Thesis for the Degree of Licentiate of Engineering

Correlating Nanostructure and Electronic Properties of Organic Semiconductors by Electron Microscopy

Gustav Persson

CHALMERS

Department of Physics

Chalmers University of Technology

Gothenburg, Sweden 2022

Correlating nanostructure and electronic properties of organic semiconductors by electron microscopy

Gustav Persson

Department of Physics
Chalmers University of Technology
SE-412 96 Gothenburg
Sweden
Telephone +46 (0)31 772 3334

Cover image:

Upper left: HAADF-STEM image of the nanostructure of a p[p($g_4$2T-T)-co-U] copolymer thin-film.
Lower left: EDX spectral image of the interface in a bilayer p($g_4$2T-T):BBL film, showing the separation between the bilayer components.
Center: HAADF-STEM image of a thin-film of p($g_4$2T-T) doped with Mo(tfd-$COCF_3$)$_3$ and a tomographic 3D reconstruction of the same sample.
Upper right: BF-TEM image of the BHJ morphology of a TQ1:$PC_{71}BM$ sample, which is used as data for simulations of charge-carrier dynamics.
Lower right: 3D tomographic reconstruction of Mo(tfd-$COCF_3$)$_3$ dopant clusters in p($g_4$2T-T) and markers indicating the positions of individual dopant molecules within the clusters.

Printed at Chalmers Reproservice
Gothenburg, Sweden 2022

Correlating nanostructure and electronic properties of organic semiconductors by electron microscopy

Gustav Persson
Department of Physics
Chalmers University of Technology

Abstract

Organic semiconductors enable fabrication and efficient processing of electronic devices with light weight, mechanical flexibility and tuneable properties. Despite significant progress in the last decades, efficiencies and long-term stabilities of these systems still need to be improved. The properties of organic semiconductors have been shown to be correlated to their morphology. In this thesis work, the nanostructures of organic semiconductors are studied using electron microscopy. Aggregation characteristics, morphology of the phases and the detailed structure of the interfaces have been studied using transmission electron microscopy with both imaging and spectroscopy. It is shown how these structural properties determine the electronic properties. Electron tomography is used to visualise the three-dimensional distribution of dopant molecules in an organic semiconductor at sub-nanometre resolution, which enables the determination of positions of individual molecules. Both individual dopants and clusters are observed. The clusters grow in size and change shape as the dopant concentration increases. This change affects the conductivity which initially increases with increasing concentration and thereafter decreases. The three-dimensional information about the dopant positions in the clusters show that the cluster morphology allow that each dopant molecule is in direct contact with the surrounding polymer. The changes in morphology of the dopant clusters can explain the decrease in electrical conductivity at the higher dopant levels. The work in this thesis provides detailed nanostructure information that is important for the understanding of fundamental mechanisms in organic semiconductors.

Keywords: organic semiconductor; nanostructure; molecular dopant; concentration; clustering; structure-property correlation; transmission electron microscopy; visualisation; 3D

Acknowledgements

The research presented in this thesis was carried out in Eva Olsson Group, Division of Nano- and Biophysics in the Department of Physics, Chalmers University of Technology, Gothenburg, Sweden, during the period of December 2018 to March 2022. The work was performed under the supervision of Prof. Eva Olsson and co-supervisor Prof. Christian Müller.

The thesis work was funded by Swedish Research Council grant 2016-06146, and this support is gratefully acknowledged.

The time spent with this project has been life-changing, and I would like to offer my sincerest gratitude to the following persons who have joined me along the way: My main supervisor Eva for all your guidance and support during the ups and downs of this thesis work, for showing me the world of electron microscopy and for creating an incredibly inspiring working environment. My co-supervisor Christian for introducing me to many concepts in the field of organic electronics and the fruitful discussions during the Organic Electronics Journal Club meetings. All the members of Eva Olsson Group; you are a fantastic group that I can always rely on for difficult scientific questions and for simple cheerful conversations. Special thanks go to Jonatan for being an excellent officemate and a great company. I would also like to thank Emmy, Sepideh, Renée and Mariza from Müller group and Magnus from RISE; none of this would have been possible without your collaborations and insightful suggestions. Many thanks to Stefan and Ludvig from Chalmers Material Analysis Laboratory for the training and the perpetual support with the microscopes, and to Ola for all the technical support. A big thank you to all the love and support I have received from family, from my partner Elin, and from my dog Bob. And finally I would like to express my gratitude to you, for taking your time and reading this thesis.

List of appended papers

This thesis is based on the following papers:

Paper I
Toughening of a Soft Polar Polythiophene through Copolymerization with Hard Urethane Segments
Sepideh Zokaei, Renee Kroon, Johannes Gladisch, Bryan D. Paulsen, Wonil Sohn, Anna I. Hofmann, Gustav Persson, Arne Stamm, Per-Olof Syrén, Eva Olsson, Jonathan Rivnay, Eleni Stavrinidou, Anja Lund and Christian Müller
Adv. Sci., 2021, 8, 2002778

Paper II
Ground-state electron transfer in all-polymer donor–acceptor heterojunctions
Kai Xu, Hengda Sun, Tero-Petri Ruoko, Gang Wang, Renee Kroon, Nagesh B. Kolhe, Yuttapoom Puttisong, Xianjie Liu, Daniele Fazzi, Koki Shibata, Chi-Yuan Yang, Ning Sun, Gustav Persson, Andrew B. Yankovich, Eva Olsson, Hiroyuki Yoshida, Weimin M. Chen, Mats Fahlman, Martijn Kemerink, Samson A. Jenekhe, Christian Müller, Magnus Berggren and Simone Fabiano
Nat. Mater., 2020, 19, 738–744

Paper III
Experimentally Calibrated Kinetic Monte Carlo Model Reproduces Organic Solar Cell Current–Voltage Curve
Sebastian Wilken, Tanvi Upreti, Armantas Melianas, Staffan Dahlström, Gustav Persson, Eva Olsson, Ronald Österbacka and Martijn Kemerink
Sol. RRL , 2020, 2000029

Paper IV
Visualisation of individual dopant molecules in organic electronics: sub-nanometre 3D distribution and correlation to electronic properties
Gustav Persson, Emmy Järsvall, Magnus Röding, Yadong Zhang, Stephen Barlow, Seth Marder, Christian Müller and Eva Olsson
In manuscript

My contributions to the appended papers

Paper I: I prepared samples for TEM analysis together with my co-authors. I performed the TEM experiments, interpreted the results together with my co-authors and wrote parts of the manuscript together with my co-authors.

Paper II: I prepared FIB-SEM cross-sections of the sample for TEM analysis. I performed the TEM imaging and spectroscopy experiments together with my co-authors, interpreted the results together with my co-authors and wrote parts of the manuscript together with my co-authors.

Paper III: I performed the TEM experiments, interpreted the results together with my co-authors and wrote parts of the manuscript together with my co-authors.

Paper IV: I planned the study and I prepared TEM samples together with my co-authors. All TEM experiments, tomography reconstructions and dopant analysis using markers were performed by me. I was involved in the data analysis using MATLAB script together with my co-authors. I interpreted all results together with my co-authors. I wrote the first draft and wrote the manuscript together with my co-authors.

Contents

List of Figures

List of Abbreviations

2D	two-dimensional
3D	three-dimensional
ADF	annular dark-field
BBL	poly(benzimidazobenzophenanthroline)
BF	bright-field
BHJ	bulk heterojunction
BSE	backscattered electron
DF	dark-field
DOS	density of states
EDX	Energy Dispersive X-ray Spectroscopy
EELS	electron energy-loss spectroscopy
F_4TCNQ	2,3,5,6-tetrafluoro-7,7,8,8-tetracyanoquinodimethane
FIB-SEM	focused ion-beam scanning electron microscope
GIS	gas injection system
GIWAXS	grazing-incidence wide angle x-ray scattering
HAADF	high-angle annular dark-field
HOMO	highest occupied molecular orbital
KMC	Kinetic Monte Carlo
LUMO	lowest unoccupied molecular orbital
$Mo(tfd)_3$	molybdenum tris(1,2-bis(trifluoromethyl)ethane-1,2-dithiolene)
$Mo(tfd\text{-}CO_2Me)_3$	$Mo(tfd)_3$ with -CO_2Me side groups
$Mo(tfd\text{-}COCF_3)_3$	$Mo(tfd)_3$ with -$COCF_3$ side groups
NMR	nuclear magnetic resonance
OFET	organic field-emission device
OLED	organic light-emitting diode
OPV	organic photovoltaic
OSC	organic semiconductors
OTE	organic thermoelectric
p($g_4$2T-T)	thiophene based polymer with tetraethylene glycol side chains
P(NDI2OD-T2)	poly{[N,N'-bis(2-octyldodecyl)-naphthalene-1,4,5,8-bis(dicarboximide)-2,6-diyl]-alt-5,5'-(2,2'-bithiophene)}
P3HT	poly(3-hexylthiophene-2,5-diyl)
p[p($g_4$2T-T)-co-U]	copolymer with p($g_4$2T-T) and urethane units
PA	polyacetylene
PBTTT-C_{14}	poly[2,5-bis(3-tetradecylthiophen-2-yl)thieno[3,2-b]thiophene]
$PC_{71}BM$	(6,6)-phenyl-C71-butyric acid methyl ester
PCE	power conversion efficiency
SE	secondary electron
SEM	Scanning Electron Microscopy

SI	spectral imaging
SIRT	simultaneous iterative reconstruction technique
STEM	Scanning Transmission Electron Microscopy
TEG	thermoelectric generator
TEM	Transmission Electron Microscopy
TQ1	poly[2,3-bis-(3-octyloxyphenyl)quinoxaline-5,8-diyl-alt-thiophene-2,5-diyl]
UV-Vis-NIR	ultraviolet-visible-near infrared
WBP	weighted back-projection

1 Introduction

1.1 Background

Since the development of the transistor, electronic devices have become an integral part of modern society. Electronics has now evolved into a key industry, with significant research and development being devoted to improving transistors in computers, light-emitting diodes for lighting, solar cells for energy production and many other devices. [1] The majority of modern electronic devices are based on silicon, a semiconducting element that is abundant in the earth's crust but also gives rise to pollution and requires energy intensive extraction and refinement in order to be used for high-quality electronics. [2] An interesting alternative to silicon is electronic devices based on organic semiconductors. Electronic devices made of organic semiconductors are associated with light weight, mechanical flexibility, high tuneability and biocompatibility. The device fabrication is also theoretically less energy intensive compared to its inorganic counterparts, making it interesting for more environmentally friendly technology and for sustainable energy production from devices such as organic solar cells and organic thermoelectrics. However, current organic electronics are generally outperformed by their inorganic counterparts regarding efficiency and long-term stability. [3–5] Despite significant progress in the last decades, there are still uncertainties regarding fundamental mechanisms in the materials, both in static conditions and during operation. Understanding and controlling such mechanisms can help improve the performance of organic electronics. [6, 7]

In recent years, multiple studies have explored how the material micro- and nanostructure are connected to relevant device properties such as conductivity or long-term stability. [7–11] Examples of such analyses are phase separation in polymer blends and dopant distribution in doped organic semiconductors. [12–15] Electron microscopy is an excellent technique for the study of material nanostructure, with the potential to resolve details even at the atomic length scales. [16, 17] At this high spatial resolution, electron microscopy also enables analytical techniques to map out chemical distributions and variations in electronic structure. [18] But analysis with electron microscopy brings challenges of its own. Organic semicon-

ductors are generally sensitive to damage or alter from the electron beam in the microscope, and care needs to be taken to not destroy the sample before relevant information can be collected. [19] This beam sensitivity has historically limited the studies of the material, but modern advancements in instruments and strategies have reduced this problem and increased the applicability of electron microscopy as a technique for high spatial analysis of organic semiconductors. [12] The versatility of advanced electron microscopy techniques are now well-suited for study of structure-property relationships in organic electronics.

1.2 Scope of the thesis

The focus of this thesis is to contribute to a better understanding of the nanostructure in organic semiconductors. Aggregation characteristics, cluster morphology, phase distribution and the detailed structure of the interfaces in organic semiconductor systems are of importance. The information regarding the material nanostructure will be correlated to electrical properties relevant for device applications.

This thesis is structured in the following way: Chapter 2 will provide relevant background information regarding organic semiconductors and organic electronic devices. Chapter 3 will describe the investigated materials, the experimental methods used for the analysis and how samples were prepared for analysis. Chapter 4 will describe the results from the studies and discuss their implications. Chapter 5 will finally summarise the conclusions from the study and provide an outlook for future work.

2 Organic Semiconductors (OSCs)

The term 'organic electronics' describes electronics made from carbon-based semiconducting materials, so called organic semiconductors (OSCs). [20] These materials offer great potential, but also big challenges to implement in practice. This thesis is focused on the analysis of OSCs and its implications when used as active material in organic electronics. Therefore, this chapter will explain in more detail the fundamentals of OSCs and how the device performance can be enhanced through processing such as electrical doping and fine-tuning of its nanostructure. Finally, the working principles and applications of OSCs in organic photovoltaics and organic thermoelectrics will be discussed.

2.1 Electronic Properties of OSCs

OSCs are a class of carbon-based compounds with semiconducting, electrochemical and optical properties that are of interest for use in a broad range of electronic applications. They are an interesting alternative to inorganic semiconductors due to relatively low-cost material with the possibility of efficient roll-to-roll processing. They can be applied in light-weight and flexible devices, and the tuneability of these polymers allows optimisation of electronic and physical properties. [21] OSCs have been known of since 1834, but only experienced isolated studies until the 1970's. [21] The work of MacDiarmid, Heeger and Shirakawa on polyacetylene, which resulted in the Nobel price in chemistry year 2000, [22] inspired further studies in the field and multiple critical discoveries in the following years. Initial efforts mainly focused on OSC conductivity, but as the materials progressed into functioning devices there was also a shift towards a better fundamental understanding of structure-property relationships and interest in new application-relevant metrics such as long-term stability. [21] The research in improving structure and electronic properties have lead to relatively complex OSC molecular structures that are optimised for use in organic electronic devices. [23] Examples of increasingly complex molecular structures of relevant OSCs are shown in figure 2.1.

OSCs behave like semiconductors, meaning that similarly to their inorganic counterparts there is a notable separation in energy between the highest occupied

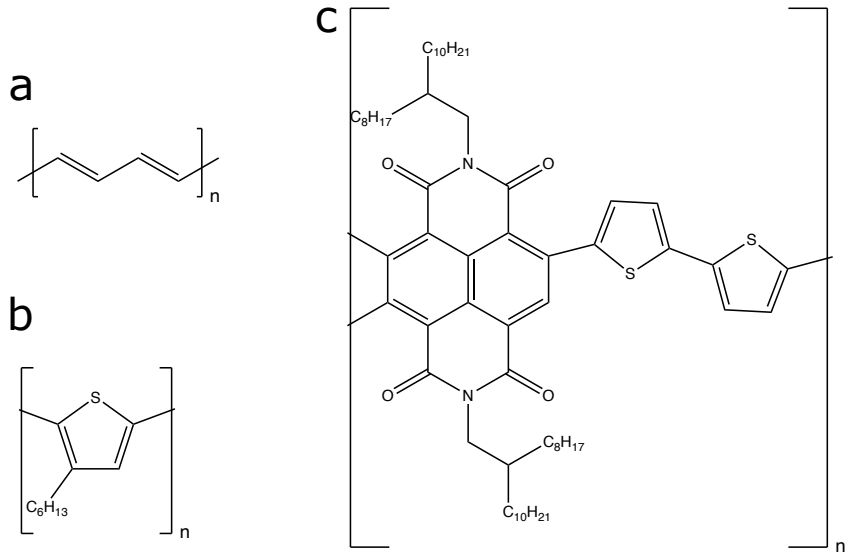

Figure 2.1: Molecular structures of example OSCs from early- to later years, illustrating increasingly complex structures. (a) Polyacetylene (PA), (b) Poly(3-hexylthiophene-2,5-diyl) (P3HT) and (c) Poly{[N,N'-bis(2-octyldodecyl)-naphthalene-1,4,5,8-bis(dicarboximide)-2,6-diyl]-alt-5,5'-(2,2'-bithiophene)} (P(NDI2OD-T2))

molecular orbital (HOMO) and the lowest unoccupied molecular orbital (LUMO) for their electrons. The difference in energy between HOMO and LUMO is termed the band gap. By tuning the band gap to an appropriate level the material may either act as an insulator, or as a conductor if sufficient energy is applied externally for the electrons to overcome the energy gap. It is the possibility of manipulating semiconductors to control the electron motion that have made semiconducting materials a fundamental part of electronic devices. The semiconducting properties in organic materials come from sp^2-hybridisation of bonds between carbon atoms, meaning that carbon forms spatially confined bonds (σ-bonds) and delocalised bonds (π-bonds) with neighbouring atoms. The π-bond is not as energetically deep as the σ-bond, and is responsible for the optoelectronic properties of the material. When an electron overcomes the energy gap and is promoted to one of the unoccupied energy levels, it also frees the state in the energy level it left behind, creating a positively charged quasi-particle called a hole. [20] Materials can be designed to preferentially transport either electrons or holes, where electron transporters are often referred to as n-type materials and hole transporters as p-type materials. These names does not rely on the ability to transport charges but rather how easily charges can be injected from electrodes that are used in devices, which in turn is associated with energy levels of the material. If the electron affinity of

the material is closely matched to the electrode Fermi level, it is an n-type. If the ionisation energy is closely to the Fermi level, it is a p-type. Efficient charge transport requires that charges move through the material without becoming trapped or scattered. [24]

Most inorganic semiconductors are bound together with strong covalent bonds, enabling them to be grown as highly ordered crystals. In contrast, intermolecular bonds for OSC are often of weak nature such as van der Waals forces, resulting in a soft and less ordered solid. A consequence of this disorder is generally slower charge carrier movement. [20] Many factors can affect charge mobility in organic semiconductors, including disorder, size and weight of molecules, molecular packing, presence of impurities, charge-carrier density, electric field, temperature and pressure. As a result, modelling charge transport for organic semiconductors is more complex than for conventional inorganic semiconductors. One-electron approaches is usually sufficient to well describe inorganics, while organics often require the consideration of both electron-electron and electron-phonon interaction. [24]

2.2 Molecular Doping

A pure semiconductor is known as an intrinsic semiconductor, and these are seldom used in real applications. Instead, by introducing a small amount of impurities into the material the Fermi level can be shifted and electron or hole conductivity can be increased manyfold. This process is known as doping, and is well-established in the field of inorganic semiconductors in order to enhance device efficiency. [7] Typically, a low concentration of atoms (ratios of $10^{-6} - 10^{-3}$) covalently bond with the host atoms to either add electrons in donor states (n-type doping) or holes in acceptor states (p-type doping). In the example of crystalline silicon, small amounts of boron atoms can be introduced for p-doping or phosphorous atoms for n-doping, generating mobile charges without disrupting the crystalline structure. [25] The efficiency of this process tends to be high for inorganic semiconductors, typically generating one free charge carrier per dopant atom, which as a result leads to a dramatic increase in conductivity even at these low concentrations. [26] Since doping allows for a high control over electrical parameters in inorganic semiconductors, organic semiconductors needs a similar process in order for their devices to be competitive.

Interestingly, the first organic electronic applications almost exclusively used intrinsic semiconductors, not utilising the potential benefits of doping. This was because the first attempts of doping organic semiconductors used halides as dopant atoms, which does not covalently bond with the organic molecules and therefore have a tendency to diffuse around in the material. Doped layers therefore became unstable under operating conditions. A solution to this problem is to use larger organic molecules as p- or n-dopants. [26] Controlling the molecule's size or shape has allowed a better control of diffusion and enhanced stability of doped layers. [7] Molecular doping has been a huge success for practical applications, allowing modern devices to push conductivities several orders of magnitudes higher. Despite this success, introducing these organic molecules have also added new complexity to organic semiconducting systems, and fundamental mechanisms are still under debate. The doping efficiency in molecularly doped organic semiconductors are much lower than in inorganic systems. This necessitates a larger amount of dopants for practical applications, commonly reaching concentrations of multiple percent. These large concentrations have in turn shown to have a significant impact on the material structure, turning crystalline areas to amorphous and increasing the density of traps and scattering centres for charge carriers upon doping. Structural changes upon doping are usually not desired, and significant effort have been put into achieving higher doping efficiencies at lower doping concentrations. Depending on choice of molecular dopant or semiconducting host, free charges can be generated through a number of different chemical mechanisms, but neutral dopants are understood to have two general types of interaction mechanisms: ion-pair formation (full charge transfer) or charge complex formation (partial charge transfer). [26]

In the case of ion-pair formation the dopant is completely ionised, *i.e.* a p-dopant will extract an electron from the host OSC and a n-dopant will donate an electron to the host, leading to a localised charge on the dopant and a mobile opposite charge in the OSC matrix. Experimental observations from a number of systems have pointed towards the validity of this ion-pair formation model, but there have also been exceptions. [27] This has been explained through the model of charge transfer complexes, or partial charge transfer. A charge transfer complex may form as an hybridisation of overlapping molecular orbitals for dopant molecule and host OSC. This will form new, local HOMO and LUMO levels notably different from HOMO and LUMO of the OSC and the dopant, where the new degree of hybridisation and energetic splitting is dependent on the initial energetic and spatial overlap. The charge will be shared between dopant and OSC in the charge complex, so this case leads to a partial charge transfer as opposed to a full charge transfer in the case of ion-pair formation. A consequence of this is that charge

transfer states must be thermally ionised, leading to a generally lower doping efficiency than for ion-pair formations. [28]

The ionisation efficiency of dopant molecules have also been shown to be affected by disorder in the OSC system. As dopants are added and contribute with charges to the OSC, the resulting dopant ions remain in the system and generate local electrostatic fields that can be felt by other molecules. This will introduce an electrostatic disorder. With a random distribution of dopant molecules, the resulting fields will randomly shift energy levels of local molecules and give rise to an energetic disorder. The energetic disorder can be determined by measuring how the system density of states broadens as a result from the disorder. As will be discussed in the following section (2.3), doping may also introduce significant structural disorder to the OSC, which can also affect the energetic disorder in the material. Recent studies have used simulations to show that dopant ionisation efficiency and device-relevant parameters can be affected as a result of the increased disorder after doping. [29, 30]

It is common for organic molecules to have an equilibrium geometry that is different in ionised state compared to in ground state. Specifically, in an organic polymer chain, it can be energetically favourable to spatially localise the charge on the chain and have a local distortion around the charge. If the relaxation energy gained from this distortion is greater than the energy required to have a distorted lattice, the charge becomes spatially bound with a binding energy equal to the energy difference. This formation is called a polaron, and is a charge-matter coupling where a charge becomes spatially bound to the place of distortion in the host. As new dopants are added, it can also be energetically favourable to add a second charge to the polaron rather than somewhere else along the polymer chain, forming one bipolaron instead of two lone polarons. The formation of bipolarons can only happen if the lattice interaction is greater than the Coulomb repulsion between the two charges confined to the same location. Adding polarons or bipolarons causes new localised electronic states in the OSC band gap due to local upward shifts of HOMO and downward shifts of LUMO, making new electronic transitions available. [31] Although a polaron may diffuse through the lattice, the formation of polarons and bipolarons still means that charges are spatially confined, not acting as free charges, which have a negative impact on overall conductivity. The exact delocalisation of charges in polarons depends on choice of system, but as an example recent modelling suggests that polarons are delocalised over 10-20 molecules or monomers for some high-performance OSC, *i.e.* over a few nanometers. [32] This means that nanoscale distribution of polarons influences the performance of organic semiconductors.

2.3 Nanostructure of OSCs

It was understood at an early stage that transport properties in OSC materials are highly dependent on its nanostructure. Their heterogeneous structure can be described as neither ordered nor completely disordered, and order can exist at lengthscales ranging from atomic to microscopic and mesoscopic levels. One particular challenge of this heterogeneity is understanding how the spatial arrangement of these differently ordered regions affects charge transport internally and across multiple regions. Due to this, characterisation techniques that analyse structure over multiple lengthscales or a combination of different techniques are important for a greater understanding of structure-property relations within OSC. [33]

As an example, understanding of how polymer chain alignment and degree of crystallinity is connected to their mechanical properties have allowed the development of fibers with higher specific strengths than steel. It was initially thought that a more crystalline microstructure would lead to a better transport than in disordered systems. This may often be the case for inorganic semiconductors, but this idea is challenged by observations of disordered or even amorphous polymers performing on par with semicrystalline polymers. It has been suggested that since charges have a short scattering mean free path in stacked molecules with a strong π-orbital overlap, they are mostly affected by short-range order in the material. Hence, charge transport would mostly be affected by short-range ordering and their interconnection in the material, and crystallites of multiple scattering lengths would bring very little additional benefit for the transport. Such short-range order is typically in the lengthscale of single nanometres. Based on this, it has been suggested that developing organic molecules with improved packing, orbital shape, symmetry and orientation can lead to enhanced transport properties in OSC. [34, 35] Due to its dependence on molecular packing, OSC can also display asymmetrical electrical properties along different orientations. Such anisotropy can even be manipulated, as shown by Hynynen *et al.* by tensile drawing a free-standing polymer film and effectively forcing the polymers chains to align along the stretching direction, resulting in a significant difference in conductivity parallell to drawing compared to perpendicular direction. [36]

The effectiveness of molecular doping has been closely linked to structure of both dopant and host OSC. Incorporating dopant molecules changes the OSC nanostructural ordering, and the close connection between structure and electrical properties makes it important to analyse and understand these changes. Experimental observations implies that dopant molecules are not randomly distributed in the host OSC, but rather towards preferential sites. Blends of the polymer poly[2,5-bis(3-tetradecylthiophen-2-yl)thieno[3,2-b]thiophene] (PBTTT-C_{14}) and

the molecular dopant 2,3,5,6-tetrafluoro-7,7,8,8-tetracyanoquinodimethane (F_4TCNQ) show that F_4TCNQ have a tendency to intercalate between the conjugated backbones of the polymer, forming π-stacked aggregates and crystallites. A similar phase has been observed for F_4TCNQ-doping of the polymer P3HT, where experimental data suggests that the dopant molecules incorporates into ordered polymer regions, forming crystalline dopant-polymer complexes with high density of dopants. The formation of such domains means that less ordered areas suffer from a deficiency of dopants and may limit the overall conductivity. [8, 37]

It has been shown that engineering of polymer side chains can help the dopant insertion mechanism in the the polymer matrix. After experimentally demonstrating that F_4TCNQ dopants mainly locate in the layers of alkyl side chains in P3AT and PBTTT-C_n, a systematic analysis of the effect of changing the length of the alkyl side chain of the polymers shows that there exists an optimum chain length for hosting dopants, and longer or shorter side chains leads to slower dopant kinetics and lower final doping levels. The studies conclude that longer side chains have a higher degree of order and becomes tightly packed, decreasing the dopants ability to diffuse efficiently into the film. Too short side chains, on the other hand, becomes too disordered which also may prevent efficient intercalation. Hence the loosely packed side chains of PBTTT-C_{12} seems to yield the highest F_4TCNQ doping level for PBTTT-C_n, and P3HT (*i.e.* C_6 side chains) is optimal for P3AT. [38, 39] Using polar side chains instead of apolar alkyl side chains is another option that has been explored for doping of conjugated polymers. Kroon *et al.* compared F_4TCNQ-doping of P3HT and p($g_4$2T-T), where the latter contains polar oligo ethylene oxide side chains. The study showed a higher maximum conductivity of doped p($g_4$2T-T) than for doped P3HT, and this was partially attributed to a better dispersion of dopants in the polar side chains, which does not form crystalline aggregates even at larger dopant fractions. The authors also noted a significantly higher thermal stability for doped p($g_4$2T-T), which was rationalised with an improved binding of the molecular dopants in the polar side chains. [40]

Studies of electronic properties as a function of dopant ratio often displays a saturation of important parameters such as conductivity past a certain point. Continuing past this optimum doping ratio does not increase the system's conductivity, and for many cases it even leads to a decrease. The reasons for this is still not fully understood, and although suggestions have been made there are still too much unknown to accurately predict the efficiency of doping in different OSC systems. [7] It has been suggested that morphology plays a crucial role in the flattening and eventual decline of conductivity at high doping concentrations. As dopant molecules becomes embedded in the host OSC, they may disrupt the system microstructure

and even form new phases, leading to a reduction in charge mobility. [41] Larger aggregates of dopants have also been observed in doped systems, resulting in morphological changes that can be correlated with a saturation in conductivity. These aggregates can grow larger at higher doping ratios, up to a few hundred nanometers in size, and seems to be connected to less efficient doping of the OSC. [42] Dopant aggregates have also been reported to stop growing at certain sizes (*e.g.* around 20 nm), but the aggregates instead become more frequent in the film at higher doping concentrations. Interestingly, nuclear magnetic resonance (NMR) analysis on the same samples have shown a lack of unreacted dopants in these samples, indicating that the aggregates may contain a finer nanostructure that allows the dopants to remain in contact with the OSC. [43] The three-dimensional structure of aggregates can also be of high importance for the transport properties in the OSC. Donhauser *et al.* have shown that dopants may not only aggregate, but they can also form filamentous structures of high doping concentration that connects one side of the thin film with the other. The formation of such filaments is expected to lead to highly anisotropic conductivity, with preferential charge transport at the film surface or within the vertically aligned nanostructures. [44] Such findings are indications of that nanostructure can be closely connected to electronic properties, and a better control over final morphology is highly relevant for the fabrication of efficient OSC.

Different doping schemes have been developed in attempts to better control the dopant-host OSC interaction. A common doping method is the 'mixed-solution method', where the OSC is dissolved in a solved and the dopant is added into the solution. The mixture of OSC and dopant is then used to directly form the film. An alternative to this is the 'sequential doping method', where the undoped OSC is allowed to first form a film and then the dopant is dissolved in an orthogonal solvent and added on the already dried OSC film. Although the mixed-solution method allows better control of the final ratio between OSC and dopant and a higher maximum achievable doping concentration, sequential doping has the advantage that the OSC microstructure is formed in advance, and may be less affected by the dopant molecules. A comparison between mixed-solution and sequential doping of F_4TCNQ on P3HT have shown that surface roughness of mixed-solution films are significantly higher than for the same doping concentrations achieved through sequential doping. The authors conclude that the higher surface roughness comes from aggregation that happens in the mixed solution before the film microstructure has formed. In the same study it is also noted that the conductivity for sequentially doped films are higher than films doped through mixed solution at the same doping concentration. [45] Another way to perform sequential doping is through vapour deposition, where an undoped OSC is first formed and then exposed to dopant molecules in vapour phase which sublimes

in the film. Doping through vapour deposition has also proven to be effective at preserving the OSC nanostructure. [46]

After charge transfer between dopant and host OSC, the dopant molecule will remain in the system as a charged counter-ion. The dopant counter-ions tend to not covalently bond but rather bond to its location with weak forces such as van der Waals or Coulombic interaction. The weak binding forces means that the dopants' spatial locations can change through diffusion or drift. It has been shown that the diffusion process requires an activation energy close to the thermal energy of room temperature, meaning that extensive rearranging of dopants' spatial distribution can happen over time, which in turn may severely affect the long-term stability of organic electronic devices. Dopant diffusion in organic electronics was a major reason why atomic dopants were abandoned in favour of small molecules which are less mobile. Although this change seems to have improved long-term stability, diffusion is still a significant problem for modern applications. Studies on dopant diffusion have concluded that the rate of diffusion is dependent of dopant molecule size and shape and also the nanostructure of the host OSC. The F_4TCNQ molecule is relatively small and has a planar structure. Bulky, three-dimensional dopant molecules are expected to have lower diffusion rates, and may be promising for a higher long-term stability on the systems. [47] An example of a well studied bulky molecular dopant is molybdenum tris(1,2-bis(trifluoromethyl)ethane-1,2-dithiolene) ($Mo(tfd)_3$), an organometallic molecular dopant where three tfd side rings are arranged in a trigonal prismatic geometry around one Mo atom. It is a p-dopant with a high electron affinity, promising stability and in recent years it has been made more solution processable by addition of ester side groups. [48, 49] However, the three-dimensional structure also means that the molecule displaces more volume in the OSC, which could lead to a higher degree of morphological disruption and lower maximum doping levels. [50]

Due to the larger size of $Mo(tfd)_3$-derivatives, the dopants are expected to not be able to enter the π stacked crystallites of P3HT at room temperature. However, a study has reported a higher diffusion of $Mo(tfd\text{-}CO_2Me)_3$ in regioregular P3HT than regiorandom P3HT, despite that the more ordered regioregular P3HT should contain a higher fraction of these crystalline regions. The article suggests that that the higher diffusion could be explained by a higher free volume in grain boundaries or connecting regions between crystallites in regioregular P3HT. [51] This example shows how the nanostructure of these systems is often complex and interpretation may not be straightforward.

After successful doping, a doping gradient results in a Fermi level gradient within

the OSC, which in turn will result in a static electric field within the material. Despite that such an electric field might affect dopant diffusion properties or impose drift across layer interfaces, there are only a few studies regarding this matter. [7] One study that analysed the drift of $Mo(tfd\text{-}CO_2Me)_3$ in P3HT and a small molecules OSC noted that significant drift could be induced after applying an electrical field across the doped material. After placing a thin film between two electrodes and applying a moderate electrical field relevant for device application, the authors demonstrated a drift of several micrometers. Such drift may lead to a significant inhomogeneity of electrical properties in the material due to depletion of dopants in some regions and accumulation of dopants in others. Interestingly, the same study showed that the drift could be reversible by changing the direction of the applied field. Doping drift over several micrometers is detrimental for the efficiency of organic field-effect transistors, solar cells and organic light-emitting diodes, and although the effect may be less severe for some material systems it could still be of interest for understanding long-term device degradation. [52]

Molecular doping is crucial for the fabrication of high-performance OSC, but nanostructure related problems such as aggregations have proven to limit their performance. A recent strategy to reduce the impact on the nanostructure is through double doping, *i.e.* dopants where the molecules may transfer two charges each. This could result in that lower doping concentrations are needed for the devices. [53] Another strategy that is explored in this thesis is to avoid these problems through ground-state charge transfer. By engineering energy levels of the components in OSC blends, charge transfer may spontaneously occur at their interfaces which results in highly conductive pathways without any doping. This will be described in more detail in section 4.1.2.

2.4 Organic Electronic Devices

After the early stages of work in the field of organic semiconductors in the 1980's, OSC application in devices began to emerge. Electrical conductivity was the common metric during initial years, but as development in the 1990's progressed into device application there was a pursuit towards new OSC architectures to optimise different applications. Consequently, a better fundamental understanding of structure-property relationships was emerging. New metrics such as thermal- and light stability began to be of interest for specific applications. Devices that received significant attention were organic photovoltaics (OPVs), organic light-emitting diodes (OLEDs) and organic field-emission devices (OFETs). [21] This thesis focuses on systems relevant for applications in OPVs and another emerging

technique called organic thermoelectrics (OTEs), and these devices will therefore be explained in more detail.

2.4.1 Organic Photovoltaics (OPVs)

Solar energy has been suggested as one of the major forms of future sustainable energy since sunlight equivalent to approximately 6000 times the global energy consumption hits the earth's surface each year. This large theoretical potential has been a main argument for solar energy for a long time. The first solar cell based on silicon was invented 1953 [54], and already five years later the first solar module was used in space. Silicon has been established as the most common semiconducting material in industry for solar cells and multiple other electronic application areas. [54] But other types of materials have been investigated as candidates to replace silicon.

Organic photovoltaics can be seen as one of the more recent, emerging technology. [55] In fact, on the global scale of energy production where the criterion of abundant raw materials becomes more relevant, only silicon- and carbon based photovoltaics are favoured. [56] Using OSCs as the active material in photovoltaics offers several advantages. High absorption coefficients means that only little material is needed and the material can be made into thin films. Thin films can be made on flexible substrates, resulting in light-weight, flexible photovoltaic panels. OPVs are also associated with simple fabrication methods that can be scaled up to industrial levels, and chemical synthesis allows high level of tuning of mechanical, electrical and optical properties. [57] Inorganic solar cells are also related to higher energy costs and environmental issues that have partially slowed down their spread. Despite these positive aspects, power conversion efficiency (PCE) and long-term stability of OPVs have historically been lower than their inorganic counterparts, and have slowed down their commercial spread. Both of these properties can be connected to the device nanostructure. [58, 59]

Converting sunlight into useable electrical energy involves several steps for OPVs, and each of these steps have to be optimised in order to avoid bottlenecks for the overall efficiency of the device. When a photon is absorbed by the active OSC layer, an electron is excited to the LUMO level and a hole is generated in the HOMO level. However, the excited electron and the resulting hole have a binding energy that keeps them together as an electron-hole pair, commonly referred to as an exciton, and this binding energy is significantly higher for OPV compared to their inorganic counterparts. In order to overcome the exciton binding energy, OPV devices consisting of donor and acceptor OSCs have been developed, where

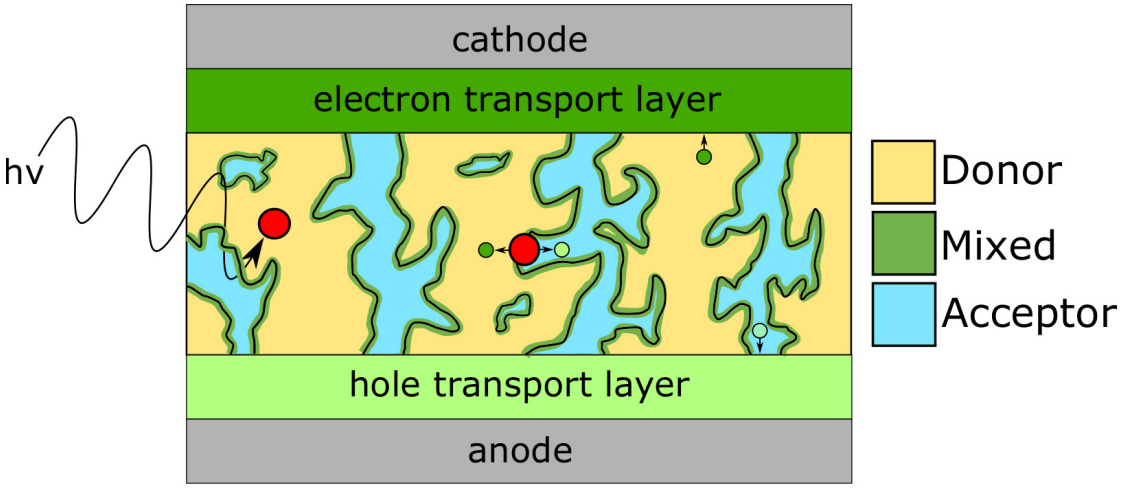

Figure 2.2: A typical architecture of an organic photovoltaic cell. The active layer consists of a bulk heterojunction between donor and acceptor materials. The figure illustrates three elementary steps when converting sunlight into electrical energy: exciton generation through absorption of sunlight, exciton separation into free charge carriers and charge carrier transport to the electrodes.

the HOMO and LUMO energies are lower in the acceptor than those of the donor. From this follows that at the donor-acceptor interface, it is energetically favourable for electrons to transfer to the acceptor material and holes to the donor material, effectively splitting the excitons into free charge carriers. However, an exciton only has a finite lifetime before it deexcites. In practice, excitons diffuse a distance of typically 20 nm or less in OSCs before the electron-hole pair recombines and the photon energy is lost as lattice vibrations. In order to maximise charge separation, excitons should therefore always be generated less than 20 nm from a donor-acceptor interface. [57]

An answer to this tough requirement is the bulk heterojunction (BHJ) structure, which has significantly improved the PCE of OPVs. In a BHJ, the donor and acceptor materials are mixed together to form a bicontinuous network with maximised interfacial area. An example of such a structure is shown in figure 2.2. After exciton splitting, a BHJ needs to provide continuous pathways for the charges to be transported to the electrodes where they can be extracted. If a free charge encounters an opposite charge during the transport to its electrode, or if it encounters an interface with the opposite component of the blend, it will recombine and not contribute to the overall OPV charge generation. [58] Fine-control of nanoscale distribution of the BHJ has proven difficult, and multiple studies have been published

regarding the analysis and optimisation of commonly used OPV blends. [10,11,60] Even after achieving an optimal BHJ, the structure is often not thermodynamically stable and may degrade over time. Elevated temperatures have shown to speed up this process, and degradation of the fine-scale phase distribution of BHJ can be correlated to a decrease in device PCE. Exposure to air and even to some extent sunlight may also lead to degradation, reducing the OPV performance over time. Molecular engineering of OSC that are resistant to these types of degradation is therefore seen as general methods to increase stability. [59, 61]

The complete process of light harvesting in OPV has been the target of intensive research, which has led to an improved understanding and eventually the development of new record-breaking OSC blends. OPV lifetime can now reach timescale of years [62], and the PCE of OPVs has reached 18.3 %. [63] However, high values of stability and efficiency are seldom realised simultaneously. Computer simulations have been suggested as a tool to better direct the molecular design of new OSC materials for OPVs, to predict properties and to hasten a more widespread commercialisation. Key properties such as electrical properties have proven difficult to model so far, but more recent models that include nanoscale structure have shown significant improvements in these aspects. [64] In this thesis, the experimental data describing a BHJ nanostructure are used to improve the accuracy of electrical characteristics simulations, and will be further discussed in section 4.1.3.

2.4.2 Organic Thermoelectrics (OTEs)

Studies show that a large part of the energy produced globally is lost as waste heat. Efforts for a more sustainable energy consumption has drawn the attention towards thermoelectric generators (TEGs) that can directly convert heat gradients back to electrical energy. A thermoelectric generator is a device that utilise thermoelectric materials that exhibit a strong Seebeck effect.

When a temperature gradient is applied over the material its dominant charge carriers will diffuse towards one side, effectively providing an electric current. The strength of this thermoelectric effect can be described by a material parameter called the Seebeck coefficient, α. Doping can be used to control the dominant type of charge carriers in the material, *i.e.* holes or electrons. Electrons will diffuse towards the hot side in n-doped materials, while the holes will diffuse in p-doped materials. This control of charge carrier flow is used by a TEG, where two legs of different doping types are connected and put in a temperature gradient, giving rise to an electrical current. Thermoelectric materials may also be used

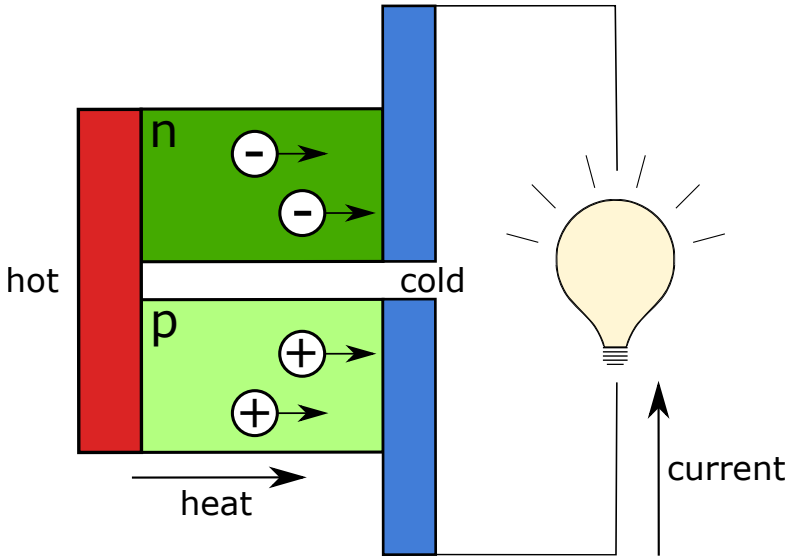

Figure 2.3: A simple schematic of a thermoelectric generator consisting of two legs of oppositely doped thermoelectric materials. A heat gradient of the materials results in charge carrier transport from the hot to the cold side. Connecting the p-type material with the n-type material gives rise to an electrical current.

'reversely' by applying an electrical current to cool or heat an area. This ability to create a heat gradient from a difference in potential is called the Peltier effect. A schematic of the working principle of a TEG is shown in figure 2.3.

The power generation efficiency of a TEG can be evaluated through a dimensionless thermoelectric figure of merit described by

$$ZT = \frac{\alpha^2 \sigma}{\kappa} T \tag{2.1}$$

where α is the Seebeck coefficient, σ is electrical conductivity, κ is thermal conductivity and T is the absolute temperature. As can be seen in equation 2.1, a dilemma of thermoelectric materials is that the maximum figure of merit is achieved by a high electrical conductivity and a low thermal conductivity. However, these material properties are usually linked, making optimisation of thermoelectric efficiency difficult. [65, 66]

Despite this dilemma, there are multiple advantages of TEGs. Unlike most heat engines, the energy is directly converted without any intermediate conversion into mechanical energy that may involve losses. Since there are no moving parts in the

device it is exceptionally reliable and usually boasts a long lifetime. TEGs can also be scaled from micro generation up to industrial applications without additional complications. Examples of areas where TEGs can be applied are waste heat recovery in vehicle exhaust gases and industry, power generation in remote areas and microgeneration for sensors and microelectronics. [67]

However, low efficiencies and high costs have limited the spread of thermoelectric devices. In the last decades, inorganic semiconductors like Bi_2Te_3 and PbTe have been the main materials for thermoelectrics. Although they are performing relatively well, the high weights, low abundances and toxicities are drawbacks of these materials. [67] These are properties where thermoelectric devices made from organic semiconductors have the potential to excel. Organic thermoelectrics (OTEs) have started to be explored in more recent years. They have the advantages of being compatible with inexpensive and scalable fabrication methods, while being more lightweight, flexible and biocompatible compared to their inorganic counterparts. OTEs is also better at operating with smaller temperature gradients close to room temperature.

According to equation 2.1, a good thermoelectric material should have high electrical conductivity and low thermal conductivity. Inorganic thermoelectrics generally satisfy the first but not the second part, while the opposite is usually true for organic thermoelectrics. The overall efficiencies of OTE are still lower than for their inorganic counterparts, and since κ is commonly satisfactory there has been considerable research focused towards increasing the power factor $\alpha^2\sigma$. [68] Optimisation of the power factor has proven difficult, and studies have found that the Seebeck coefficient decreases as a function of conductivity according to the empirical relationship $\alpha \propto \sigma^{-1/4}$. In efforts to break this relationship, one aspect that have been studied in recent years is the properties' dependence on the material structure. [69–71] One such study noted that a higher crystalline order in a doped polymer resulted in significantly improved electrical conductivity, but only small changes in Seebeck coefficient, leading to an increased power factor with increased structural order. [46] In another study, polymer chains were aligned by tensile strain which led to an anisotropy in the conductivity but kept the Seebeck coefficient relatively constant. These results show that alignment of polymer chains is a method to increase the thermopower along the strain direction and surpass the empirical relationship between α and σ. [36] As mentioned in section 2.2, it has been recently noted that energetic disorder in the OSC may also affect device parameters such as the relationship between α vs σ in thermoelectrics. [30] Relations between structural disorder, energetic disorder and electronic parameters will be further discussed in section 4.2.3.

Flexible OSCs that can deform without fractures are highly relevant for OTE applications. [66, 72] This is possible for polymers that operate above their glass transition temperature T_g. Conductive polymers with polar side chains have lower T_g than similar polymers with alkyl side chains, resulting in notably soft materials. [40] However, too soft structure may also be problematic for practical application for OTEs that require free-standing structures and some mechanical stability. [70] The fabrication of an OSC with both electrical and mechanical properties suitable for OTE is described in section 4.1.2, where the soft polymer with polar side chains p($g_4$2T-T) is copolymerised with urethane segments in order to enhance mechanical stability.

Organic thermoelectrics are complex systems, and the correlation between choice of OSC, dopant molecule, doping process and the resulting thermoelectric properties are not fully understood. [73] The development of OTE devices is still at an early stage compared to their inorganic equivalents, but their positive aspects continue to attract considerable research attention. Besides a focus on outperforming inorganic materials in classical thermoelectric applications such as power generation in remote areas, new areas may also be explored with the properties of OTEs. Flexible, lightweight modules that can perform with small temperature gradients open up applications in future such as biointegrated and wearable devices, *e.g.* making use of the body heat to continuously provide power in artificial skin or in e-textiles. [68, 70] Great progress has already been made and although many challenges remain, continued research for a better understanding of the systems may lead to further success and an exciting future for OTEs.

3 Experimental

This chapter will present the materials and experimental methods chosen in this thesis for the study of structure-property relationships in OSCs. The materials studied in the thesis will first be introduced. This will be followed by a thorough explanation of the main methods for structural characterisation. Finally, sample preparation as a prerequisite for these techniques will be discussed in the final section.

3.1 Materials

As described in chapter 2, the properties of organic electronic systems may vary significantly depending on the choice of materials. This section will introduce the OSCs and the dopant molecule studied in this thesis. The OSCs include the conjugated polymers p($g_4$2T-T), poly(benzimidazobenzophenanthroline) (BBL) and poly[2,3-bis-(3-octyloxyphenyl)quinoxaline-5,8-diyl-alt-thiophene-2,5-diyl] (TQ1), and the organic small molecule (6,6)-phenyl-C71-butyric acid methyl ester ($PC_{71}BM$). The molecular dopant is Mo(tfd-$COCF_3$)$_3$. This text will briefly discuss properties and reasons for interest in these OSCs and the dopant molecule. Finally, spin coating will be discussed, which is a method to fabricate thin film specimens from these materials.

3.1.1 p($g_4$2T-T)

p($g_4$2T-T) is a conjugated polymer that consists of a thiophene backbone, simliar to well studied OSCs like P3HT, but with polar tetraethylene glycol side chains instead of aliphatic to increase its processability in polar solvents. The molecular structure of p($g_4$2T-T) is shown in figure 3.1 a. Figure 3.1 b shows the molecular structure of the copolymer p[p($g_4$2T-T)-co-U] which will be further discussed in section 4.1.1. A recent study has shown that doping with the commonly used molecular dopant F_4TCNQ leads to electrical conductivities up to 100 S/cm. The polymer's compatibility with these polar dopants also leads to a high thermal stability for the system, making it promising for use in applications such as OTEs. [40]

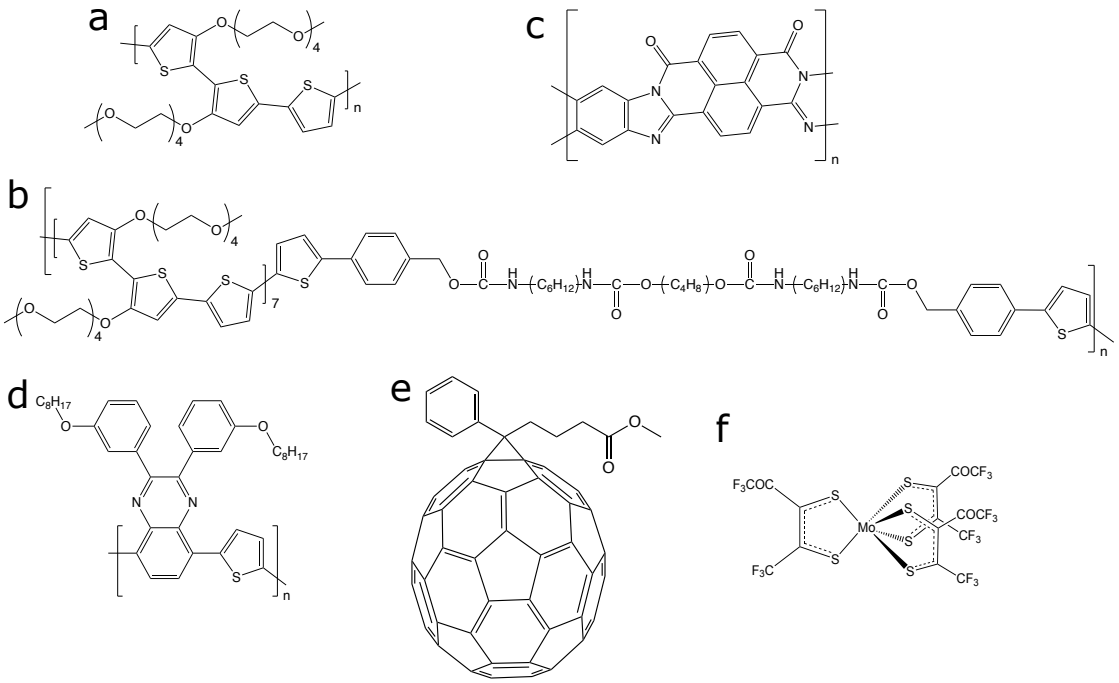

Figure 3.1: Molecular structures of the OSCs and molecular dopant used in this thesis work: (a) p($g_4$2T-T), (b) p[p($g_4$2T-T)-co-U], (c) BBL, (d) TQ1, (e) $PC_{71}BM$ and (f) Mo(tfd-$COCF_3$)$_3$.

As discussed in section 2.2, coprocessing of OSCs such as P3HT with F_4TCNQ results in formation of ion-pairs which aggregate, leading to a suboptimal nanostructure. The study shows that adding polar side chains is a promising design concept for suppressing this aggregate formation, reducing the losses in conductivity and thermal stability at room temperature coprocessing. Grazing-incidence wide angle x-ray scattering (GIWAXS) experiments in the same study show a lack of signal from F_4TCNQ crystals at higher dopant fractions, indicating that the dopant stays molecularly dispersed in the polymer even at higher concentrations. Although it has yet to be experimentally shown, the dopants are expected to be spatially located in the polymer side chains, where the polar nature of the chains should improve their binding. It has also been speculated that a decreased density of side chains, such as for p($g_4$2T-T) compared to P3HT, increases the available space for the dopant counter-ion which could lead to a higher degree of stability. [74]

3.1.2 BBL

BBL is a heteroaromatic polymer that has been well studied for its optical and electronic properties. Its molecular structure is illustrated in figure 3.1 b. The BBL monomer has a two-dimensional geometry, resulting in a more limited conformational freedom and less hinderance for electron delocalisation for the polymer. Thus, BBL displays a high mobility for charge-carriers. Doping has been used to form conductive BBL films that have shown high thermal stability [75], making it attractive for use in organic electronics such as OPV or organic field-effect transistors. [76] The high electron affinity and electron mobility makes BBL suitable for n-type transport layers in polymer-based devices. [77] Section 4.1.2 discusses a study of the interface structure of a p($g_4$2T-T):BBL bilayer.

3.1.3 TQ1:$PC_{71}BM$

BHJ blends of semiconducting polymers and fullerenes have been widely studied as donor and acceptor materials in OPVs. A fullerene derivate commonly used as acceptor material is $PC_{71}BM$. BHJ thin-films based on fullerenes tend to form high-performance active layers for OPV, which in part is due to a relatively stable nanostructure resistant to phase separation. The stable structure can be formed by heating $PC_{71}BM$ above its glass transition temperature (T_g), causing $PC_{71}BM$ to crystallise. This process is called thermal annealing. $PC_{71}BM$ have been shown to offer promising photovoltaic performance in blends together with the electron donor TQ1. TQ1 is an amorphous polymer that does not crystallise upon annealing. The difference in ordering and chemical composition between the TQ1 and $PC_{71}BM$ have been used in previous studies to distinguish the two blend components. [78, 79] The molecular structure of TQ1 and $PC_{71}BM$ are displayed in figure 3.1 c and 3.1 d. The nanoscale phase distribution of a TQ1 and $PC_{71}BM$ BHJ have been investigated in this thesis, and the results from this study are discussed in section 4.1.3.

3.1.4 Mo(tfd-$COCF_3$)$_3$

Many OSCs do not have a high electrical conductivity on its own, and require doping through a molecular dopant to increase its applicability in organic electronics. High-performing molecular dopants often contain elements of similar atomic number as the host OSC, making it difficult to distinguish the dopant from its host when characterising the dopant spatial distribution. Such is the case for the commonly used F_4TCNQ. One molecular dopant with a distinct element is molybdenum tris-[1,2-bis(trifluoromethyl) ethane-1,2-dithiolene], or Mo(tfd)$_3$. Mo(tfd)$_3$

is a p-type dopant, and besides being easier to identify during material characterisation since it contains the relatively heavy element Mo in a light-element surrounding, it also offers advantages to F_4TCNQ such as larger molecule size, higher electron affinity and a lower volatility. [48] In recent years, a more soluble derivative of $Mo(tfd)_3$ has also been synthesised by exchanging one -CF_3 side group with -$COCF_3$ on each dithiolene ring. The resulting molecule, $Mo(tfd\text{-}COCF_3)_3$, is a relatively bulky molecular dopant shaped like a trigonal prism with a long axis approximately 1.2 nm in length and a short axis of approximately 0.6 nm. [49] It is expected that the three-dimensional shape of $Mo(tfd\text{-}COCF_3)_3$ would make it less prone to movement in the OSC compared to a dopant molecule with a planar structure such as F_4TCNQ. $Mo(tfd\text{-}COCF_3)_3$ is the molecular dopant used in the study described in section 4.2, and its molecular structure is shown in figure 3.1 e.

3.1.5 Thin-film Fabrication Using Spin Coating

OSCs are suitable to be made into thin-films for their practical applications. Since thin-films offer more mechanical flexibility than bulk materials, this form offer potential for devices that can bend and deform without permanent damage. [80, 81] The absorption coefficient is generally higher for OSCs than for silicon, meaning that the majority of incoming sunlight can be absorbed in OPVs that use OSC thin-films as active layer. [54] Additionally, although vapour deposition and sequential doping offer a better potential to preserve the OSC nanostructure than doping through mixed solution, there is also risk for a dopant gradient forming in the film between the substrate side and the side that is exposed to the dopant vapour or solution, resulting in a heterogenous distribution. [7] This gradient effect is reduced for specimens formed as thin films.

Spin coating is a well-established technique used to produce thin films with uniform thickness on flat substrates. This specimen fabrication technique is illustrated in figure 3.2. During spin coating, the solution of interest is dropped on a substrate which is accelerated up to a desired rotation speed. Common rotational speeds are of order of thousands revolutions per minute, and at this rate the inertia of the solution causes it to flow radially. During this flow, the solution will cover the substrate and the solvent will evaporate quickly. Excess solution will be ejected from the substrate edges, leaving a thin film after the complete evaporation. The final thickness of the film depends on solution properties such as viscosity and volatility, and can be controlled through spinning parameters like rotation speed and total spinning time. [82]

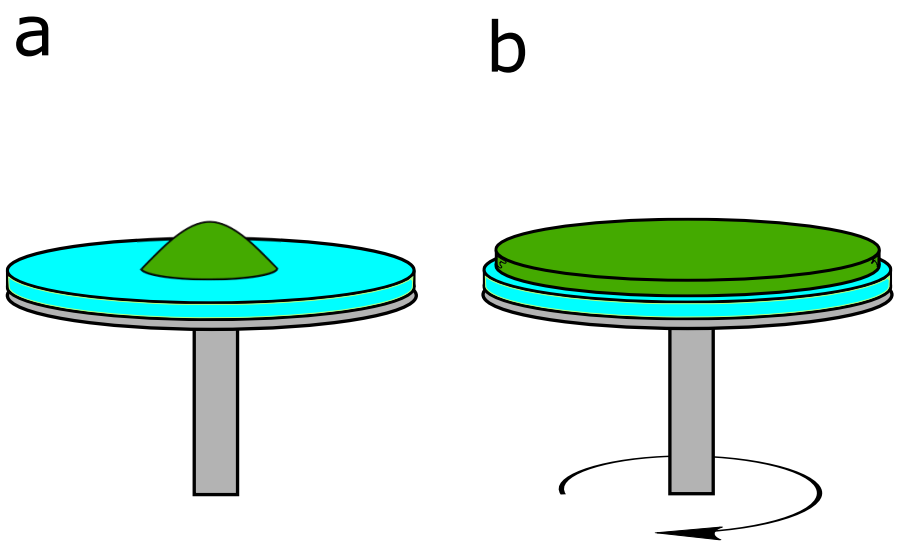

Figure 3.2: The main steps of the spin-coating specimen fabrication technique. (a) A solution is dropped on a substrate. (b) Using high rotational speeds, the solution will flow radially and form a thin-film on the substrate.

3.2 Structural Characterisation

Since lengthscales all the way down to nanometre or atomic levels are of importance for a thorough structural characterisation of organic electronics, techniques that can resolve such fine features is required. This thesis has focused on using electron microscopy for this detailed characterisation. In an electron microscope, electrons are accelerated by a high voltage and focused to an electron-dense beam using electromagnetic lenses. When this beam interacts with the investigated sample, multiple types of signals are generated that can be used for structural investigation at high spatial resolution. [18] Different forms of electron microscopes use this basic principle in different ways. This section will explain the principles of the electron microscopy techniques used, and discuss the advantages and challenges of the different methods.

3.2.1 Scanning Electron Microscopy (SEM)

SEM was used in this thesis to screen for successfully fabricated samples, to gain an overview of the sample structures and for analysis at lengthscales of 10-1000 nm. SEM is a flexible technique that allows characterisation of many different types of bulk samples. The main requirements are that the samples should not be insulating or change structure when exposed to vacuum. A schematic of the basic SEM components is shown in figure 3.3. Electrons are emitted from an electron

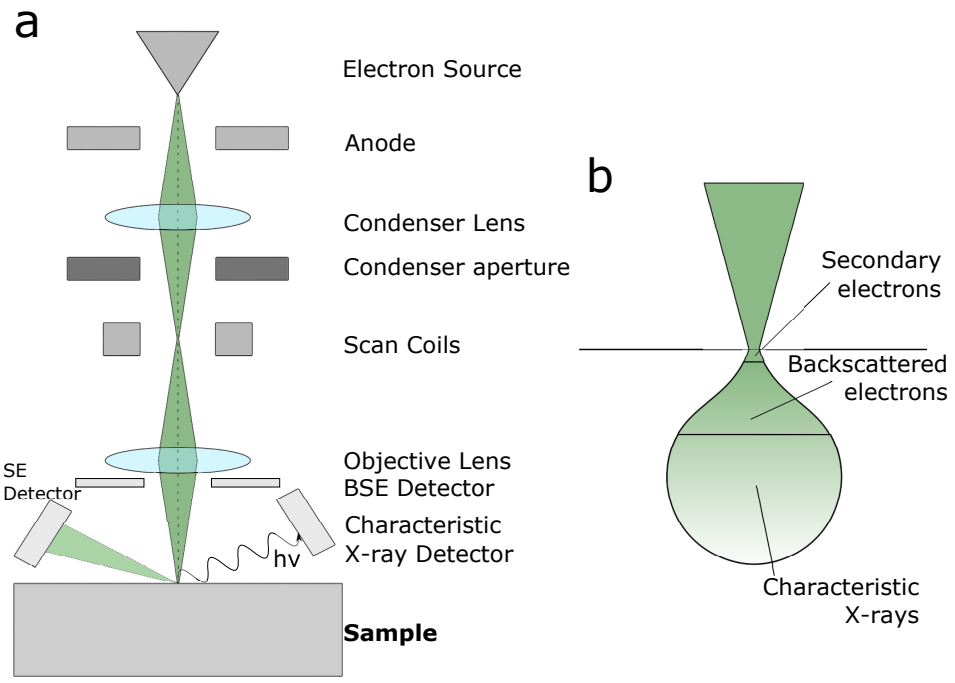

Figure 3.3: (a) A schematic of the basic SEM components and (b) three signal types that are generated when the focused electron beam interacts with the sample.

source, which is usually a thermionic gun or a field emission gun, and accelerated to high energies by an anode below the source. Energies used in SEM typically range from 1 to 30 keV. Electromagnetic lenses in the microscope column are used to focus the electrons into a beam of high electron density. In SEM, the electron beam is further focused into a fine point, an electron probe, which converges at the sample surface. Using scan coils, the probe can then be raster scanned over the sample in order generate signals at different positions. These signals are collected pixel by pixel, and can be used to form an image of the analysed sample area.

Signals in SEM

As the electron probe interact with the sample, elastic and inelastic scattering give rise to multiple types of signals that can be collected by detectors and used for structural and chemical analysis. The penetration depth of the electron beam in the sample is determined by the electron mean free path in the material. In general, a higher incident electron energy and a sample composed of lighter elements lead to a deeper penetration depth and a larger volume of interaction from

where signal can originate from. After formation, the signal also needs to escape the sample in order to reach a detector. The volumes from where different signal types can escape are not equal, leading to different effective interaction volumes. Three signals that are commonly used in SEM analysis are secondary electrons (SEs), backscattered electrons (BSEs) and characteristic X-rays. Their interaction volumes are qualitatively shown in figure 3.3.

SEs are electrons originating from the sample. High-energy electrons from the beam may inelastically interact with electrons from the sample's atoms and eject them. These ejected sample electrons are the "secondary electrons", and have significantly lower kinetic energy than the electrons from the beam. Due to these low energies, SEs can relatively easily be reabsorbed by neighbouring sample atoms. Therefore, the interaction volume of SEs is small and localised to only the first atomic layers of the sample surface. The small interaction volume and reduced signal from deeper atomic layers make SEs useful for studies of a sample's surface topography in SEM.

BSEs are electrons originating from the primary electron beam, and have higher energies than SEs. Incident electrons from the beam may elastically scatter against the sample atoms, leading to a large change in their trajectory (back-scattering). Since the energy of these scattered primary electrons is close to that of the incoming electron beam, backscattered electrons are not as easily reabsorbed by neighbouring sample atoms and their interaction volume is larger. The probability of backscattering is increased for heavier atoms, *i.e.* elements with higher atomic number Z, which therefore yield a higher BSE signal. The strong Z-number contrast makes BSEs useful for compositional studies in SEM.

Characteristic X-rays are photons that are generated as the empty states, resulting from the secondary electrons escaping the atoms, are filled by electrons from outer electron shells. The relaxation will correspond to a specific energy difference that is unique for each electronic transition in each element, and will lead to the emission of a characteristic X-ray corresponding to the relaxation energy. The element specific energies of characteristic X-rays make them useful for elemental analysis in SEM. Since photons are massless particles they have a lower probability of reabsorption than electrons, and the resulting interaction volume is larger than for SEs and BSEs. [83] The spectroscopy technique of acquiring and analysing characteristic X-rays is further explained in section 3.2.4.

All SEM analyses in this thesis were performed on a JEOL JSM 7800F Prime equipped with a field-emission gun of the Schottky type as electron source and an

Oxford X-Max 80 mm^2 detector for energy dispersive X-ray spectroscopy (EDX).

3.2.2 Transmission Electron Microscopy (TEM)

A transmission electron microscope (TEM) offers potentially higher spatial resolution than SEM, but it also adds the requirement of an electron transparent sample. Thus, this technique is not intended for bulk samples but is well-suited for detailed analysis of small sample volumes. The basic components of a TEM are illustrated in figure 3.4. Similar to SEM, electrons are first emitted from an electron source, accelerated to high energies by an anode and focused to a beam using electromagnetic lenses. TEM generally uses higher energies than SEM, with typical values ranging from 60 to 300 keV. In conventional TEM, a broad, parallell beam is used to illuminate the sample. In scanning TEM (STEM), the beam is instead focused into a small probe which converges at the sample and is raster scanned over an area, similar to SEM. Both of these modes were used for high-resolution analysis of the sample structures at the nanometre- and atomic levels. In TEM and STEM, the electrons are transmitted through the sample, producing signals through interactions with the sample atoms. The signals are used to extract high-resolution information of the analysed material.

If high-resolution imaging using transmitted electrons is desired, the sample needs to be thin. Samples suitable for TEM analysis are commonly thinner than 100 nm, and materials consisting of elements with high Z-number may require even thinner samples. Additionally, using electrons that are transmitted through a sample means that an image formed from this signal is a two-dimensional (2D) projection of a three-dimensional (3D) material. Therefore, a reduced thickness also reduces the chances of multiple overlapping features in the depth direction, leading to more clearly interpretable images. [18]

Signals in TEM

Similarly to SEM, the interaction between the electron beam and the sample will produce SEs, BSEs and characteristic X-rays in a TEM. Despite this, the most commonly used signals come from the electrons that have transmitted through the sample. These signals can be divided into three main categories. Unscattered electrons are electrons that have transmitted through the sample without being scattered or scattered to small angles, and can be collected by a detector at the optical axis below the sample. Image formation using this signal is called bright-field (BF) imaging, and is well-suited for phase-contrast imaging. In con-

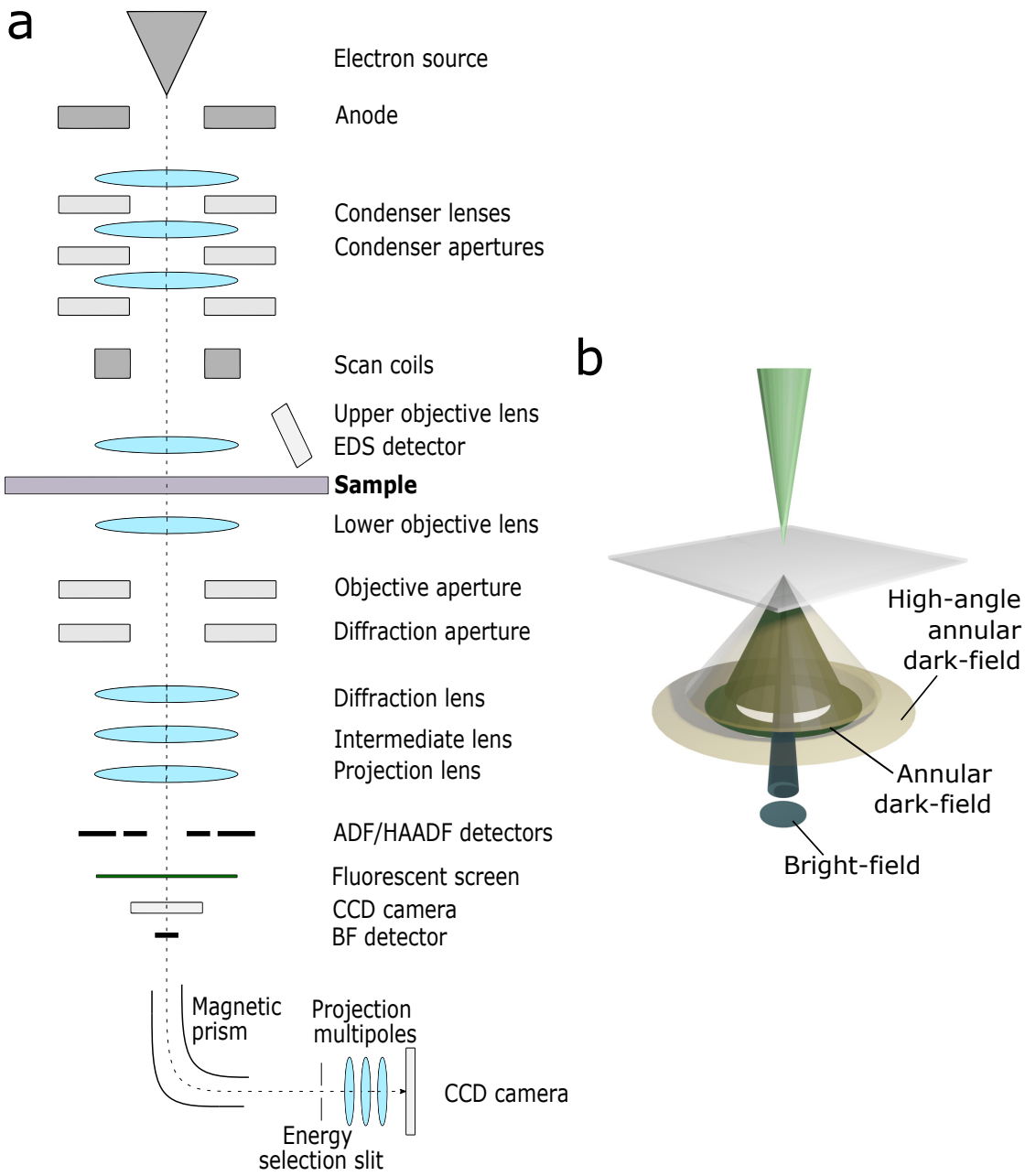

Figure 3.4: (a) A schematic of the basic TEM components and (b) three detectors that are used for collection of electrons scattered at different angle intervals when the focused electron beam interacts with the sample.

trast to BF imaging, using the signal from electrons scattered at higher angles is instead called dark-field (DF) imaging. In this thesis, BF imaging has mainly been performed in TEM mode and DF imaging has been performed in STEM mode. Scattered electrons can be detected using an annular dark-field (ADF) detector, which is ring-shaped with a circular hole in the centre in order to exclude the unscattered electrons. ADF imaging using a sufficiently large hole, or more specifically with an inner acceptance angle larger than 50 mrad, is termed high-angle annular dark-field (HAADF) imaging. [18] The majority of the signal at these high angles is due to elastic electron scattering close to the nuclei of the sample atoms, making HAADF imaging more sensitive to variations in Z-number compared to BF- and ADF imaging. The practical Z-dependence of HAADF-STEM signal varies between $Z^{1.6}$ and $Z^{1.9}$, meaning that heavy elements will produce a strong contrast when surrounded by lighter elements. HAADF imaging is often termed Z-contrast imaging due to this dependency. Denser or thicker regions in a material means more mass to transmit through, which also leads to increased scattering and a higher HAADF signal. [84] Another advantage of using HAADF imaging is that coherent scattering is suppressed for electrons that are scattered to these high angles, which minimises the image contrast from Bragg scattering. Imaging crystalline samples at angles that fulfils Bragg's law gives rise to Bragg scattering, meaning that the contrast of certain regions may change at these angles and structures risk being misinterpreted in the images. [85] The suppression of Bragg scattering in HAADF images is important when performing electron tomography, which is discussed in section 3.2.3. Finally, inelastically scattered electrons are electrons that have scattered and deposited energy in the sample, and can be used as signal for a spectroscopy technique called electron energy-loss spectroscopy (EELS). As an electron is inelastically scattered, it may lose energy corresponding to the state it interacted with. Information such as elemental distribution and the chemical state of the element can be obtained using EELS in a TEM. [86]

All STEM analysis in this study was mainly performed using a FEI Titan 80-300 at an electron acceleration voltage of 300 kV. The instrument is equipped with a Schottky field-emission gun and a CEOS probe aberration corrector, allowing the STEM electron probe to be focused to a diameter of 70 pm. HAADF-STEM was selected as the main imaging mode due to that the heavy elements in the Mo(tfd-$COCF_3$)$_3$ dopants produced a strong Z-contrast compared to the polymer p($g_4$2T-T), enabling the dopant molecules to be imaged with high precision. BF-TEM in the study described in section 4.1.3 was performed using a FEI Tecnai T20 at 200 kV acceleration voltage equipped with a LaB_6 filament. HAADF-STEM imaging and analysis using characteristic X-rays in the study in section 4.1.2 was performed using a JEOL MonoNEOARM200F at 200 kV. This instru-

ment has a Schottky field-emission gun, an ASCOR probe aberration corrector and a CETCOR image aberration corrector and is equipped with dual EDX detectors for analysis of characteristic X-rays.

3.2.3 Electron Tomography

Although it is possible to achieve high spatial resolution analysis using TEM, a limitation for structural analysis is that a transmitted signal will yield 2D projections of the sample and information regarding depth distribution of features will not be retained. This can complicate the interpretation of data and may even lead to wrong conclusions regarding the sample structure. A method developed to solve this problem is electron tomography. The base principle of tomography is to retain the 3D structure of an object by acquiring a series of 2D images at different tilt angles. By tilting the sample relative to the electron beam, the different images will contain information about the object from different viewpoints. Mathematical algorithms can then be used to reconstruct the full 3D volume from the acquired tilt series. [87] The algorithm used for reconstruction may vary, but the principle is based on the projection theorem (also known as the Fourier slice theorem). The theorem states that a projection of an object at a certain angle is equivalent to sampling of a central plane at the same angle in the object's 3D Fourier transform. This means that the series of projections in real space at different angles can be Fourier transformed, used to fill in the corresponding angles in its 3D Fourier transform, and finally inverted to reconstruct its 3D structure in real space. [88] A cartoon of how a 3D object is reconstructed from a 2D tilt series is shown in figure 3.5.

The resolution of tomographic reconstructions is not isotropic for the different axes, and will besides the microscope resolution also be limited by the number of images in the tilt series and its span of angles. With this in mind, one might reason that a tilt series over the full $\pm 90^{\circ}$ rotation over a sample with extremely fine rotation increments should lead to the best possible 3D resolution for the reconstructions. In practice however, the maximum tilt angles are limited by shadowing from the TEM sample holder, grid or other features in the sample. The angles outside the maximum tilt lead to a missing wedge of information that can lead to an elongation along the wedge direction and may introduce artefacts for the reconstructed features. [87] Although no such restrictions exist for maximum number of images in the tilt series, exposing the same area of the sample for too high dose of the electron beam may damage the sample features and irreversibly change the structure during the acquisition. Sample damage from the electron beam is discussed in further detail in section 3.2.5. In practice, tilt steps of 1-2° with a tilt range

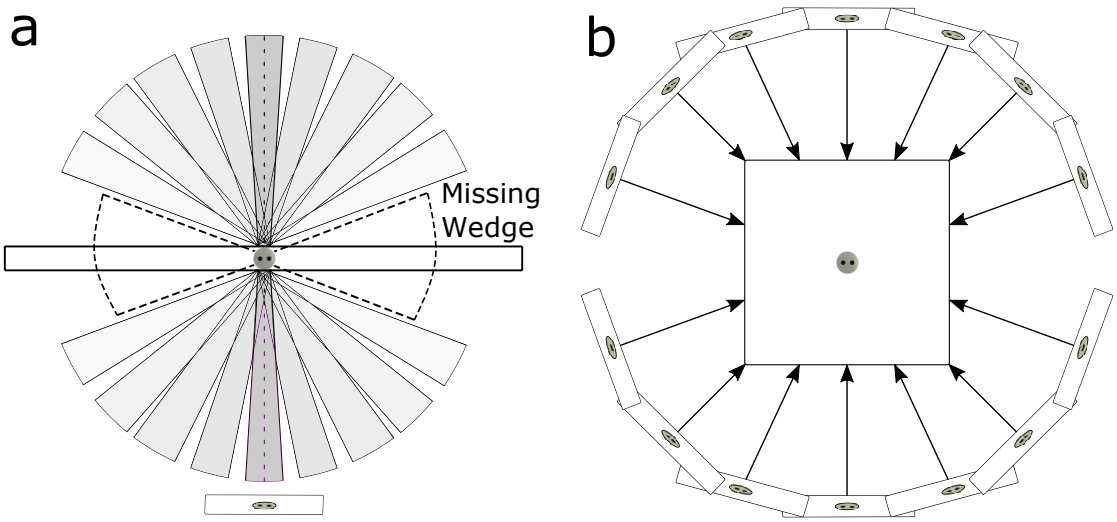

Figure 3.5: Cartoon illustrating the principle of electron tomography, where (a) a series of 2D projections of an object from different tilt angles is used to (b) reconstruct its 3D structure.

of $\pm 70^{\circ}$ are commonly used to get sufficient results, which should theoretically produce an elongation factor smaller than 1.3. [89]

Direct reconstruction through inverse Fourier transform have shown to be computationally expensive and also requires a continuously varying function from series based on discrete sampling, which necessitates an interpolation that can affect the reconstruction results. Instead, the Radon transform has been widely used for tomography, which avoids the complications with inverse Fourier transform and the required interpolation. However, reconstructions using inverse Radon transform, commonly called back-projection, are known to produce 3D reconstructions with blurred fine details due to oversampling of information at low spatial frequencies and undersampling at high frequencies from the tilt series. This has been solved by convolving the reconstruction with a weighting filter that increases amplitude at higher frequencies, resulting in the popular weighted back-projection (WBP) reconstruction algorithm. A more modern approach is to iteratively reconstruct the volume, which is used in the algorithm simultaneous iterative reconstruction technique (SIRT). The main idea behind iterative algorithms is that the original TEM images can be seen as ideal 2D projections of the sample, but the missing information due to only a discrete number of samplings may lead to errors in the final reconstruction. By iteratively comparing linear re-projections of the reconstruction with the original images, such artefacts can be removed from the output 3D structure to improve the results. [89]

A requirement for the reconstruction algorithms is that changes in image intensity should be linearly proportional to the change in thickness. This can make BF tilt series difficult to use for tomography on crystalline samples due to Bragg contrast at certain angles. However, this is not a problem for tilt series using HAADF imaging, which suppresses coherent scattering as described in section 3.2.2. Hence, HAADF-STEM images series are used for all tomography reconstructions in this thesis work.

3.2.4 Energy Dispersive X-ray Spectroscopy (EDX)

As described in section 3.2.1, when the primary electron beam causes inner shell electrons to be ejected from the sample atoms, electrons from outer shells will undergo relaxation to the vacant lower energy states. The energy difference of the two electronic states may give rise to a characteristic X-ray photon with a unique energy specific for each electronic transition in each element. This process is illustrated in figure 3.6. The spectroscopy technique of collection and analysis of these characteristic X-rays is known as EDX, and has been widely used as a reliable technique for compositional analysis. In SEM and STEM, the raster scanning of the beam can be utilised to gather the X-ray signal pixel by pixel and correlate this to the beam position to combine the information of elemental composition with high spatial resolution. This process in known as spectral imaging using EDX (EDX-SI). As mentioned in section 3.2.1, characteristic X-rays are associated with a larger interaction volume in SEM, but the higher acceleration voltage and thin samples used in TEM significantly limit this signal spread and sub-nanometre resolution of the elemental distribution can be obtained. Modern software has made EDX analysis streamlined and efficient, but it is important to know the underlying processes in order to acquire high-quality data.

In general, EDX analysis of light elements can be more challenging than analysis of heavy elements, especially when the elemental concentration is low. This is due to that relaxation of outer-shell electrons will not always lead to emission of characteristic X-rays, instead Auger electrons may be emitted that are not detected by EDX. The probability of characteristic X-ray emission increases with atomic number, and thus a higher signal per dose is achieved for heavier elements. [90] Furthermore, the characteristic X-rays are sent out in random directions from the sample, and the limited space in the sample chamber allows only a fraction of the X-rays to reach the EDX detector. After reaching the detector, X-rays are separated (or "dispersed") according to their energy and displayed in a spectrum as number of counts in different spectrometer channels correspinding to preset en-

ergy intervals. The detected energy values are electronically identified as electron transitions of different elements. Such an EDX spectrum is shown in figure 3.6. It should be noted that the detection and processing steps involve statistical steps that lead to a fundamental limitation in energy resolution. Current EDX detectors have an energy resolution of the order of 100 eV, leading to peaks with Gaussian shapes instead of sharp lines and may give rise to peak overlaps for X-rays with similar energy values. In particular, the low energy values of light-element X-rays mean a higher risk of overlap, making it difficult to distinguish the different elements. The lower characteristic X-ray yield and overlapping peaks can make it challenging to perform EDX analysis of low Z-number materials such as OSCs. Combined with sample beam damage, which is discussed in section 3.2.5, it can be difficult to obtain reliable EDX spectra or maps for these systems. However, modern improvements in spectrometer efficiencies and larger detector collection angles are making EDX analysis increasingly applicable for OSCs. [18]

The intensity of each peak in a EDX spectrum is related to the concentration of corresponding element. Thus, measuring the relative strength of each spectrum peak enables quantitative EDX analysis. For a reliable quantification, a high peak-to-background ratio should be obtained for all characteristic peaks so that the background signal can unambiguously be subtracted. [18] After subtraction, the true intensity I of each characteristic peak obtained through integration. If two elements are present in the spectrum, the relative concentrations of the elements C_A and C_B can be calculated with the Cliff-Lorimer equation

$$\begin{aligned} C_A/C_B &= k_{AB} I_A/I_B \\ C_A + C_B &= 1 \end{aligned} \tag{3.1}$$

where k_{AB} is a non-constant sensitivity factor often termed the Cliff-Lorimer factor. k_{AB} depends on the elements, absorption of X-rays and X-ray fluorescence in the sample. [91] Although simple in concept, obtaining accurate k-factors can be difficult in reality. Modern EDX software often come with pre-determined Cliff-Lorimer factors. These are often sufficient to estimate the material composition, but highly accurate quantification may require other methods. [18, 92] Modern advancements in detectors and post-acquisition processing are constantly improving the accuracy of EDX, which have in recent years reached the milestone of mapping chemical elements with atomic resolution. [93, 94] EDX was performed to confirm the elemental compositions of all samples studied in this thesis, and was of specific importance in the study described in section 4.1.2 where EDX mapping was used to determine the separation of components in the bilayer film.

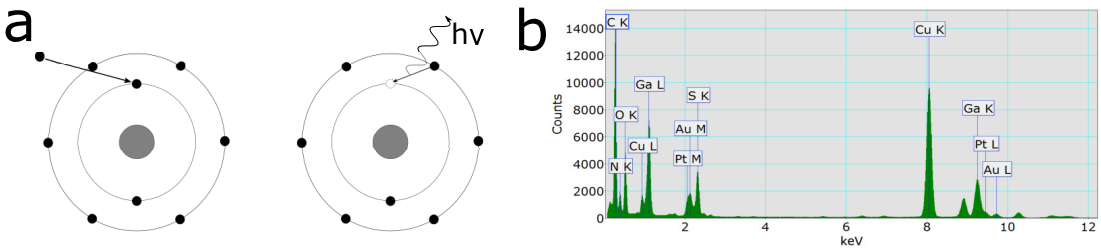

Figure 3.6: (a) Mechanism for characteristic X-ray generation: An incoming electron knocks out a sample electron from an inner electron shell. This allows an electron from an outer shell to relax to the inner shell and emit a X-ray corresponding to the relaxation energy. (b) Example of an EDX spectrum obtained by analysing characteristic X-rays.

3.2.5 Minimising Radiation Damage on Samples

Modern electron microscopes are capable of achieving an incredibly high spatial resolution, but the high-energy electron beam's interaction with the sample may cause radiation damage that will limit the analysis of the true state of the material. It is important to understand these damaging interactions in order to limit their extent, especially for soft materials like OSCs. This section will list common damage mechanisms and methods to minimise their effect.

Damage from Elastic Scattering

Elastic scattering by electrons from the primary beam and the sample atoms' nuclei may lead to so called knock-on damage. The total amount of energy is conserved in an elastic interaction, but energy can still be transfered from beam electrons to the nucleus followed by a significant change in the electron trajectory. This transferred energy may be sufficient to displace the sample atoms, permanently rearranging the structure or sputtering them away which will result in mass-loss. The displacement of sample atoms due to elastic scattering from the electron beam is referred to as knock-on damage. Knock-on damage is commonly the dominant damage mechanism during analysis of conducting materials such as metals. The effect is decreased at lower beam energies and for higher atomic weights. All atomic sites are also not affected equally by the scattering, for example a surface atom may more easily be displaced than an atom in the bulk of a sample. The minimum energy required to displace an atom is called the displacement energy, which is dependent on atomic weight, bonding with surrounding atoms and location within the sample. A maximum transfer energy lower than the displacement energy means a drastic reduction in knock-on damage. Thus, it is possible to lower the beam

acceleration voltage below certain threshold values in order to make knock-on damage negligible. [95]

Damage from Inelastic Scattering

When the incident electrons change kinetic energy due to interaction with the sample atom, it is considered inelastic scattering. This change is usually a loss in electron energy, which can vary from a few electron volts up to hundreds of electron volts and significantly affect the sample. Inelastic scattering commonly results in ionisation of sample atoms, excitation of phonons or excitation of valence- or conduction electrons in the material. Although such interactions provide useful signals that can be analysed in the microscope, they also result in radiolysis, heating and electrostatic charging, which are the dominant sources of damage for soft materials such as OSCs. [96]

Sample heating due to inelastic scattering can be problematic for materials with low thermal conductivity, and combining this with a low thermal stability may result in significant decomposition due to the local rise in temperature. Similarly, electron beam interactions may cause a build-up of charges in poorly electrically conducting materials, leading to local potential differences that may result in sample damage. Radiolysis, or ionisation damage, occurs when an exited sample atom or molecule do not return to its original electronic state upon deexcitation. This results in permanent changes in atomic or molecular structure due to breaking of chemical bonds or cross-linking between new species. Bonds between C- and H atoms are easily broken in organic samples, and the reformation of bonds prevents hydrogen from rebinding which leads to mass-loss. As opposed to knock-on damage, there is no threshold in acceleration voltage where radiolysis is significantly reduced. Instead, the effect from radiolysis increases at lower acceleration voltage, meaning that the beam energy has to be carefully selected for different samples to minimise damage from both mechanisms. The cross-section of radiolysis is several orders of magnitude higher than for knock-on damage, so although damage through elastic scattering do occur in organic samples, it tends to be dominated by inelastic effects such as radiolysis. [19] A recent study of beam sensitive phosphorene showed that radiolysis can be reduced by protective layers such as graphene. Materials like graphene can both suppress knock-on damage by acting as a net to reduce sputtering of atoms and suppress radiolysis via fast charge transfers due to its excellent transport properties. The authors showed that encapsulating phosphorene in graphene increased the sample durability to approximately 13 times higher than the bare material. [97]

Heating and charging are direct dose rate dependent effects, meaning that the total electron dose is less important than the dose rate. Higher electron dose rates mean that heat or charges can not be transported away at a sufficient pace, leading to a rise in local temperature or electrostatic potential and eventual decomposition of the sample. For direct dose rate effects there may exist a threshold rate for when build-up occurs, so reducing dose rate below this can reduce the damage to negligible levels. For radiolysis, however, only the total dose is relevant and a larger current density over a shorter time should produce a similar amount of damage. Therefore, a critical dose, D_c, can be defined to quantitatively measure the material's sensitivity to damage. Since radiolysis in TEM can be approximated to follow first-order decay kinetics $S = S_0 e^{(-D/D_c)}$, for initial and measured signals S_0 and S at dose D, the critical dose can be determined as the dose when the signal reaches $1/e$ of its initial value. As an example, aromatic hydrocarbons usually have a higher D_c than aliphatic hydrocarbons due to resonance stabilisation of the phenyl rings. Finally, a material may also exhibit a decreased dose sensitivity for higher dose rates, *i.e.* an inverse dose rate effect. An inverse dose rate dependence favours the use of higher currents in the TEM in order to outrun damage in the sample. [19]

Secondary Damage Effects

In recent years it has been noted that D_c for conjugated polymers may first increase and then decrease as a function of dose rate, *i.e.* showing first an inverse and later a direct dose rate dependence in different dose rate regimes. It has been proposed that this behaviour can arise due to slow, diffusion limited processes from secondary reactants. As bonds are broken from radiolysis, some resulting species may start to react with their surroundings in a cascading manner that breaks down the material. These secondary processes should be diffusion limited, meaning that it is possible to outrun the damage with increased dose rate. On the other hand, too high dose rate can result in local heating, leading to an increased rate of diffusion and thus more damage. [98]

The extent of damage from secondary species is complex and not yet fully understood. It has been noted that cryogenic conditions can reduce sample damage in TEM, which could be due to suppression of atomic motion after bonds are broken or lowering the rate of diffusion for secondary reactants. A recent study has shown that damage can also be suppressed by adding antioxidants to the sample in order to neutralise reactive species before they break down the material. The study showed increased D_c for three OSCs after addition of antioxidants, even without the additives being incorporated into crystals, highlighting the importance of sec-

ondary damage processes for this type of material. The increased material stability allowed the $\pi - \pi$ stacking to be resolved in one of the OSCs, which had previously not been possible due to beam damage. [98]

3.3 TEM Sample Preparation

This section will present the sample preparation techniques used in this thesis in order to obtain high-quality OSC thin-film samples for TEM analysis. The following two methods will be discussed: the float-off technique from spin coated thin-films and the lift-out technique using a combined focused ion-beam and scanning electron microscope (FIB-SEM).

3.3.1 Float-off

As discussed in section 3.1.5, spin coating is a common method to fabricate thin-film specimen of OSCs. By adding additional steps to the spin coating procedure, it can be used to prepare samples for TEM analysis. This is commonly referred to as the float-off technique, and is illustrated in figure 3.7 a-b. The float-off technique is done by spin coating a sacrificial thin-film on the substrate, and subsequently a film of the material of interest. By immersing the substrate and the two layers into a dissolving agent for the sacrificial layer, for example deionised water, the second layer will be released and can float up to the water surface. Finally, the floating thin-film can be directly picked up on a TEM grid using tweezers and transferred to a microscope for analysis. [99, 100] The float-off technique is the main sample preparation method used in this thesis to prepare OSC thin-films.

3.3.2 Focused Ion Beam - Scanning Electron Microscopy (FIB-SEM) Lift-out

Another method for preparing thin OSC samples for TEM analysis is through lift-out using a FIB-SEM. The lift-out procedure is illustrated in figures 3.7 c-e. A FIB-SEM is a dual-beam instrument that combines the electron beam of a scanning electron microscope with an ion-beam that use a similar principle. The most common choice of ion is Ga^+, meaning that the particles in the ion-beam have a significantly higher mass than those in an electron beam. After aligning the electron beam and the ion-beam in a FIB-SEM, it is possible to simultaneously use electrons to image an area and use ions to perform manipulations such

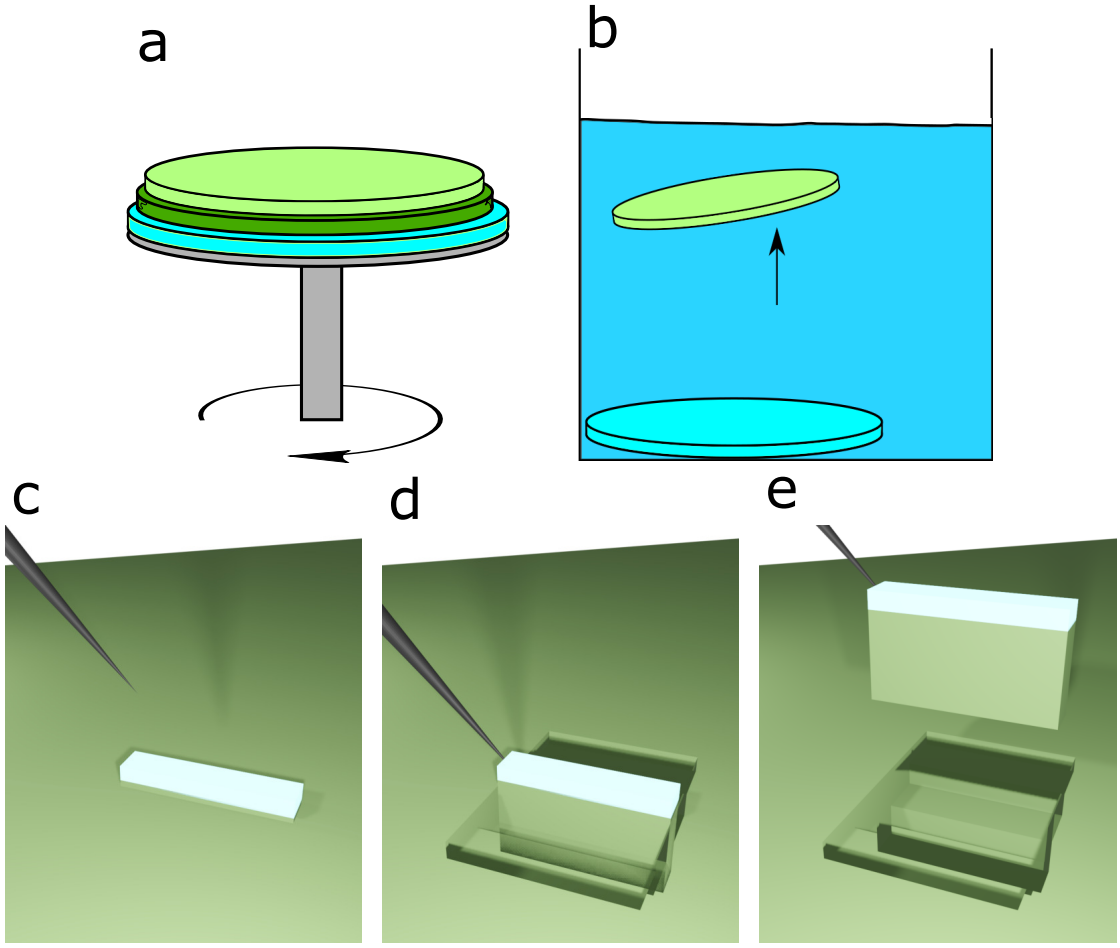

Figure 3.7: The main steps of the two sample preparation techniques: float-off and FIB-SEM lift-out. (a) Two thin films are fabricated through spin coating: a sacrificial film and the film of interest on top. (b) Immersing the substrate and the films in a dissolving agent will release the film of interest, which will float to the surface. (c) An area of interest is identified using a FIB-SEM and a protective layer is deposited on top. (d) The area surrounding the area of interest is milled away, freeing up a lamella of the area of interest which is welded to a micromanipulator. (e) The lamella is cut loose from the sample and lifted out using the micromanipulator.

as sputtering away material according to preselected patterns. Additionally, if the FIB-SEM is equipped with a metal evaporation source, commonly a gas injection system (GIS), the ion beam can be used to deposit a protective metal layer on top of selected areas in the sample. [101]

Using a FIB-SEM, it is possible to select a specific region of interest in a sample, mill out its surroundings, lift out the selected region and attach it to a TEM grid according to the following procedure. After selecting an area for lift-out, a metallic (or carbon-based) layer is deposited to protect the area from subsequent exposure to the ion beam. Using the GIS, an organometallic precursor gas is ejected over the area and decomposed using the ion beam during a predetermined time. A frequent choice of metal is Pt, where a 1 μm thick layer is normally deemed sufficient for protection. To prevent ion and Pt implantation in the material of interest, the first initial nm of protective layer may also be deposited using the electron beam. The area surrounding the protective layer is then milled away using the ion beam, forming a thin slice, a lamella. By tilting the sample relative to the ion beam, the area underneath the lamella may also be milled away at a chosen depth. Before completely cutting loose the lamella, a needle-shaped micromanipulator is inserted until it is barely touching the sample, and the lamella is welded to the micromanipulator using the GIS. The lamella is cut loose and moved to a TEM grid, which it is welded to and removed from the micromanipulator. After being securely welded to the TEM grid, final thinning is carefully performed on the lamella to make it sufficiently thin for TEM analysis. The lamella is rotated 90° during the transfer to the TEM grid, meaning that the in-plane orientation in the TEM will be a cross-section of the sample. Due to this, FIB-SEM lift-out is an excellent method to prepare cross-sections for analysis of depth profiles. [101]

Comparing FIB-SEM lift-out to spin coating and float-off as a sample preparation technique for OSCs, lift-out using FIB-SEM offers the advantage of selective analysis over an area of the researcher's choice, and lift-out is necessary if analysis of a cross-section in required. However, it is a time-consuming sample preparation technique and the resulting samples are small, which may introduce an operator bias when studying the material. Also, thinning soft materials such as OSCs to only a few tens of nanometers can be difficult in a FIB-SEM, meaning that the thickness of the spin-coated sample has the potential to be smaller. [102] Ultimately, there are advantages and disadvantages of both methods and the choice of sample preparation technique is often determined by the type of analysis that will be performed on the material. In this thesis, the FIB-SEM lift-out technique was used to create cross-section samples of the bilayer film discussed in section 4.1.2.

4 Results and Discussions

As discussed in section 2.3, the performance of organic electronic devices is connected to the material nanostructure. This chapter shows and discusses results from electron microscopy studies of organic semiconductor systems. Structural details of interest are aggregation characteristics, interface structures, phase distribution and dopant cluster morphology, which are studied in 2D. Furthermore, the analysis is extended to 3D in order to visualise the complete sub-nanometre dopant distribution in an OSC. The information regarding nanostructure is in turn interpreted and correlated to electronic properties of the materials.

4.1 Characterisation of 2D Nanostructure

Using TEM to image samples in transmission will yield 2D projections of a 3D sample. Despite this limitation, 2D TEM imaging can be sufficient to determine the relevant nanostructure features in thin-films. This section is centered around the results from high-resolution electron microscopy imaging and spectroscopy of the nanostructure of different OSC systems. Important details are aggregation characteristics, phase distribution, dopant cluster morphology and interface structure of OSC blends. The systems of interest are thin-films of the copolymer p[p($g_4$2T-T)-co-U] and neat p($g_4$2T-T), a bilayer structure of BBL and p($g_4$2T-T), a BHJ of TQ1:$PC_{71}BM$, and p($g_4$2T-T) doped with Mo(tfd-$COCF_3$)$_3$.

4.1.1 Aggregation Characteristics of copolymer p[p($g_4$2T-T)-co-U]

As described in section 2.4.2, practical application of TEGs requires thermoelectric materials with suitable electrical and mechanical properties. Optimal mechanical properties are a balance between sufficient flexibility to deform without fractures and sufficient robustness to form free-standing films. For this purpose, the synthesis of a material consisting of p($g_4$2T-T) blocks and hard linker segments of urethane is reported in paper I. High resolution STEM was performed on the resulting copolymer p[p($g_4$2T-T)-co-U] and compared to neat p($g_4$2T-T) in order to

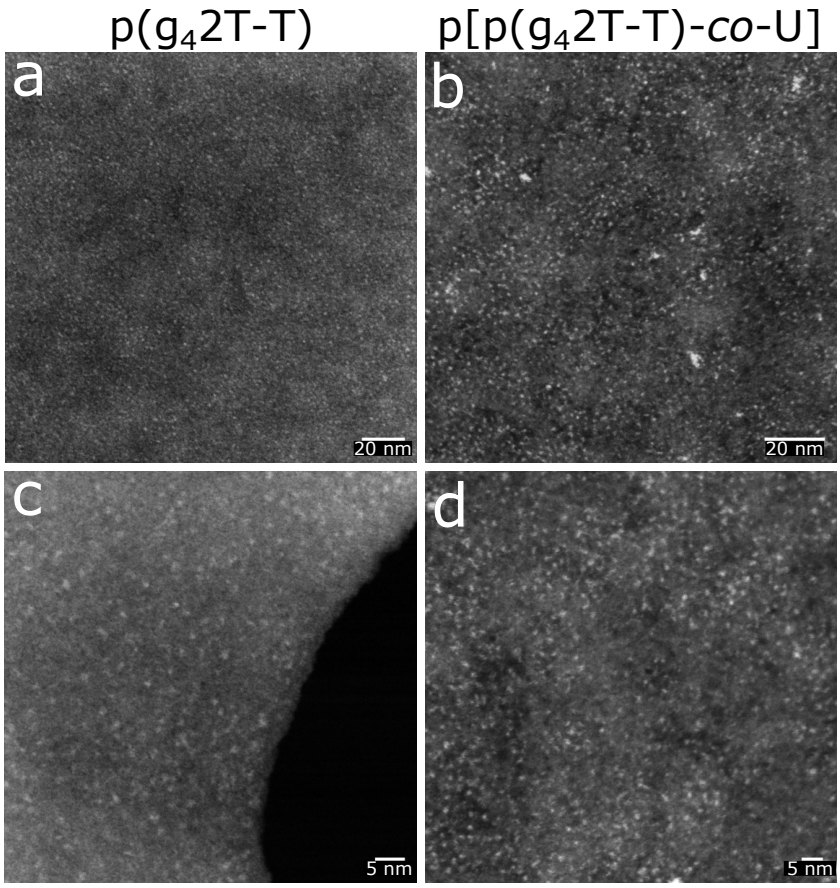

Figure 4.1: HAADF-STEM images of (a, b) p($g_4$2T-T) and (c, d) p[p($g_4$2T-T)-co-U]. Both neat polymer and the copolymer display the same granular texture but lacks large aggregations, indicating that the urethane units are introduced without significant disruption of the p($g_4$2T-T) nanostructure.

study the nanostructure of the materials. Samples of p($g_4$2T-T) and p[p($g_4$2T-T)-co-U] were fabricated through the spin coating and float-off method described in section 3.3.1, resulting in thin-films that were picked up on TEM grids and transferred to the microscope for imaging. Analysis in HAADF-STEM mode at 300 kV resulted in the images shown in figure 4.1.

In this figure, it can be seen that both materials contains bright features of single-nanometre sizes across the film. These features may form as a result of micellar-like structures that have previously been inferred for pure p($g_4$2T-T). [40] Distinct domains of urethane blocks, approximately 5 nm long, were expected in the copolymer. These should be discernible due to their denser and more ordered structure,

but could not be resolved during the analysis. A possible reason for this could be that the domains are distributed evenly in all three dimensions, making it difficult to distinguish them in projection in samples where multiple blocks may be overlapping. Importantly, no large aggregations of the different components can be observed in these images. The lack of aggregates indicate that the urethane units are successfully added to the p($g_4$2T-T) without any significant disruption in the polymer nanostructure. Complimentary measurements show that the successful inclusion of the urethane segments only leads to a slight reduction of electrical properties but a significantly enhanced robustness for the copolymer. This robustness is sufficient to form a free-standing solid, which makes the copolymer p[p($g_4$2T-T)-co-U] a promising material for applications such as for the active material in thermoelectric generators.

4.1.2 Interface Structure of Bilayer p($g_4$2T-T):BBL

Sections 2.2 and 2.3 discusses that the difficulties in controlling the position of molecular dopants may lead to low long-term stabilities and eventual loss of performance due to dopant aggregation. Ground-state charge transfer presents a way to ignore the drawbacks of adding dopants by instead matching the levels of ionisation energy and electron affinity of two OSC components in a system. Upon physical contact, an electron transfer will then occur spontaneously between the components in the electronic ground state without any external stimuli, resulting in an interface that can act as a charge transport layer. The study in paper II reports the first time a ground-state charge transfer has been observed for an all-polymer system by combining the polymers p($g_4$2T-T) and BBL. The contact between the polymers resulted in a quasi-two-dimensional interface with a drop in electrical resistance of several orders of magnitude compared to that of the pure polymers. Kinetic Monte Carlo (KMC) simulations indicate that the charge transport is confined to a narrow interface between the components that is only a few nanometres wide. Thus, a sharp interface between the polymers is crucial in order to form a continuous highly conductive transport layer through the material. Bilayer films were prepared for electron microscopy study by spin coating the p($g_4$2T-T) and BBL on a gold electrode. In order to image the depth profile and the interface of the bilayer, cross-sections had to be prepared from the sample using the FIB-SEM lift-out scheme presented in section 3.3.2. The TEM lamella produced from the lift-out was transferred to a TEM to be imaged using HAADF-STEM at 200 kV, revealing a structure seen in figure 4.2.

A clear layered structure is visible in the figure, where the interfaces between

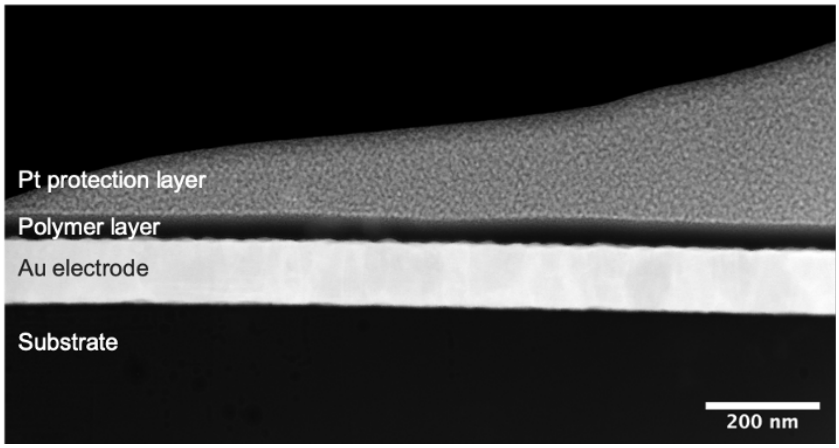

Figure 4.2: ADF-STEM image recorded at 200 kV acceleration voltage showing the different layers of the spin coated bilayer p($g_4$2T-T):BBL on a Au electrode. A protective layer of Pt was deposited on top of the polymers.

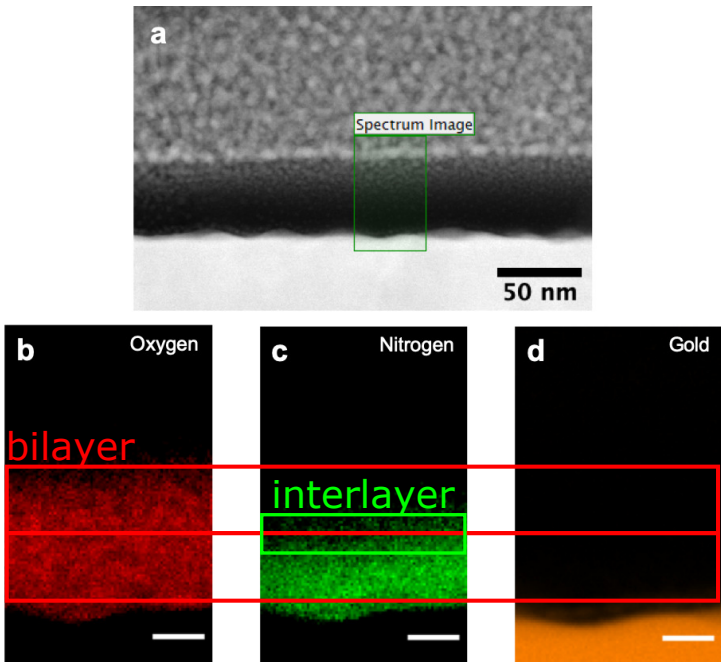

Figure 4.3: EDX mapping of the oxygen and nitrogen distribution in bilayer p($g_4$2T-T):BBL, taken at 200 kV acceleration voltage. (a) ADF-STEM image of the bilayer. The area for EDX analysis is marked "Spectrum Image". (b) Oxygen map. (c) Nitrogen map. (d) Gold map. Scale bars in (b)-(d) are 10 nm.

substrate, gold electrode, polymer layer and the platinum protection layer from the lift-out procedure are clearly visible. However, the low contrast of the two polymer layers made it difficult to distinguish their interface directly through HAADF-STEM imaging. Instead, the chemical differences was utilised by performing EDX-SI by acquiring an EDX spectrum for each pixel in a designated area, resulting in the data displayed in figure 4.3. The maps displaying the distribution of chemical elements in area indicate the presence of oxygen in the entire polymer layer, while nitrogen only is present in the lower part. Since nitrogen is a component of BBL but not p($g_4$2T-T), this proves that the polymers remain separated in the bilayer. Furthermore, the signal from nitrogen ends sharply, with an interlayer that is only a few nanometres wide. These results experimentally confirm that a continuous transport layer can form at the polymer interface due to ground-state charge transfer. The highly conductive interfacial regions were maximised by blending the two polymer components into a BHJ, resulting in a bulk conductivity four to five orders of magnitude higher than that of the pure polymers.

4.1.3 Phase Distribution Data of TQ1:$PC_{71}BM$ BHJ for Simulations

Accurate simulations are crucial for the understanding and development of novel materials for organic electronics. KMC has proven to be a powerful tool to study the charge carriers dynamics for OPVs, but has had difficulties to correctly simulate the current voltage (J-V) curve under illumination. Modelling the J-V curve is important since it is a key part of describing the performance of an OPV. A solution to this problem is presented in paper III by calibration of a KMC model using real experimental data. A main result of this study is that realistic data of the nanostructure is required in order to take into account recombination effects that may occur due to the phase distribution. For this purpose, electron microscopy analysis was performed on a BHJ of the polymer TQ1 and the fullerene $PC_{71}BM$. Free-standing thin-films were prepared on TEM grids using the spin coating and float-off method described in section 3.3.1. BF-TEM imaging at 200 kV revealed a granular structure with low contrast regions approximately 100 nm in size seen in figure 4.4. These low contrast regions were attributed to fullerene-rich domains due to their higher density.

However, since diffraction contrast from crystalline regions can make it difficult to interpret BF-TEM images with certainty, complimentary HAADF-STEM imaging was also performed on the same sample at 300 kV. The similar structures seen with an inverted contrast in figure 4.4 indicate that the observed features are

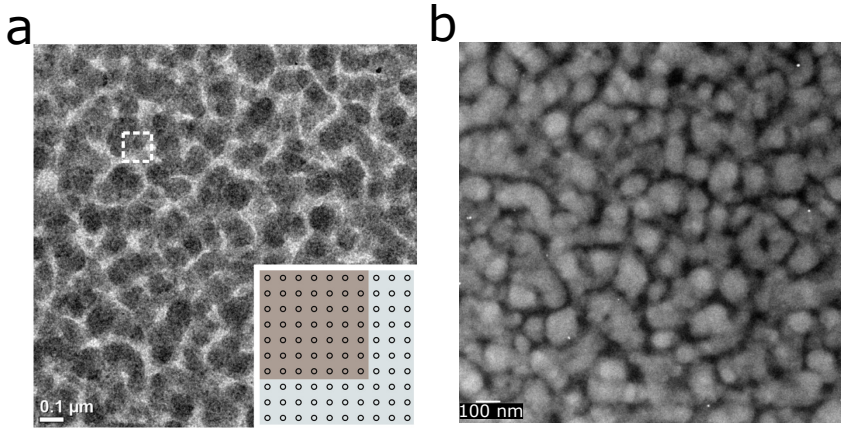

Figure 4.4: Phase distribution of TQ1:$PC_{71}BM$. (a) BF-TEM image of a TQ1:$PC_{71}BM$ BHJ and numerical implementation of the nanostructure (inset). The low contrast $PC_{71}BM$ aggregates are assumed in the KMC model as 7 x 7 inclusions in a 10 x 10 unit cell representing the mixed phase of TQ1 and $PC_{71}BM$. The dashed square shows a region that is reasonably captured by this model structure. (b) Complimentary HAADF-STEM imaging on the same sample, showing similar features as in (a) but with an inverted contrast.

correctly interpreted as aggregates of the fullerene $PC_{71}BM$. The data of the blend phase distribution acquired from the electron microscopy images were included in the KMC models in order to tune the recombination yields to more realistic rates. The fully calibrated model were able to fully describe the J-V curve of a disordered OPV under illumination of light. The results from this study highlights the importance of collaborative work between theoretical simulations and data acquired from experimental observations in order to investigate and improve future materials for organic electronics.

4.1.4 Cluster morphology of p($g_4$2T-T) doped with Mo(tfd-$COCF_3$)$_3$

As was shown in section 4.1.3, experimental data of the realistic material nanostructure can provide important contributions to material property simulations and improve the accuracy of their results. TEM has the potential for a sufficiently high resolution to directly image the dopant distribution in OSCs. However, OSCs and dopant molecules commonly contains elements of similar atomic number, resulting in a low contrast between the components. Paper IV presents the study of the low average Z-number OSC p($g_4$2T-T) doped with the high average Z-number molec-

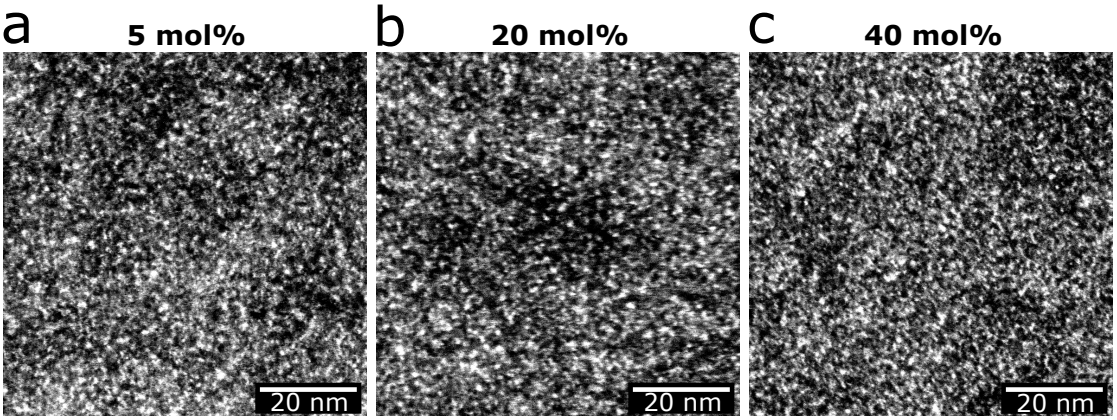

Figure 4.5: 300 kV HAADF-STEM images of representative areas of films with (a) 5 mol%, (b) 20 mol% and (c) 40 mol% Mo(tfd-$COCF_3$)$_3$ dopant concentrations in p($g_4$2T-T. The high intensity features seen in the images are direct visualisations of the dopants.

ular dopant Mo(tfd-$COCF_3$)$_3$ with different doping concentrations. Doping was performed by the mixed-solution method and thin-films samples were prepared according to the spin coating and float-off method explained in section 3.3.1, yielding free-standing TEM samples. The dopant concentrations were 5 mol%, 20 mol% and 40 mol%, respectively. Figure 4.5 shows HAADF-STEM images of the nanostructure of the analysed samples.

The high average Z-number of Mo(tfd-$COCF_3$)$_3$ (≈ 20.0) compared to p($g_4$2T-T) (≈ 7.7) should lead to a significant Z-contrast in HAADF-STEM mode. Thus, the high contrast features seen in the figure are assumed to be dopant molecules that are being imaged directly. However, it is difficult to draw conclusions regarding the complete dopant distribution at different concentrations from these 2D images. In order to obtain a complete visualisation of the dopant distribution in these samples, the 3D nanostructure needs to be determined. This is described in the following section, 4.2.

4.2 Characterisation of 3D Nanostructure

In order to understand the complete component distribution in a material, it is important to extend the nanostructure analysis from 2D to 3D. Therefore, this section is centered around electron tomography 3D reconstructions of the nanoscale distribution of Mo(tfd-$COCF_3$)$_3$ dopants in p($g_4$2T-T). The reconstructions are used to visualise the positions of individual dopant molecules in the material at

different dopant concentrations. Subsequently, the tomography data is evaluated in order to obtain quantitative information regarding the dopant distribution in the samples. Finally, the nanostructure data is correlated to electronic properties at the different dopant concentrations. The text in this section is based on results from the study in paper IV.

4.2.1 Dopant Molecule Visualisation

As described in section 3.2.3, a 3D tomographic reconstruction of an analysed volume can be obtained by acquiring a tilt series of HAADF-STEM 2D projections of a sample volume. Such tilt series were acquired for the doped OSC samples described in section 4.1.4 and used as basis to reconstruct the volumes. The tilt series for all reconstructions used a Saxton scheme and spanned angles between -70° and $+70^{\circ}$ with a 2.5° step at the 0° angle. The SIRT algorithm described in section 3.2.3 was used for the reconstruction and iterated 25 times for each sample in order to minimise background noise. The resulting volumes are shown in figure 4.6. Care was taken to reconstruct volumes at sufficient spatial resolution to resolve the 3D distribution of individual dopant molecules. The voxel side length in the reconstructions is 0.5 nm, while the dopant molecules are approximately 1.2 nm along the long axis and 0.6 nm along the short axis. [49] The red intensity thresholds in figure 4.6 represent the position of the dopant molecules, and the yellow intensity thresholds were set at a slightly lower value. Yellow intensity regions are located around the red intensity regions, and can be interpreted as the small movement of dopant side chains during the tilt series acquisition. The red thresholds were calibrated relative to each other to retain a 5:20:40 ratio between voxels representing dopant molecules for the 5 mol%, 20 mol% and 40 mol% samples. A volume equivalent to an in-plane area of 2 600 μm^2 was reconstructed and analysed for each sample in order to confirm that the reconstructions shown in figure 4.6 were representative of the material.

The reconstructed volumes show a significant difference in 3D nanostructure between the three samples. Dopant molecules are positioned as either isolated individual molecules or as small clusters of molecules. At increased dopant concentration, the size of the clusters increases. Additionally, the distance between clusters decreases with increasing dopant concentration.

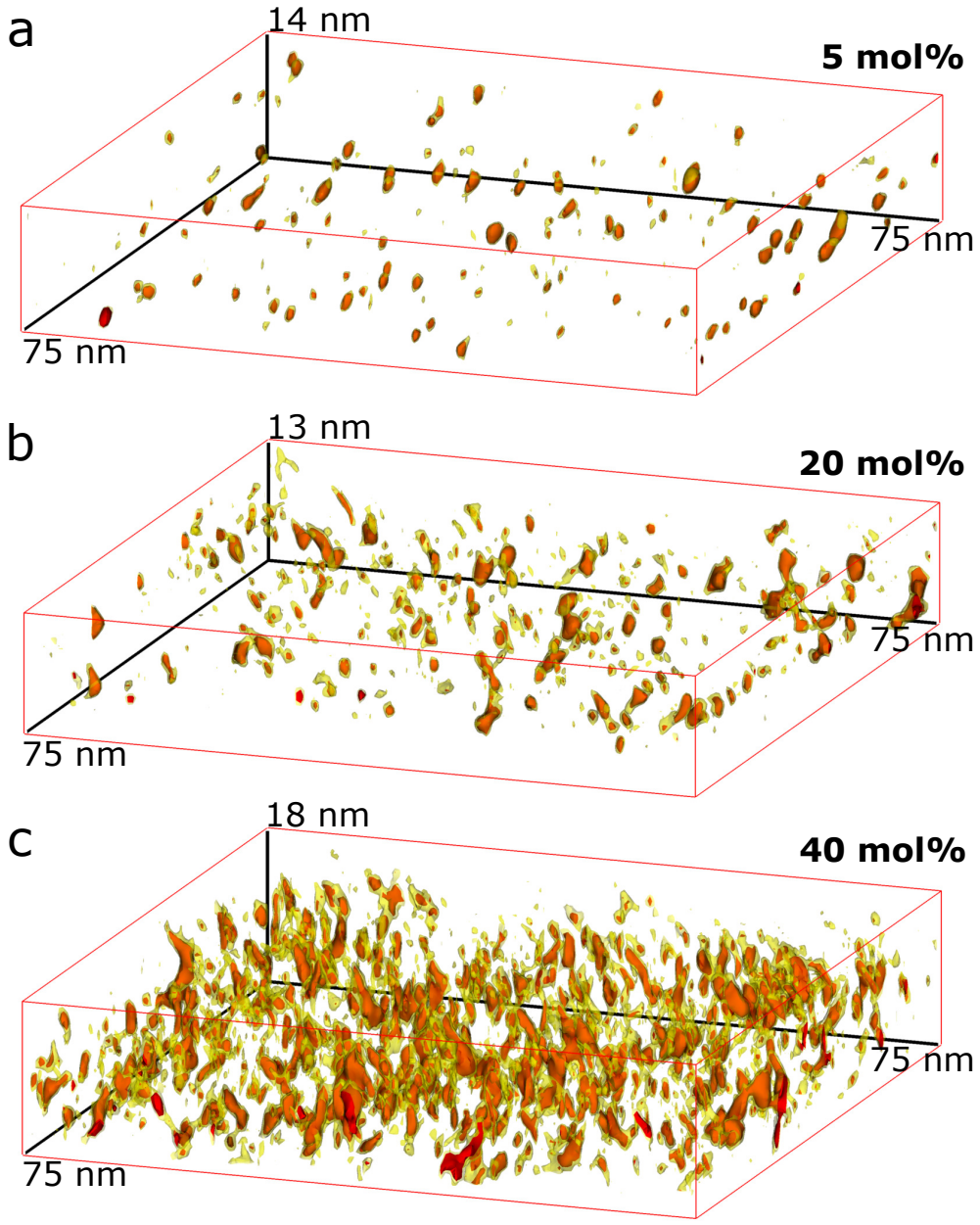

Figure 4.6: Electron tomography reconstructions of the 3D nanostructure of p($g_4$2T-T) doped with a Mo(tfd-$COCF_3$)$_3$ concentration of (a) 5 mol%, (b) 20 mol% and (c) 40 mol%. Red intensity thresholds in the reconstructions represent the position of dopant molecules and yellow intensity thresholds are slightly lower values to visualise the movement of side chains during acquisition.

4.2.2 Tomography Data Evaluation

Figure 4.7 a-c shows representative sub-volumes of the reconstructions in figure 4.6. These figures clearly show the presence of isolated dopant molecules and dopant clusters in the films. The position of each individual dopant molecule in the reconstructed clusters can be indicated through the use of spherical markers with diameters corresponding to the largest dimension of the molecule. The positions of individual dopant molecules in the sub-volumes are marked in figure 4.7 d-f.

The tomography results indicate a trend of increasing dopant cluster size with increasing dopant concentration. Figure 4.7 shows that at 5 mol%, the dopants are mainly present as individual molecules or clusters that are a few molecules in size. The average number of dopant molecules per cluster increases at 20 mol% and 40 mol%. Furthermore, the dopant clusters change shape as the concentration increases, forming elongated chains along the thickness direction of the film.

Repeating the method of manually marking the position of dopant molecules of 50 clusters in each sample, the number of molecules per clusters could be determined. Average values were calculated to be 3.4 for 5 mol%, 4.6 for 20 mol% and 11 for 40 mol%, which quantitatively confirms the visual trends of cluster sizes at different concentrations in figures 4.6 and 4.7. The tomography data was further evaluated by using the software Matlab, which allowed analysis of all clusters in larger reconstructed volumes. Quantitative analysis of a large number of cluster volumes resulted in the size distribution histograms shown in figure 4.8 a. The histograms indicate an especially wide distribution of cluster sizes for the higher dopant concentrations, where a few clusters with volumes as large as 15 nm^3 are observed. Average cluster volumes were calculated to be 1.71 nm^3, 2.96 nm^3 and 3.10 nm^3 for the samples.

Figure 4.8 b shows a histogram of cluster aspect ratio, *i.e.* the ratio between the cluster long axis and short axis, indicating the change in cluster morphology at different dopant concentrations. Examples of dopant cluster conformations for different aspect ratios are included in the figure. Multiple peaks are visible in the histogram, especially for the higher dopant concentrations. A general trend of higher average values and a wider distribution of aspect ratios are observed for higher dopant concentrations. This is consistent with the reconstructed cluster shapes in figures 4.6 and 4.7 that show how the majority of the clusters at 5 mol% has a rounded shape while 20 mol% and 40 mol% display increasingly elongated clusters along the out-of-plane direction of the film.

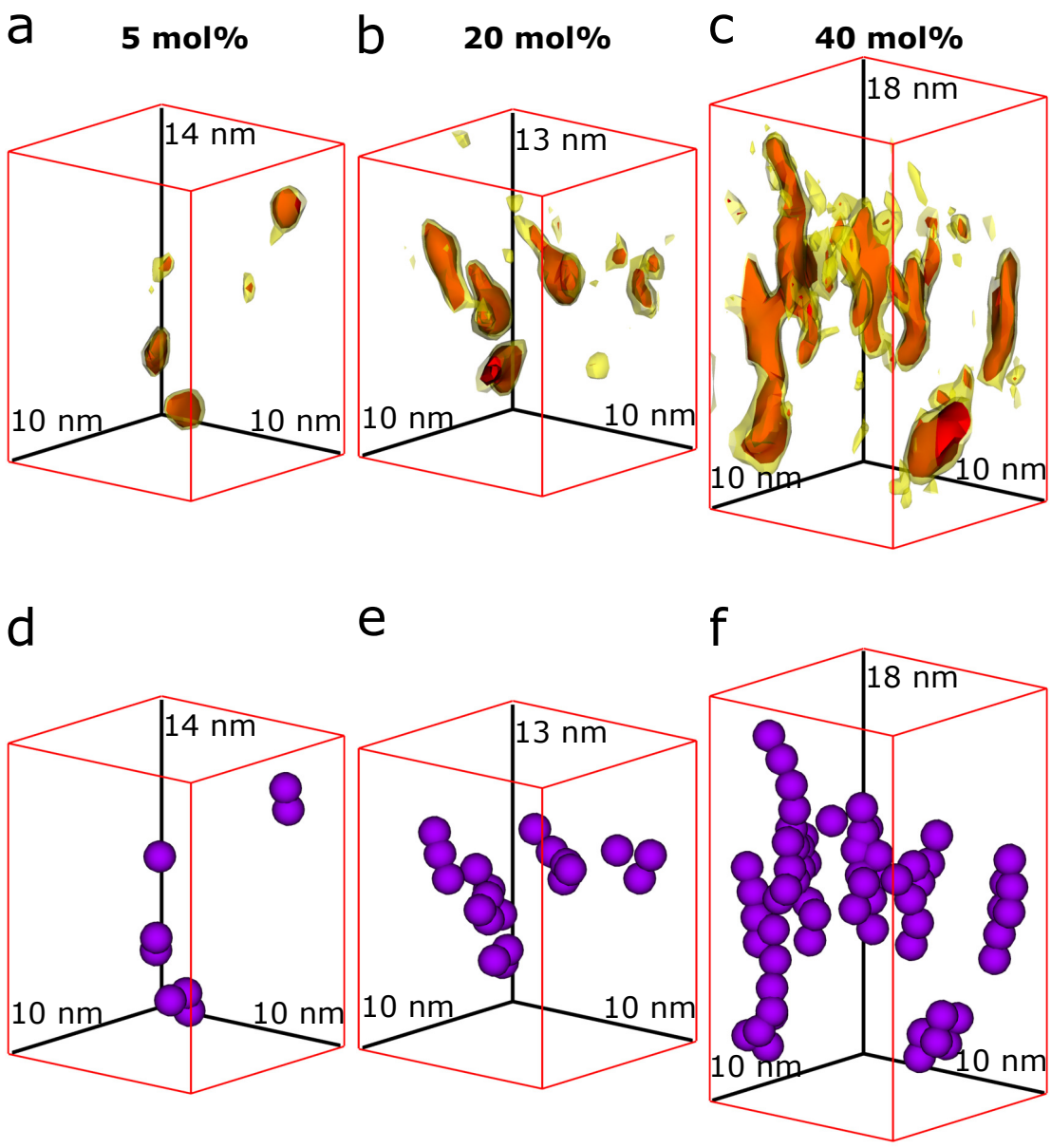

Figure 4.7: Representative sub-volumes of the tomographic reconstructions from figure 4.6. (a)-(c) Reconstructed volumes, showing individual dopant molecules and dopant clusters. Red intensity thresholds in the reconstructions represent the position of dopant molecules. Yellow intensity thresholds are slightly lower values to visualise the movement of side chains during acquisition. (d)-(f) Purple markers that indicate the positions of individual dopants in the clusters.

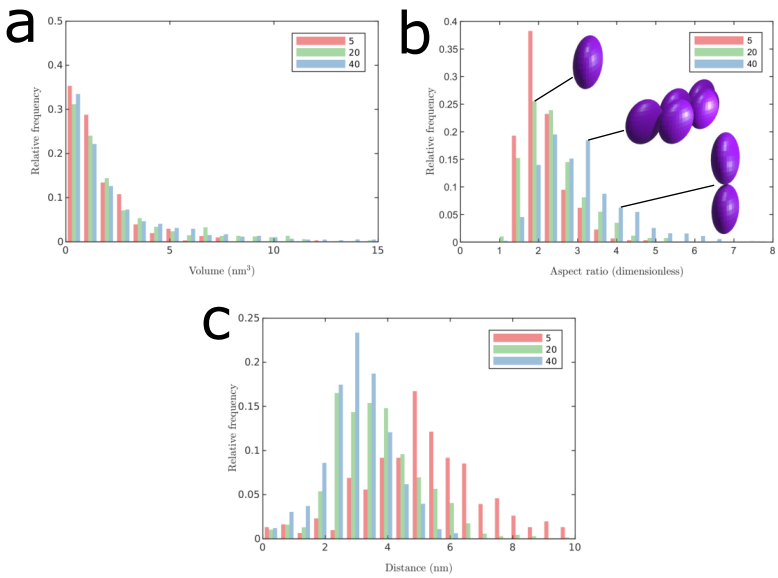

Figure 4.8: Histogram from data analysis on all clusters in a 150 nm by 150 nm in-plane area of each sample, displaying distribution of (a) cluster volumes, (b) cluster elongation ratios and (c) distances to nearest neighbouring clusters.

As a consequence of increasing cluster sizes and changes in cluster morphology, the distance between dopant clusters varied for the different dopant concentrations. Histograms of the distance to the closest neighbouring clusters are shown in figure 4.8 c. Higher average distances and a wider distribution of distances can be seen for the lower dopant concentrations in this figure. Models for prediction of OSC transport properties often assume a homogenous dopant distribution. [103] The wide distributions of cluster distances shown in figure 4.8 c shows a clear heterogenous distribution. Thus, the nanostructure data acquired from the tomography reconstructions may contribute to the simulation accuracy of these films similarly as in the study presented in section 4.1.3.

Although an increased cluster size is observed with increasing dopant concentration, the elongated cluster shapes allows each dopant molecule to be adjacent to the surrounding OSC, as can be seen in figure 4.7. Therefore, the cluster morphology is such that the dopant molecules are not blocked from transferring charges and the ionisation efficiency should be higher compared that of spherical clusters.

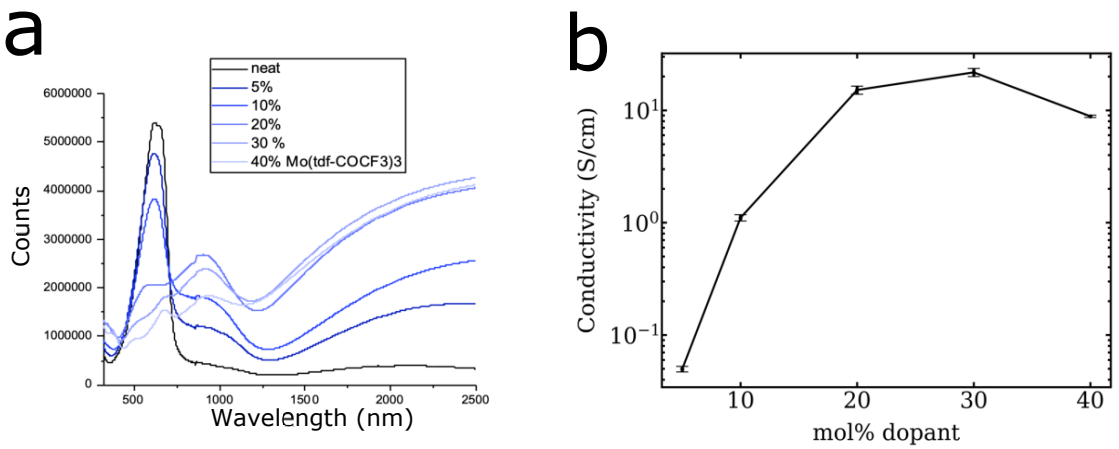

Figure 4.9: Results from electronic analysis of the doped samples through (a) UV-Vis-NIR absorption spectroscopy and (b) four-point probe conductivity measurements.

4.2.3 Nanostructure - Electronic Properties Correlation

The main goal of doping p($g_4$2T-T) using Mo(tfd-$COCF_3$)$_3$ molecules is to introduce charge carriers and enhance electronic properties such as conductivity. Thus, optical and electrical properties were measured for 0 mol%, 5 mol%, 10 mol%, 20 mol%, 30 mol% and 40 mol% thin-film specimens. Results from these measurements are shown in figure 4.9.

Spectra from UV-Vis-NIR absorption spectroscopy, shown in figure 4.9 a, showed absorption from polaronic bands at 900 nm wavelength and in the near infrared for the doped films. The increasingly pronounced polaronic bands at higher dopant concentrations indicate successful charge transfer, [27,31] which is consistent with the conclusions that the dopant molecules are not blocked from charge transfer in the clusters. Results from four-point probe measurements of the electrical conductivity of the thin-film specimen are shown in figure 4.9 b. At concentrations of 5 mol%, an increase in dopant concentration leads to a significant increase of conductivity. This trend is, however, reaching a plateau at approximately 30 mol% and a conductivity decline is observed past this point. Interestingly, this is approximately at the same concentration where changes in cluster size and morphology were observed in the tomography reconstructions. As discussed in section 2.3, such conductivity saturation has been observed in previous studies, and has been attributed to disruptions in nanostructure. [42, 43] However, the tomography reconstructions reveal that there are no large dopant aggregates in the sample, and that each dopant molecule should be sufficiently adjacent to the OSC to undergo

charge transfer.

A recent study has shown that clustering of dopant molecules can directly impact OSC electronic properties. [30] Using modelling, the authors have shown that the charge carrier DOS widens significantly if the number of dopants per cluster is increased from 1 to 6 molecules. In section 2.2, it was discussed that a wider DOS indicates a higher energetic disorder in the system, which in turn may have a notable impact on electrical properties such as conductivity. The dopant clusters observed in the tomography reconstructions may be larger than 6 molecules, as indicated in the data evaluation, and there are also large deviations in dopant sizes. Thus, the energetic disorder is expected to be severe at high concentrations of $Mo(tfd\text{-}COCF_3)_3$ in $p(g_42T\text{-}T)$. Additionally, another recent study suggests that dopant ionisation efficiency may decrease at high dopant concentrations partially or completely due to a low entropy effect. [29] As dopant concentration increases, there will be an increased number of adjacent dopant molecules and a reduced number of OSC host sites favourable for charge transfer. This decreased access to host sites leads to a decreased probability of charge transfer, *i.e.* a reduced dopant ionisation efficiency. It is noteworthy that this explanation to a decreased ionisation efficiency does not require large aggregations where dopants are blocked from the OSC. However, the formation of clusters means that dopants are partially blocked from adjacent OSC host sites, and should lead to further decrease in ionisation efficiency.

The study of dopant distribution presented in this section offers explanations to the decrease in conductivity observed at high concentrations of $Mo(tfd\text{-}COCF_3)_3$ in $p(g_42T\text{-}T)$. The results indicate that dopant clustering even at the single-nanometre scale may cause a significant impact on electronic properties for OSCs. Thus, structural characterisation at this length scale can provide important information for the development of novel doped OSC systems with optimised device-relevant properties.

5 Conclusions and Outlook

In this thesis, electron microscopy was used to study the correlation between nanostructure and electronic properties of different organic semiconductors. The ability of the copolymer p[p($g_4$2T-T)-co-U] to form homogenous films was studied using HAADF-STEM. High-resolution imaging revealed similar structures for the copolymer and for neat p($g_4$2T-T), indicating that the urethane segments in the copolymer were successfully added without significant disruption of the p($g_4$2T-T) nanostructure. This non-disruptive addition enhanced mechanical robustness of the copolymer with only slight reductions of electrical properties from the inclusion of the urethane, which enabled the material to form free-standing films and increased its applicability as active layer in organic electronics.

The bilayer interface structure of the polymers BBL and p($g_4$2T-T) was studied by preparing cross-sections using the FIB-SEM lift-out scheme. Direct HAADF-STEM imaging of the detailed interface structure proved challenging due to the low contrast between the polymers. Instead, they could be distinguished using the spectroscopy technique EDX-SI, which revealed a strong polymer separation and an interface that was only a few nanometres wide. This interface was of high importance for these polymers since it allowed the formation of a continuous charge transport layer with enhanced conductivity through the material. A BHJ of this material blend was created in order to make maximum use of the transport layer, resulting in a bulk material with a conductivity several orders of magnitude higher than that of the pure polymers.

The phase distribution in a BHJ of TQ1:$PC_{71}BM$ was also studied. Structural data regarding the fine-scale separation between the phases was obtained using BF-TEM and HAADF-STEM. This data was used to calibrate a KMC model, resulting in simulated J-V curves that more accurately showed what have been experimentally observed for the system.

Finally, a method was presented for visualising the 3D distribution of individual Mo(tfd-$COCF_3$)$_3$ molecular dopants in p($g_4$2T-T). By acquiring HAADF-STEM tilt series and performing electron tomography, the 3D structure of the material could be reconstructed with sub-nanometre resolution. Analysis of the reconstruc-

tions allowed the positions of individual dopant molecules to be determined. The tomography reconstructions revealed both individual and clusters of dopants. The method was repeated for samples at different dopant concentrations, which showed that the size and shape of the clusters changed as dopant concentration increased. Quantitative data was extracted from the reconstructed volumes, which revealed changes in cluster volumes, aspect ratios and distances to nearest neighbours for the different dopant concentrations. Despite that larger clusters was observed at higher dopant levels, the clusters remained sufficiently fine-dispersed to never fully block dopants from being adjacent to the surrounding polymer. Four-point probe measurements showed that conductivity initially increased with increased dopant concentration and thereafter decreased as the clusters grew larger and increasingly elongated. From the observation of the study, it was suggested that the decreased conductivity at high doping concentrations was a result from an increased energetic disorder that originated from the clustering.

The work in this thesis is focused on nanostructure characterisation of organic semiconductors. Using electron microscopy imaging, spectroscopy and 3D reconstruction, the study provides detailed information that is important for the understanding of fundamental mechanisms in the material systems. As continuation on this work, the electron tomography method presented in this thesis may be repeated on modified versions of Mo(tfd-$COCF_3$)$_3$ in p($g_4$2T-T) in order to investigate how cluster formation changes for different modifications. A systematic study may yield an understanding of how different dopant molecules cluster, which can be used in order to optimise the 3D dopant distribution and hence the electronic properties of the organic semiconductor. Another aspect that may be studied is the detailed dopant drift for Mo(tfd-$COCF_3$)$_3$ in p($g_4$2T-T) as a function of an applied electric field. Since the high Z-contrast allows direct imaging of individual dopants using HAADF-STEM, this may be used to follow the path of the molecules after *in situ* applying an electrical bias across the polymer film. A detailed study of the dopant dynamics should provide new information regarding the movement of the molecules during device operation and how it can be controlled, which in turn can lead to novel strategies for an increased long-term stability of organic electronics.

Bibliography

[1] Daniel Todd. *The world electronics industry*. Routledge, 2018.

[2] Stephen Maldonado. The importance of new "sand-to-silicon"processes for the rapid future increase of photovoltaics. *ACS Energy Letters*, 5(11):3628–3632, 11 2020.

[3] P. R. Berger and M. Kim. Polymer solar cells: P3ht:pcbm and beyond. *Journal of Renewable and Sustainable Energy*, 10(1):013508, 2018.

[4] Alexandra F. Paterson, Saumya Singh, Kealan J. Fallon, Thomas Hodsden, Yang Han, Bob C. Schroeder, Hugo Bronstein, Martin Heeney, Iain McCulloch, and Thomas D. Anthopoulos. Recent progress in high-mobility organic transistors: A reality check. *Advanced Materials*, 30(36):1801079, 2018.

[5] Dion Khodagholy, Thomas Doublet, Pascale Quilichini, Moshe Gurfinkel, Pierre Leleux, Antoine Ghestem, Esma Ismailova, Thierry Hervé, Sébastien Sanaur, Christophe Bernard, and George G. Malliaras. In vivo recordings of brain activity using organic transistors. *Nature Communications*, 4(1):1575, 2013.

[6] B. Lüssem, M. Riede, and K. Leo. Doping of organic semiconductors. *physica status solidi (a)*, 210(1):9–43, 2013.

[7] Ian E. Jacobs and Adam J. Moulé. Controlling molecular doping in organic semiconductors. *Advanced Materials*, 29(42):1703063, 2017.

[8] Duc T. Duong, Chenchen Wang, Erin Antono, Michael F. Toney, and Alberto Salleo. The chemical and structural origin of efficient p-type doping in p3ht. *Organic Electronics*, 14(5):1330–1336, 2013.

[9] Justin E. Cochran, Matthias J. N. Junk, A. M. Glaudell, P. Levi Miller, John S. Cowart, Michael F. Toney, Craig J. Hawker, Bradley F. Chmelka, and Michael L. Chabinyc. Molecular interactions and ordering in electrically doped polymers: Blends of pbttt and f4tcnq. *Macromolecules*, 47(19):6836–6846, 10 2014.

[10] Feng Liu, Wei Zhao, John R. Tumbleston, Cheng Wang, Yu Gu, Dong Wang, Alejandro L. Briseno, Harald Ade, and Thomas P. Russell. Understanding the morphology of ptb7:pcbm blends in organic photovoltaics. *Advanced Energy Materials*, 4(5):1301377, 2014.

[11] John D. Roehling, Derya Baran, Joseph Sit, Thaer Kassar, Tayebeh Ameri, Tobias Unruh, Christoph J. Brabec, and Adam J. Moulé. Nanoscale morphology of ptb7 based organic photovoltaics as a function of fullerene size. *Scientific Reports*, 6(1):30915, 2016.

[12] Brooke Kuei, Melissa P. Aplan, Joshua H. Litofsky, and Enrique D. Gomez. New opportunities in transmission electron microscopy of polymers. *Materials Science and Engineering: R: Reports*, 139:100516, 2020.

[13] Dinesh Lolla, Joseph Gorse, Christian Kisielowski, Jiayuan Miao, Philip L. Taylor, George G. Chase, and Darrell H. Reneker. Polyvinylidene fluoride molecules in nanofibers, imaged at atomic scale by aberration corrected electron microscopy. *Nanoscale*, 8:120–128, 2016.

[14] Christopher J. Takacs, Neil D. Treat, Stephan Krämer, Zhihua Chen, Antonio Facchetti, Michael L. Chabinyc, and Alan J. Heeger. Remarkable order of a high-performance polymer. *Nano Letters*, 13(6):2522–2527, 06 2013.

[15] Changhe Guo, Frances I. Allen, Youngmin Lee, Thinh P. Le, Chengyu Song, Jim Ciston, Andrew M. Minor, and Enrique D. Gomez. Probing local electronic transitions in organic semiconductors through energy-loss spectrum imaging in the transmission electron microscope. *Advanced Functional Materials*, 25(38):6071–6076, 2015.

[16] Ryo Ishikawa, Eiji Okunishi, Hidetaka Sawada, Yukihito Kondo, Fumio Hosokawa, and Eiji Abe. Direct imaging of hydrogen-atom columns in a crystal by annular bright-field electron microscopy. *Nature Materials*, 10(4):278–281, 2011.

[17] Scott D. Findlay, Tomohiro Saito, Naoya Shibata, Yukio Sato, Junko Matsuda, Kohta Asano, Etsuo Akiba, Tsukasa Hirayama, and Yuichi Ikuhara. Direct imaging of hydrogen within a crystalline environment. *Applied Physics Express*, 3(11):116603, nov 2010.

[18] D.B. Williams and C.B. Carter. *Transmission Electron Microscopy: A Textbook for Materials Science*. Springer Science+Business Media, 2 edition, 2009.

[19] R.F. Egerton. Radiation damage to organic and inorganic specimens in the tem. *Micron*, 119:72–87, 2019.

[20] Dario Natali. 1 - fundamentals of organic electronic devices. In Piero Cosseddu and Mario Caironi, editors, *Organic Flexible Electronics*, Woodhead Publishing Series in Electronic and Optical Materials, chapter 1, pages 1–25. Woodhead Publishing, 2021.

[21] Robert M. Pankow and Barry C. Thompson. The development of conjugated polymers as the cornerstone of organic electronics. *Polymer*, 207:122874, 2020.

[22] Hideki Shirakawa, Edwin J. Louis, Alan G. MacDiarmid, Chwan K. Chiang, and Alan J. Heeger. Synthesis of electrically conducting organic polymers: halogen derivatives of polyacetylene, (ch). *J. Chem. Soc., Chem. Commun.*, pages 578–580, 1977.

[23] Hugo Bronstein, Christian B. Nielsen, Bob C. Schroeder, and Iain McCulloch. The role of chemical design in the performance of organic semiconductors. *Nature Reviews Chemistry*, 4(2):66–77, 2020.

[24] Veaceslav Coropceanu, Jérôme Cornil, Demetrio A. da Silva Filho, Yoann Olivier, Robert Silbey, and Jean-Luc Brédas. Charge transport in organic semiconductors. *Chemical Reviews*, 107(4):926–952, 04 2007.

[25] Hannes Hase and Ingo Salzmann. 11 - doping in organic semiconductors. In Oksana Ostroverkhova, editor, *Handbook of Organic Materials for Electronic and Photonic Devices (Second Edition)*, Woodhead Publishing Series in Electronic and Optical Materials, pages 349–383. Woodhead Publishing, second edition edition, 2019.

[26] Ingo Salzmann, Georg Heimel, Martin Oehzelt, Stefanie Winkler, and Norbert Koch. Molecular electrical doping of organic semiconductors: Fundamental mechanisms and emerging dopant design rules. *Accounts of Chemical Research*, 49(3):370–378, 03 2016.

[27] Henry Méndez, Georg Heimel, Stefanie Winkler, Johannes Frisch, Andreas Opitz, Katrein Sauer, Berthold Wegner, Martin Oehzelt, Christian Röthel, Steffen Duhm, Daniel Többens, Norbert Koch, and Ingo Salzmann. Charge-transfer crystallites as molecular electrical dopants. *Nature Communications*, 6(1):8560, 2015.

[28] Ingo Salzmann and Georg Heimel. Toward a comprehensive understanding of molecular doping organic semiconductors (review). *Journal of Electron Spectroscopy and Related Phenomena*, 204:208–222, 2015. Organic Electronics.

[29] Artem Fediai, Anne Emering, Franz Symalla, and Wolfgang Wenzel.

Disorder-driven doping activation in organic semiconductors. *Phys. Chem. Chem. Phys.*, 22:10256–10264, 2020.

[30] Connor J. Boyle, Meenakshi Upadhyaya, Peijian Wang, Lawrence A. Renna, Michael Lu-Díaz, Seung Pyo Jeong, Nicholas Hight-Huf, Ljiljana Korugic-Karasz, Michael D. Barnes, Zlatan Aksamija, and D. Venkataraman. Tuning charge transport dynamics via clustering of doping in organic semiconductor thin films. *Nature Communications*, 10(1):2827, 2019.

[31] Jean Luc Bredas and G Bryan Street. Polarons, bipolarons, and solitons in conducting polymers. *Accounts of Chemical Research*, 18(10):309–315, 1985.

[32] Samuele Giannini, Antoine Carof, Matthew Ellis, Hui Yang, Orestis George Ziogos, Soumya Ghosh, and Jochen Blumberger. Quantum localization and delocalization of charge carriers in organic semiconducting crystals. *Nature Communications*, 10(1):3843, 2019.

[33] Alberto Salleo, R. Joseph Kline, Dean M. DeLongchamp, and Michael L. Chabinyc. Microstructural characterization and charge transport in thin films of conjugated polymers. *Advanced Materials*, 22(34):3812–3838, 2010.

[34] Rodrigo Noriega, Jonathan Rivnay, Koen Vandewal, Felix P. V. Koch, Natalie Stingelin, Paul Smith, Michael F. Toney, and Alberto Salleo. A general relationship between disorder, aggregation and charge transport in conjugated polymers. *Nature Materials*, 12(11):1038–1044, 2013.

[35] RA Street, JE Northrup, and A Salleo. Transport in polycrystalline polymer thin-film transistors. *Physical Review B*, 71(16):165202, 2005.

[36] Jonna Hynynen, Emmy Järsvall, Renee Kroon, Yadong Zhang, Stephen Barlow, Seth R. Marder, Martijn Kemerink, Anja Lund, and Christian Müller. Enhanced thermoelectric power factor of tensile drawn poly(3-hexylthiophene). *ACS Macro Letters*, 8(1):70–76, 2019.

[37] Justin E. Cochran, Matthias J. N. Junk, A. M. Glaudell, P. Levi Miller, John S. Cowart, Michael F. Toney, Craig J. Hawker, Bradley F. Chmelka, and Michael L. Chabinyc. Molecular interactions and ordering in electrically doped polymers: Blends of pbttt and f4tcnq. *Macromolecules*, 47(19):6836–6846, 10 2014.

[38] Vishnu Vijayakumar, Elena Zaborova, Laure Biniek, Huiyan Zeng, Laurent Herrmann, Alain Carvalho, Olivier Boyron, Nicolas Leclerc, and Martin Brinkmann. Effect of alkyl side chain length on doping kinetics, thermopower, and charge transport properties in highly oriented f4tcnq-doped pbttt films. *ACS Applied Materials & Interfaces*, 11(5):4942–4953, 02 2019.

[39] Amer Hamidi-Sakr, Laure Biniek, Jean-Louis Bantignies, David Maurin, Laurent Herrmann, Nicolas Leclerc, Patrick Lévêque, Vishnu Vijayakumar, Nicolas Zimmermann, and Martin Brinkmann. A versatile method to fabricate highly in-plane aligned conducting polymer films with anisotropic charge transport and thermoelectric properties: The key role of alkyl side chain layers on the doping mechanism. *Advanced Functional Materials*, 27(25):1700173, 2017.

[40] Renee Kroon, David Kiefer, Dominik Stegerer, Liyang Yu, Michael Sommer, and Christian Müller. Polar side chains enhance processability, electrical conductivity, and thermal stability of a molecularly p-doped polythiophene. *Advanced Materials*, 29(24):1700930, 2017.

[41] Hans Kleemann, Christoph Schuenemann, Alexander A. Zakhidov, Moritz Riede, Björn Lüssem, and Karl Leo. Structural phase transition in pentacene caused by molecular doping and its effect on charge carrier mobility. *Organic Electronics*, 13(1):58–65, 2012.

[42] Felix Deschler, Daniel Riedel, Andras Deák, Bernhard Ecker, Elizabeth von Hauff, and Enrico Da Como. Imaging of morphological changes and phase segregation in doped polymeric semiconductors. *Synthetic Metals*, 199:381–387, 2015.

[43] Julie Euvrard, Amélie Revaux, Pierre-Alain Bayle, Michel Bardet, Dominique Vuillaume, and Antoine Kahn. The formation of polymer-dopant aggregates as a possible origin of limited doping efficiency at high dopant concentration. *Organic Electronics*, 53:135–140, 2018.

[44] Daniela Donhauser, Martin Pfannmöller, Levin Dieterle, Katrin Schultheiß, Rasmus R. Schröder, Wolfgang Kowalsky, and Michael Kröger. Observation of filamentous nanostructures in organic-inorganic composite thin films deposited by co-evaporation. *Advanced Functional Materials*, 23(17):2130–2136, 2013.

[45] Ian E Jacobs, Erik W Aasen, Julia L Oliveira, Tayane N Fonseca, John D Roehling, Jun Li, Gwangwu Zhang, Matthew P Augustine, Mark Mascal, and Adam J Moulé. Comparison of solution-mixed and sequentially processed p3ht: F4tcnq films: effect of doping-induced aggregation on film morphology. *Journal of Materials Chemistry C*, 4(16):3454–3466, 2016.

[46] Jonna Hynynen, David Kiefer, Liyang Yu, Renee Kroon, Rahim Munir, Aram Amassian, Martijn Kemerink, and Christian Müller. Enhanced electrical conductivity of molecularly p-doped poly(3-hexylthiophene) through

understanding the correlation with solid-state order. *Macromolecules*, 50(20):8140–8148, 2017. PMID: 29093606.

[47] Jun Li, Correy Koshnick, Souleymane O. Diallo, Sophia Ackling, David M. Huang, Ian E. Jacobs, Thomas F. Harrelson, Kunlun Hong, Guangwu Zhang, Joseph Beckett, Mark Mascal, and Adam J. Moulé. Quantitative measurements of the temperature-dependent microscopic and macroscopic dynamics of a molecular dopant in a conjugated polymer. *Macromolecules*, 50(14):5476–5489, 07 2017.

[48] Sergio A. Paniagua, Jose Baltazar, Hossein Sojoudi, Swagat K. Mohapatra, Siyuan Zhang, Clifford L. Henderson, Samuel Graham, Stephen Barlow, and Seth R. Marder. Production of heavily n- and p-doped cvd graphene with solution-processed redox-active metal–organic species. *Mater. Horiz.*, 1:111–115, 2014.

[49] Swagat K. Mohapatra, Yadong Zhang, Bhupinder Sandhu, Marina S. Fonari, Tatiana V. Timofeeva, Seth R. Marder, and Stephen Barlow. Synthesis, characterization, and crystal structures of molybdenum complexes of unsymmetrical electron-poor dithiolene ligands. *Polyhedron*, 116:88–95, 2016. Special Issue in Honour of Professor Malcolm L. H. Green on the occasion of his 80th Birthday.

[50] Nichole C. Cates, Roman Gysel, Zach Beiley, Chad E. Miller, Michael F. Toney, Martin Heeney, Iain McCulloch, and Michael D. McGehee. Tuning the properties of polymer bulk heterojunction solar cells by adjusting fullerene size to control intercalation. *Nano Letters*, 9(12):4153–4157, 12 2009.

[51] Patrick Reiser, Lars Müller, Vipilan Sivanesan, Robert Lovrincic, Stephen Barlow, Seth R. Marder, Annemarie Pucci, Wolfram Jaegermann, Eric Mankel, and Sebastian Beck. Dopant diffusion in sequentially doped poly(3-hexylthiophene) studied by infrared and photoelectron spectroscopy. *The Journal of Physical Chemistry C*, 122(26):14518–14527, 07 2018.

[52] Lars Müller, Seon-Young Rhim, Vipilan Sivanesan, Dongxiang Wang, Sebastian Hietzschold, Patrick Reiser, Eric Mankel, Sebastian Beck, Stephen Barlow, Seth R. Marder, Annemarie Pucci, Wolfgang Kowalsky, and Robert Lovrincic. Electric-field-controlled dopant distribution in organic semiconductors. *Advanced Materials*, 29(30):1701466, 2017.

[53] David Kiefer, Renee Kroon, Anna I. Hofmann, Hengda Sun, Xianjie Liu, Alexander Giovannitti, Dominik Stegerer, Alexander Cano, Jonna Hynynen, Liyang Yu, Yadong Zhang, Dingqi Nai, Thomas F. Harrelson, Michael Som-

mer, Adam J. Moulé, Martijn Kemerink, Seth R. Marder, Iain McCulloch, Mats Fahlman, Simone Fabiano, and Christian Müller. Double doping of conjugated polymers with monomer molecular dopants. *Nature Materials*, 18(2):149–155, 2019.

[54] Wolfgang Tress. *Organic Solar Cells*, chapter 1, pages 1–9. Springer International Publishing, Cham, 2014.

[55] National Renewable Energy Laboratory. Best research-cell efficiency chart, Jun 2021.

[56] Andrea Feltrin and Alex Freundlich. Material considerations for terawatt level deployment of photovoltaics. *Renewable Energy*, 33(2):180–185, 2008. E-MRS 2006 Symposium M: Materials, Devices and Prospects for Sustainable Energy.

[57] Gordon J. Hedley, Arvydas Ruseckas, and Ifor D. W. Samuel. Light harvesting for organic photovoltaics. *Chemical Reviews*, 117(2):796–837, 01 2017.

[58] Luyao Lu, Tianyue Zheng, Qinghe Wu, Alexander M. Schneider, Donglin Zhao, and Luping Yu. Recent advances in bulk heterojunction polymer solar cells. *Chemical Reviews*, 115(23):12666–12731, 12 2015.

[59] William R. Mateker and Michael D. McGehee. Progress in understanding degradation mechanisms and improving stability in organic photovoltaics. *Advanced Materials*, 29(10):1603940, 2017.

[60] Derya Baran, Raja Shahid Ashraf, David A. Hanifi, Maged Abdelsamie, Nicola Gasparini, Jason A. Röhr, Sarah Holliday, Andrew Wadsworth, Sarah Lockett, Marios Neophytou, Christopher J. M. Emmott, Jenny Nelson, Christoph J. Brabec, Aram Amassian, Alberto Salleo, Thomas Kirchartz, James R. Durrant, and Iain McCulloch. Reducing the efficiency–stability–cost gap of organic photovoltaics with highly efficient and stable small molecule acceptor ternary solar cells. *Nature Materials*, 16(3):363–369, 2017.

[61] Mikkel Jørgensen, Kion Norrman, and Frederik C. Krebs. Stability/degradation of polymer solar cells. *Solar Energy Materials and Solar Cells*, 92(7):686–714, 2008. Degradation and Stability of Polymer and Organic Solar Cells.

[62] Suren A. Gevorgyan, Morten V. Madsen, Bérenger Roth, Michael Corazza, Markus Hösel, Roar R. Søndergaard, Mikkel Jørgensen, and Frederik C. Krebs. Lifetime of organic photovoltaics: Status and predictions. *Advanced Energy Materials*, 6(2):1501208, 2016.

[63] Chao Li, Jiadong Zhou, Jiali Song, Jinqiu Xu, Huotian Zhang, Xuning Zhang, Jing Guo, Lei Zhu, Donghui Wei, Guangchao Han, Jie Min, Yuan Zhang, Zengqi Xie, Yuanping Yi, He Yan, Feng Gao, Feng Liu, and Yanming Sun. Non-fullerene acceptors with branched side chains and improved molecular packing to exceed 18% efficiency in organic solar cells. *Nature Energy*, 2021.

[64] Guangchao Han, Yuanping Yi, and Zhigang Shuai. From molecular packing structures to electronic processes: Theoretical simulations for organic solar cells. *Advanced Energy Materials*, 8(28):1702743, 2018.

[65] Xiao Zhang and Li-Dong Zhao. Thermoelectric materials: Energy conversion between heat and electricity. *Journal of Materiomics*, 1(2):92–105, 2015.

[66] Binghao Wang and Antonio Facchetti. Mechanically flexible conductors for stretchable and wearable e-skin and e-textile devices. *Advanced Materials*, 31(28):1901408, 2019.

[67] Daniel Champier. Thermoelectric generators: A review of applications. *Energy Conversion and Management*, 140:167–181, 2017.

[68] Boris Russ, Anne Glaudell, Jeffrey J. Urban, Michael L. Chabinyc, and Rachel A. Segalman. Organic thermoelectric materials for energy harvesting and temperature control. *Nature Reviews Materials*, 1(10):16050, 2016.

[69] Guangming Chen, Wei Xu, and Daoben Zhu. Recent advances in organic polymer thermoelectric composites. *J. Mater. Chem. C*, 5:4350–4360, 2017.

[70] Renee Kroon, Desalegn Alemu Mengistie, David Kiefer, Jonna Hynynen, Jason D. Ryan, Liyang Yu, and Christian Müller. Thermoelectric plastics: from design to synthesis, processing and structure–property relationships. *Chem. Soc. Rev.*, 45:6147–6164, 2016.

[71] Shrayesh N. Patel, Anne M. Glaudell, Kelly A. Peterson, Elayne M. Thomas, Kathryn A. O'Hara, Eunhee Lim, and Michael L. Chabinyc. Morphology controls the thermoelectric power factor of a doped semiconducting polymer. *Science Advances*, 3(6), 2017.

[72] Takao Someya, Zhenan Bao, and George G. Malliaras. The rise of plastic bioelectronics. *Nature*, 540(7633):379–385, 2016.

[73] Hongyan Yao, Zeng Fan, Hanlin Cheng, Xin Guan, Chen Wang, Kuan Sun, and Jianyong Ouyang. Recent development of thermoelectric polymers and composites. *Macromolecular Rapid Communications*, 39(6):1700727, 2018.

[74] Mats R. Andersson, Olinga Thomas, Wendimagegn Mammo, Mattias Svensson, Mathias Theander, and Olle Inganäs. Substituted polythiophenes designed for optoelectronic devices and conductors. *J. Mater. Chem.*, 9:1933–1940, 1999.

[75] Artem Fediai, Anne Emering, Franz Symalla, and Wolfgang Wenzel. Disorder-driven doping activation in organic semiconductors. *Phys. Chem. Chem. Phys.*, 22:10256–10264, 2020.

[76] A. Bafekry, M. M. Fadlallah, C. Nguyen, and D. Gogova. Vertical two-dimensional layered conjugated porous organic network structures of polybenzimidazobenzophenanthroline (bbl): A first-principles study. *Applied Physics Letters*, 117(23):233101, 2020.

[77] Jongbok Lee, Alexander J. Kalin, Tianyu Yuan, Mohammed Al-Hashimi, and Lei Fang. Fully conjugated ladder polymers. *Chem. Sci.*, 8:2503–2521, 2017.

[78] Camilla Lindqvist, Anke Sanz-Velasco, Ergang Wang, Olof Bäcke, Stefan Gustafsson, Eva Olsson, Mats R. Andersson, and Christian Müller. Nucleation-limited fullerene crystallisation in a polymer–fullerene bulk-heterojunction blend. *J. Mater. Chem. A*, 1:7174–7180, 2013.

[79] Lintao Hou, Ergang Wang, Jonas Bergqvist, B. Viktor Andersson, Zhongqiang Wang, Christian Müller, Mariano Campoy-Quiles, Mats R. Andersson, Fengling Zhang, and Olle Inganäs. Lateral phase separation gradients in spin-coated thin films of high-performance polymer:fullerene photovoltaic blends. *Advanced Functional Materials*, 21(16):3169–3175, 2011.

[80] Darren J. Lipomi and Zhenan Bao. Stretchable and ultraflexible organic electronics. *MRS Bulletin*, 42(2):93–97, 2017.

[81] Shiv K. Gupta, Purushottam Jha, Ajay Singh, Mohamed M. Chehimi, and Dinesh K. Aswal. Flexible organic semiconductor thin films. *J. Mater. Chem. C*, 3:8468–8479, 2015.

[82] G.H. Michler. *Electron Microscopy of Polymers*. Springer Laboratory. Springer Berlin Heidelberg, 2008.

[83] J.I. Goldstein, D.E. Newbury, J.R. Michael, N.W.M. Ritchie, J.H.J. Scott, and D.C. Joy. Scanning electron microscopy and x-ray microanalysis. Springer New York, 4 edition, 2017.

[84] L. Reimer. *Transmission Electron Microscopy: Physics of Image Formation and Microanalysis*, volume 36. Springer Berlin Heidelberg, 2013.

[85] S.J. Pennycook and P.D. Nellist. *Scanning Transmission Electron Microscopy: Imaging and Analysis*. Springer New York, 2011.

[86] R. F Egerton. Electron energy-loss spectroscopy in the electron microscope. Springer Science & Business Media, 3 edition, 2011.

[87] Paul A. Midgley and Rafal E. Dunin-Borkowski. Electron tomography and holography in materials science. *Nature Materials*, 8(4):271–280, 2009.

[88] Richard Anthony Crowther, D. J. DeRosier, and Aaron Klug. The reconstruction of a three-dimensional structure from projections and its application to electron microscopy. *Proceedings of the Royal Society of London. A. Mathematical and Physical Sciences*, 317(1530):319–340, 1970.

[89] Peter Ercius, Osama Alaidi, Matthew J. Rames, and Gang Ren. Electron tomography: A three-dimensional analytic tool for hard and soft materials research. *Advanced Materials*, 27(38):5638–5663, 2015.

[90] Daisuke Shindo and Tetsuo Oikawa. *Energy Dispersive X-ray Spectroscopy*, pages 81–102. Springer Japan, Tokyo, 2002.

[91] G. Cliff and G. W. Lorimer. The quantitative analysis of thin specimens. *Journal of Microscopy*, 103(2):203–207, 1975.

[92] M. Watanabe and D. B. Williams. The quantitative analysis of thin specimens: a review of progress from the cliff-lorimer to the new ζ-factor methods. *Journal of Microscopy*, 221(2):89–109, 2006.

[93] A. J. D'Alfonso, B. Freitag, D. Klenov, and L. J. Allen. Atomic-resolution chemical mapping using energy-dispersive x-ray spectroscopy. *Phys. Rev. B*, 81:100101, Mar 2010.

[94] Z. Chen, M. Weyland, X. Sang, W. Xu, J.H. Dycus, J.M. LeBeau, A.J. D'Alfonso, L.J. Allen, and S.D. Findlay. Quantitative atomic resolution elemental mapping via absolute-scale energy dispersive x-ray spectroscopy. *Ultramicroscopy*, 168:7–16, 2016.

[95] R.F. Egerton, R. McLeod, F. Wang, and M. Malac. Basic questions related to electron-induced sputtering in the tem. *Ultramicroscopy*, 110(8):991–997, 2010. PROCEEDINGS OF THE INTERNATIONAL WORKSHOP ON ENHANCED DATA GENERATED BY ELECTRONS.

[96] Qiaoli Chen, Christian Dwyer, Guan Sheng, Chongzhi Zhu, Xiaonian Li, Changlin Zheng, and Yihan Zhu. Imaging beam-sensitive materials by electron microscopy. *Advanced Materials*, 32(16):1907619, 2020.

[97] Yangjin Lee, Sol Lee, Jun-Yeong Yoon, Jinwoo Cheon, Hu Young Jeong, and Kwanpyo Kim. Fabrication and imaging of monolayer phosphorene with preferred edge configurations via graphene-assisted layer-by-layer thinning. *Nano Letters*, 20(1):559–566, 01 2020.

[98] Brooke Kuei and Enrique D. Gomez. Elucidating mechanisms for electron beam damage in conjugated polymers. *Microscopy and Microanalysis*, 24(S1):1988–1989, 2018.

[99] Olof Bäcke, Camilla Lindqvist, Amaia Diaz de Zerio Mendaza, Stefan Gustafsson, Ergang Wang, Mats R. Andersson, Christian Müller, and Eva Olsson. Mapping fullerene crystallization in a photovoltaic blend: an electron tomography study. *Nanoscale*, 7:8451–8456, 2015.

[100] Shabi Thankaraj Salammal, Eduard Mikayelyan, Souren Grigorian, Ullrich Pietsch, Nils Koenen, Ullrich Scherf, Navaphun Kayunkid, and Martin Brinkmann. Impact of thermal annealing on the semicrystalline nanomorphology of spin-coated thin films of regioregular poly(3-alkylthiophene)s as observed by high-resolution transmission electron microscopy and grazing incidence x-ray diffraction. *Macromolecules*, 45(13):5575–5585, 07 2012.

[101] J. Ayache, L. Beaunier, J. Boumendil, G. Ehret, and D. Laub. *Sample Preparation Handbook for Transmission Electron Microscopy: Techniques*. Sample preparation handbook for transmission electron microscopy / Jeanne Ayache; Luc Beaunier; Jacqueline Boumendil; Gabrielle Ehret; Danièle Laub. Foreword by Ron Anderson. Springer New York, 2010.

[102] Michael Corazza, Søren B. Simonsen, Helmut Gnaegi, Karl T.S. Thydén, Frederik C. Krebs, and Suren A. Gevorgyan. Comparison of ultramicrotomy and focused-ion-beam for the preparation of tem and stem cross section of organic solar cells. *Applied Surface Science*, 389:462–468, 2016.

[103] Hassan Abdalla, Guangzheng Zuo, and Martijn Kemerink. Range and energetics of charge hopping in organic semiconductors. *Phys. Rev. B*, 96:241202, Dec 2017.

Paper I

Toughening of a Soft Polar Polythiophene through Copolymerization with Hard Urethane Segments

Sepideh Zokaei, Renee Kroon, Johannes Gladisch, Bryan D. Paulsen, Wonil Sohn, Anna I. Hofmann, Gustav Persson, Arne Stamm, Per-Olof Syrén, Eva Olsson, Jonathan Rivnay, Eleni Stavrinidou, Anja Lund, and Christian Müller

Advanced Science, 2021, 8, 2002778

ADVANCED SCIENCE
Open Access
www.advancedscience.com

Toughening of a Soft Polar Polythiophene through Copolymerization with Hard Urethane Segments

*Sepideh Zokaei, Renee Kroon, Johannes Gladisch, Bryan D. Paulsen, Wonil Sohn, Anna I. Hofmann, Gustav Persson, Arne Stamm, Per-Olof Syrén, Eva Olsson, Jonathan Rivnay, Eleni Stavrinidou, Anja Lund, and Christian Müller**

Polar polythiophenes with oligoethylene glycol side chains are exceedingly soft materials. A low glass transition temperature and low degree of crystallinity prevents their use as a bulk material. The synthesis of a copolymer comprising 1) soft polythiophene blocks with tetraethylene glycol side chains, and 2) hard urethane segments is reported. The molecular design is contrary to that of other semiconductor-insulator copolymers, which typically combine a soft nonconjugated spacer with hard conjugated segments. Copolymerization of polar polythiophenes and urethane segments results in a ductile material that can be used as a free-standing solid. The copolymer displays a storage modulus of 25 MPa at room temperature, elongation at break of 95%, and a reduced degree of swelling due to hydrogen bonding. Both chemical doping and electrochemical oxidation reveal that the introduction of urethane segments does not unduly reduce the hole charge-carrier mobility and ability to take up charge. Further, stable operation is observed when the copolymer is used as the active layer of organic electrochemical transistors.

1. Introduction

Conjugated polymers that are able to deform without fracture are highly sought after for the realization of truly flexible electronic devices.[1–5] A polymer will only be able to accommodate a high degree of strain if its glass transition temperature T_g lies well below the operating temperature of the target application. At the same time, the material should behave like a solid and not a viscous substance, which requires reinforcement, for instance through crystallites or other types of physical or chemical crosslinks.

The rigid backbone of conjugated polymers, which often comprises planar aromatic moieties, typically results in a high T_g and a strong tendency for aggregation.[6,7] As a result, many materials are brittle at room temperature and display a high tensile storage modulus E' of up to several GPa.[8] Synthetic efforts therefore concentrate on strategies that reduce E', such as 1) copolymerization with a nonconjugated polymer, such as poly(methyl acrylate) or a polyurethane,[9–11] 2) the incorporation of nonconjugated spacer units, such as hydrogen-bonding motifs,[12,13] and flexible linkages,[14–20] and 3) an increase in the length and grafting density of the solubilizing side chains.[21,22]

S. Zokaei, Dr. R. Kroon, Dr. A. I. Hofmann, Dr. A. Lund, Prof. C. Müller
Department of Chemistry and Chemical Engineering
Chalmers University of Technology
Göteborg 41296, Sweden
E-mail: zokaei@chalmers.se; christian.muller@chalmers.se

J. Gladisch, E. Stavrinidou
Laboratory of Organic Electronics
Department of Science and Technology
Linköping University
Norrköping 60174, Sweden

J. Gladisch, E. Stavrinidou
Wallenberg Wood Science Center
Department of Science and Technology
Linköping University
Norrköping 60174, Sweden

Dr. B. D. Paulsen, W. Sohn, J. Rivnay
Department of Biomedical Engineering
Northwestern University
Evanston, IL 60208, USA

G. Persson, Prof. E. Olsson
Department of Physics
Chalmers University of Technology
Göteborg 41296, Sweden

A. Stamm, P.-O. Syrén
Department of Fibre and Polymer Technology
KTH Royal Institute of Technology
Stockholm 11428, Sweden

P.-O. Syrén
Wallenberg Wood Science Center
KTH Royal Institute of Technology
Stockholm 11428, Sweden

Prof. E. Olsson, Prof. C. Müller
Wallenberg Wood Science Center
Chalmers University of Technology
Göteborg 41296, Sweden

The ORCID identification number(s) for the author(s) of this article can be found under https://doi.org/10.1002/advs.202002778

DOI: 10.1002/advs.202002778

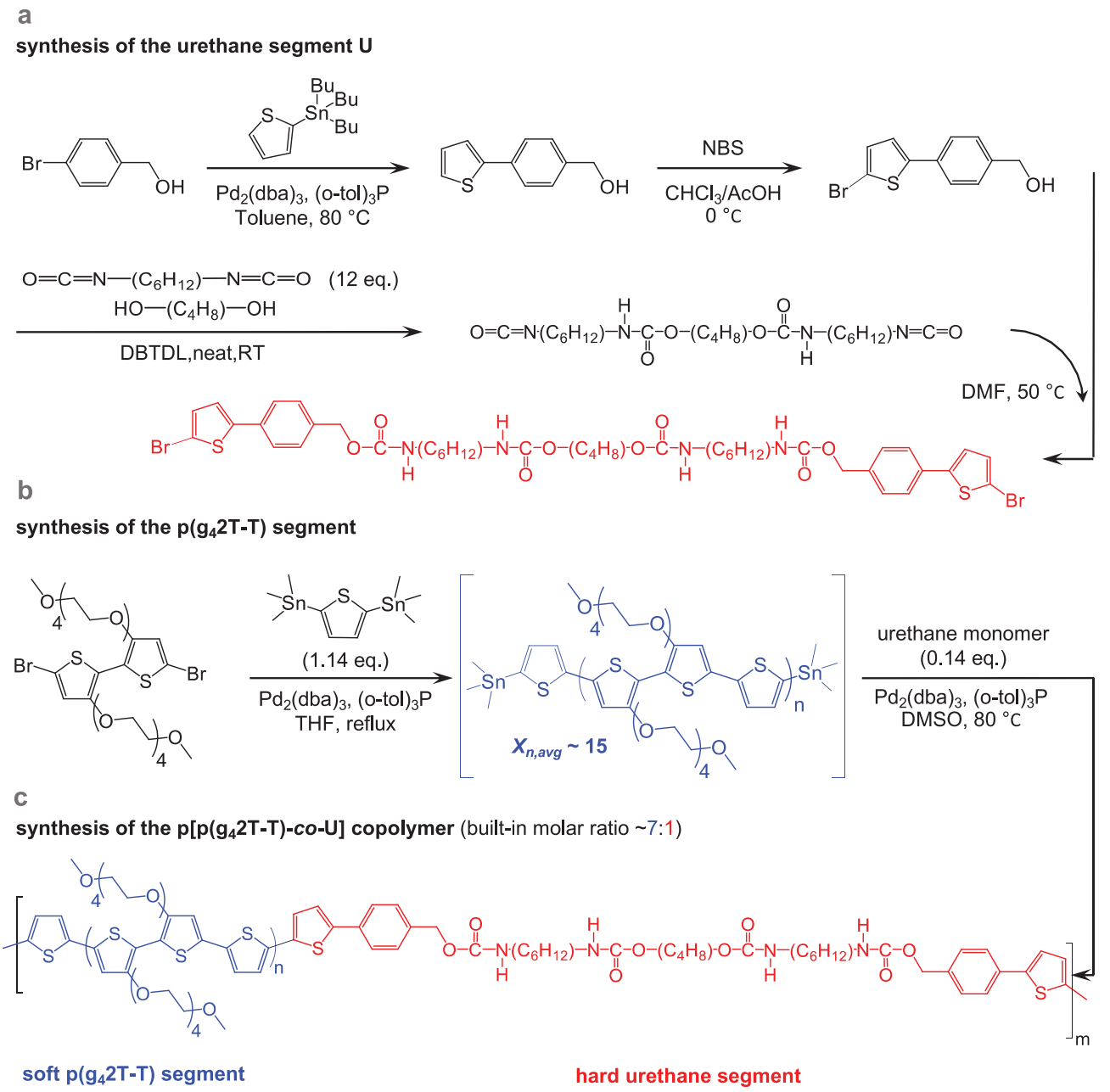

Figure 1. Synthesis scheme of a) the urethane segment (U), b) the p($g_4$2T-T) segment, and c) the copolymer p[p($g_4$2T-T)-*co*-U].

The majority of conjugated polymers feature alkyl side chains, and an increase in their length is an effective way to lower the T_g. Regio-random poly(3-alkylthiophene)s (P3AT)s, for instance, show a significant drop in T_g from +45 to −18 °C when increasing the alkyl side chain length from butyl to dodecyl,[23] accompanied by a significant reduction in the shear storage modulus G' at room temperature from 1 GPa to about 100 kPa.[24] The decrease in storage modulus is less pronounced in case of regioregular P3ATs because the presence of crystallites reinforces the material above the T_g, resulting in a much higher $E' \approx 100$ MPa at room temperature in case of poly(3-dodecylthiophene) (P3DDT) with dodecyl side chains.[21,22]

A different design strategy is required for conjugated polymers with oligoethylene glycol side chains, which currently receive widespread interest for applications related to bioelectronics,[25–28] as well as energy storage,[29–31] and harvesting.[32–36] These materials are considerably softer than comparable polymers with alkyl side chains. This behavior is exemplified by the polymer p($g_4$2T-T) (see **Figure 1** for chemical structure), which already softens at −45 °C (see discussion below) and displays a low tendency for aggregation.[37]

While the use of oligoethylene glycol side chains is an effective tool for the design of polymers with a low T_g, the resulting material is too soft for applications, such as electronic textiles

(e-textiles) and thermoelectrics where mechanically robust and free-standing structures are needed.[38,39] Therefore, it would be desirable to develop means to improve its mechanical robustness without unduly compromising its ability to transport and store electronic charges, facilitated by the conjugated backbone, as well as ions, the affinity for which is greatly enhanced by polar side chains.

The most widely used synthetic strategy to improve the ductility or elasticity of an initially rigid conjugated polymer involves the incorporation of a nonconjugated flexible spacer unit.[14–18] We here invert this design principle and use a soft conjugated segment, i.e., p($g_4$2T-T), which we combine with a hard linker unit. We chose to incorporate a urethane-based block, which allows the formation of a reversible network mediated by hydrogen bonds. The resulting copolymer p[p($g_4$2T-T)-*co*-U] (see Figure 1 for chemical structure) features a molar ratio of 7:1 of soft $g_4$2T-T to hard urethane segments. Incorporation of the urethane segments turns the putty-like p($g_4$2T-T) into a free-standing solid with E' ≈25 MPa. Incorporation of the hard urethane blocks only slightly reduces the electrical and electrochemical properties, yielding a material with a mobility of 0.2–0.7 $cm^2\ V^{-1}\ s^{-1}$ when chemically doped or electrochemically oxidized, and a conductivity of about 20 S cm^{-1} when doped with 2,3,5,6-tetrafluoro-7,7,8,8-tetracyanoquinodimethane (F4TCNQ).

2. Results and Discussion

2.1. Synthesis of the p[p($g_4$2T-T)-*co*-U] Copolymer

The most widely used synthetic route to obtain segmented urethanes follows the reaction of an alcohol-functionalized prepolymer with a diisocyanate and (subsequently) a diol or diamine chain extender.[40,41] Extending the same synthetic route to conjugated polymers seemed less reliable to us, as the typical synthesis scale (0.1–1 g) and large difference in molecular weight of the dihydroxyl-functionalized conjugated macromonomer and the diisocyanate/chain extenders would prevent accurate control over the stoichiometry. To obtain a more robust synthetic procedure, we decided to first synthesize a high molecular-weight monomer that incorporated the desired urethane bonds, allowing for a controlled one-pot reaction with the conjugated soft block.

The reinforcing urethane monomer (Figure 1a) was obtained by first synthesizing (4-(5-bromothiophen-2-yl)phenyl)methanol as the capping moiety. Then, 1,4-butanediol (BDO) was reacted with a 12-fold excess of 1,6-hexamethylene diisocyanate (HDI). After removal of excess HDI, the resulting HDI–BDO–HDI trimer was reacted with the bromothiophene-functionalized benzyl alcohol to yield the reinforcing urethane monomer. The final monomer was moderately soluble in hot pyridine or hot dimethyl sulfoxide (DMSO).

To obtain the p[p($g_4$2T-T)-*co*-U] copolymer, we first synthesized a p($g_4$2T-T) prepolymer (Figure 1b) by reacting a ≈1.14 stoichiometric excess of 2,5-bis(trimethylstannyl)thiophene with the dibrominated $g_4$2T-monomer under Stille conditions, which according to Carothers' equation yields an average degree of polymerization of about $\bar{X}_n$ ≈15 in the limit of complete conversion, which corresponds to twice the average number of repeat units, i.e., 7 $g_4$2T-T + one thiophene ring and a concomitant M_n ≈ 4690 g mol^{-1}. After reacting for 3 h, the stoichiometric imbalance was restored to a 1:1 stoichiometry by addition of 0.14 eq. of the urethane comonomer to the distannylated p($g_4$2T-T) prepolymer. To ensure solubility of the final p[p($g_4$2T-T)-*co*-U] copolymer during the chain-extension, a solvent exchange was performed by addition of DMSO, while tetrahydrofuran (THF) was slowly removed through nitrogen purging and increasing the reaction temperature to 80 °C. The polymerization was continued for 48 h, after which the crude polymer was collected by precipitation. After purification, the Soxhlet extraction offered two fractions of p[p($g_4$2T-T)-*co*-U]. A lower molecular weight fraction was obtained by dichloromethane (DCM) extraction, while a higher molecular weight fraction with a number-average molecular weight of M_n ≈13.5 kg mol^{-1} (PDI ≈2.5, Figure S1, Supporting Information) was extracted with DMSO as a blue material, which is used in this study. From this value, and the weight of the built-in urethane moiety (≈805 g mol^{-1}), we can calculate that on average 3–6 reinforcing units are built into a polymer chain. ^{1}H-NMR indicated a ≈7:1 built-in molar ratio of the $g_4$2T-T repeat unit and the urethane block (Figures 1c; and Figure S2, Supporting Information), i.e., a 6:1 weight ratio of $g_4$2T-T and the urethane block.

p($g_4$2T-T) readily dissolves in chloroform (CH_3Cl). Instead, the copolymer can be processed from 80 °C hot polar solvents, such as pyridine, DMSO and dimethylformamide. We used UV–vis spectroscopy to assess the stability of p[p($g_4$2T-T)-*co*-U] dissolved in pyridine and DMSO. A blueshift of the polymer absorption occurs already after 1 day (Figure S3, Supporting Information), which indicates that solutions of the copolymer must be used immediately to avoid degradation. The homopolymer also displays limited stability in polar solvents (Figure S3, Supporting Information), as reported previously.[37] Unlike solutions, thin films of both the homopolymer and copolymer, processed from pyridine, are stable for at least 3 months, as evidenced by the absence of any significant shift of the polymer absorption (Figure S4, Supporting Information). We however note that the polymer films become slightly oxidized when stored at ambient conditions, which we infer from the emergence of clear polaronic absorption peaks in the NIR part of the UV-Vis-NIR absorbance spectrum.

2.2. Hydrogen Bonding and Nanostructure of the Copolymer

In a first set of experiments, we studied how temperature impacts the formation of urethane "hard" domains in p[p($g_4$2T-T)-*co*-U]. Transmission Fourier-transform infrared (FTIR) spectroscopy allowed us to distinguish between free and hydrogen-bonded urethane (**Figure 2**a). Hydrogen bonding, depending on its strength, shifts the stretching vibration of NH and C=O groups of urethane bonds to lower energies.[40] Chittibabu et al. studied a polythiophene with urethane containing side chains and assigned absorbance peaks at 1725 and 1705 cm^{-1} to the stretching vibration of free and hydrogen-bonded C=O groups, respectively.[42] p[p($g_4$2T-T)-*co*-U] processed from DMSO features a pronounced peak at 1683 cm^{-1}, which we assign to hydrogen-bonded urethane segments, and a weaker shoulder around 1718 cm^{-1}, which indicates free, i.e., not hydrogen-bonded urethane segments. Heating to 220 °C results in the disappearance of the peak at 1683 cm^{-1} and a shift of the C=O stretching vibration to 1726 cm^{-1}, which we explain with dissociation of hydrogen bonds. Upon

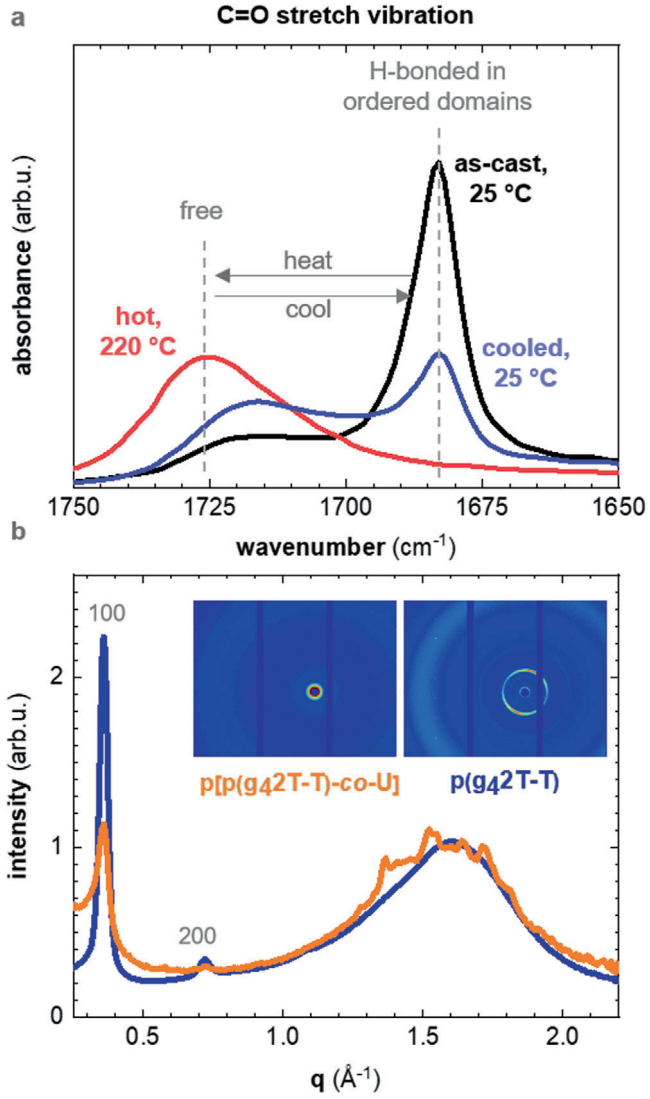

Figure 2. a) FTIR absorbance of the carbonyl stretch vibration in the urethane linkage, recorded at 25 °C for a p[p($g_4$2T-T)-*co*-U] film cast from dimethyl sulfoxide (DMSO) (black), recorded for the same film at 220 °C (red) and after cooling from 220 to 25 °C (blue). b) WAXS diffractograms of a piece of p($g_4$2T-T) (orange) and a free-standing film of p[p($g_4$2T-T)-*co*-U] (blue) normalized to the intensity of the amorphous halo at 1.6 Å^{-1}.

subsequent cooling to room temperature the two C=O peaks at 1683 and 1718 cm^{-1} do not regain their initial intensity, which implies that the hydrogen bonded network only partially recovers. For the N–H stretch vibration (3324 cm^{-1}), which we assign to the N–H stretch vibration of hydrogen-bonded N–H groups, we observe a similar behavior (Figure S5, Supporting Information). This peak diminishes upon heating while a new peak at 3434 cm^{-1} emerges, indicating dissociation of hydrogen bonds. The peak at 3324 cm^{-1} only returns to some extent upon subsequent cooling to room temperature, which again confirms that hydrogen-bonds only partially recover.

We carried out wide-angle X-ray scattering (WAXS) to compare the relative degree of crystalline order of p($g_4$2T-T) and the p[p($g_4$2T-T)-*co*-U] copolymer (Figure 2b). The WAXS diffractogram of neat p($g_4$2T-T) features prominent peaks at q_{100} ≈0.36 Å^{-1} and q_{200} ≈ 0.71 Å^{-1}, which we assign to lamellar stacking. We note that a distinct π–π stacking peak is absent, in agreement with previous reports.[37,43] Instead, a broad amorphous halo with a peak maximum at q ≈1.6 Å^{-1} is present. For the copolymer the intensity of the lamellar stacking peaks q_{n00}, assigned to the p($g_4$2T-T) blocks, is noticeably reduced. We argue that the presence of the urethane blocks reduces the ability of the conjugated segment to order due to formation of the hydrogen-bonded network. Further, the WAXS diffractogram of the copolymer features weak but distinct peaks on top of the broad amorphous halo. We rule out that some of these peaks arise from π–π stacking of p($g_4$2T-T), which should result in a peak around 1.8 nm^{-1} (cf. refs. [37,43]). Instead, we tentatively assign these additional peaks to the presence of ordered urethane domains. The length of a fully extended urethane block in our copolymer is about 5 nm, and therefore ordered domains are likely only a few nanometers in size. We attempted to resolve the nanostructure of neat p($g_4$2T-T) as well as the copolymer with high-resolution scanning transmission electron microscopy (HR-STEM) but did not observe distinct domains (Figure S6, Supporting Information). A possible explanation for this is that the domains are evenly distributed in three dimensions and cannot be distinguished in projection from a sample where multiple blocks are overlapping. Both materials display the same granular texture, which may form as a result of the micellar-like structure that we have previously inferred for solutions of neat p($g_4$2T-T).[37]

2.3. Thermomechanical Properties of the Copolymer and Comparison with p($g_4$2T-T)

Since p($g_4$2T-T) is very soft, we were unable to study the thermomechanical properties of free-standing samples of the reference material. We instead used a technique recently applied to conjugated polymers by Sharma et al.,[44] which utilizes a thin layer of the polymer supported by a glass fiber mesh and allows to record the relative change in tensile storage and loss modulus E' and E'' upon heating. A dynamic mechanical analysis (DMA) thermogram of fiber mesh reinforced p($g_4$2T-T) indicates considerable softening already at low temperatures with a peak in E'' at −45 °C and a shoulder around −20 °C (Figure S7, Supporting Information). For the copolymer we observe two peaks in E'' at −44 and −20 °C. While these measurements clearly indicate that both materials start to soften at very low temperatures, we are currently unable to conclusively assign either observed transition to the T_g. We have used the empirical relation proposed by Xie et al.,[24] which allows to estimate the T_g of a conjugated polymer by considering the mobility of each atom that make up its repeat unit, and obtain a value of T_g = −15 °C (cf. Supporting Information).

We were readily able to prepare micrometer-thick, free-standing samples from the copolymer by peeling off drop-cast films from a glass substrate. The copolymer is considerably stronger compared to neat p($g_4$2T-T), as evidenced by a knot tied into a ribbon cut from a drop-cast copolymer film (**Figure 3**a). We studied the thermomechanical properties of the copolymer both with tensile testing and DMA. The tensile storage modulus of the copolymer has a value of E ≈25 MPa at room temperature (value from single measurement shown in Figure 3a). A strain at break

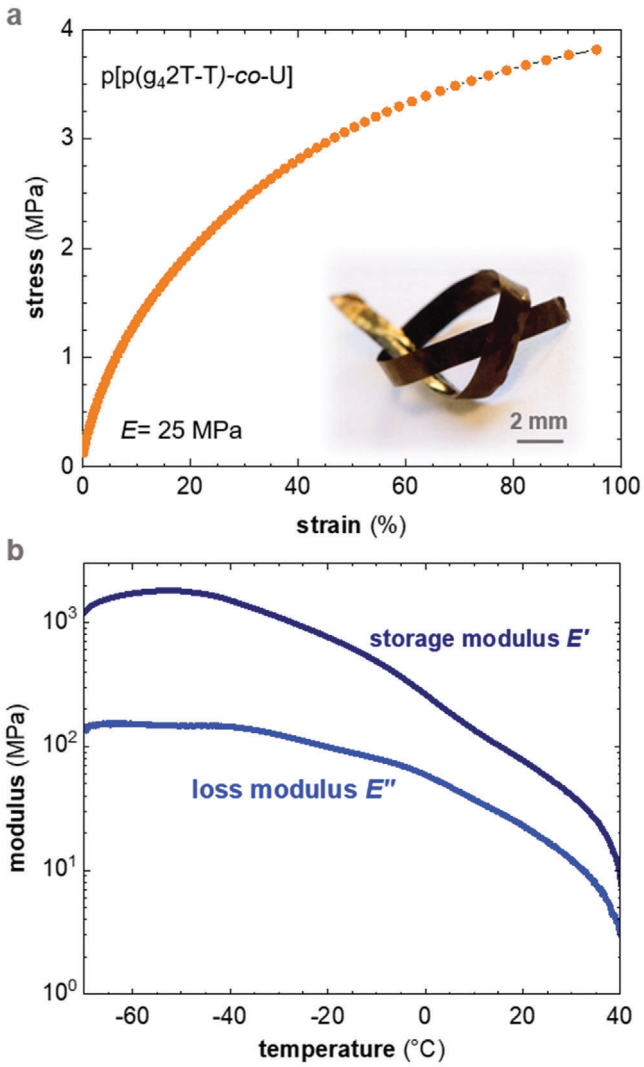

Figure 3. a) Tensile stress–strain curve of a free-standing p[p($g_4$2T-T)-*co*-U] film (inset: photograph of a knotted p[p($g_4$2T-T)-*co*-U] ribbon). b) Storage and loss modulus, E' and E'', of free-standing p[p($g_4$2T-T)-*co*-U] measured with DMA from −70 to 40 °C.

of ϵ_{break} ≈95% indicates that the copolymer is able to undergo significant plastic deformation. DMA measured in tensile mode revealed that E' drops from 1.2 GPa at −70 °C to 7 MPa at 40 °C (Figure 3b).

2.4. Electrochemical Swelling

We used swelling experiments to confirm the presence of a reinforcing network in the p[p($g_4$2T-T)-*co*-U] copolymer. Recent studies have shown that polythiophenes with oligoethylene glycol side chains undergo considerable active swelling exceeding 100% during electrochemical oxidation.[28,45] Our setup consisted of a carbon filament working electrode coated with a ≈2 µm thick layer of the homopolymer or the copolymer, which was submerged in an aqueous KCl electrolyte solution together with a Pt counter electrode and an Ag/AgCl reference electrode (cf. Experimental Section for details). Application of a positive potential of up to +0.8 V versus Ag/AgCl resulted in oxidation of the polymer layer, accompanied by ingression of Cl^- counterions that are surrounded by a water hydration shell, which leads to a sizable volume increase. We monitored the degree of swelling as a function of oxidation/reduction cycle by applying a potential of ±0.8 V versus Ag/AgCl. Very little passive swelling, less than 1%, is observed for both polymers (Figure S8, Supporting Information). For neat p($g_4$2T-T) a relative volume change of ΔV ≈100% (i.e., the volume change upon swelling with respect to the previous minimum contracted state) increased to ΔV ≈125% during the 5th electrochemical cycle. Instead, the ability of the p[p($g_4$2T-T)-*co*-U] copolymer to expand is lower with only ΔV ≈38% during the 1st electrochemical cycle and ΔV ≈33% during the 5th cycle (**Figure 4**). Both polymers exhibit an irreversible volume change, i.e., they do not return to the initial state when electrochemically reduced. The irreversible change tends to stabilize at the 5th cycle for p($g_4$2T-T), while the copolymer stabilizes already at the 3rd cycle. Such a behavior has been observed before for similar materials like p(g_3T2)[45] as well as for hydrogels, where it has been described as a conditioning effect due to nonrecoverable changes in the polymer network.[46] We argue that the presence of urethane domains allows the copolymer to resist extensive swelling and renders the polymer matrix more stable, which is in agreement with the presence of a reinforcing network that we inferred from our thermomechanical analysis.

2.5. Electrochemical Oxidation and Spectroelectrochemistry

We were interested in comparing the extent to which p($g_4$2T-T) and the p[p($g_4$2T-T)-*co*-U] copolymer can be electrochemically oxidized. Our electrochemical cell contained a polymer film spin-cast on an indium tin oxide (ITO)/glass working electrode, a Pt wire counter electrode and an Ag wire pseudoreference electrode, submerged in an electrolyte solution of 0.1 M 1-ethyl-3-methylimidazolium tetrafluoroborate ([EMIM][BF_4]) in acetonitrile (AcN; cf. Experimental Section for details). Cyclic voltammograms of the homopolymer and the copolymer indicate an oxidation onset of E_{ox} ≈ −0.44 V and −0.41 V versus Ferrocene/Ferrocenium (Fc/Fc^+) (**Table 1** and **Figure 5**a), which correspond to an ionization energy IE = 5.1 eV + E_{ox} ≈ 4.66 V and 4.69 eV, respectively.

We then recorded a series of UV–vis–NIR absorbance spectra at different constant oxidation potentials between −0.33 V and +0.37 V versus Fc/Fc^+ and plotted the change in absorbance relative to the spectrum of the undoped polymer at −0.53 V (Figure 5b). The neutral p($g_4$2T-T) absorption with its peak at 600 nm diminishes with increasing potential due to gradual oxidation of the conjugated backbone. At +0.37 V the change in absorbance ΔA at 600 nm has reached a close to constant value, indicating that both polymers are strongly oxidized. We conclude that the urethane segments do not noticeably impact the ability of the copolymer to take up charge. At higher wavelengths two polaronic absorption bands emerge, one with its peak at 900 nm and one in the infrared region. The absorbance at 900 nm increases up to an oxidation potential of 0.07 V, but decreases again at higher potentials, which we explain with the increasing presence of bipolarons (Figure 5c; and Figure S9, Supporting Information). We argue that at low oxidation potentials the majority of

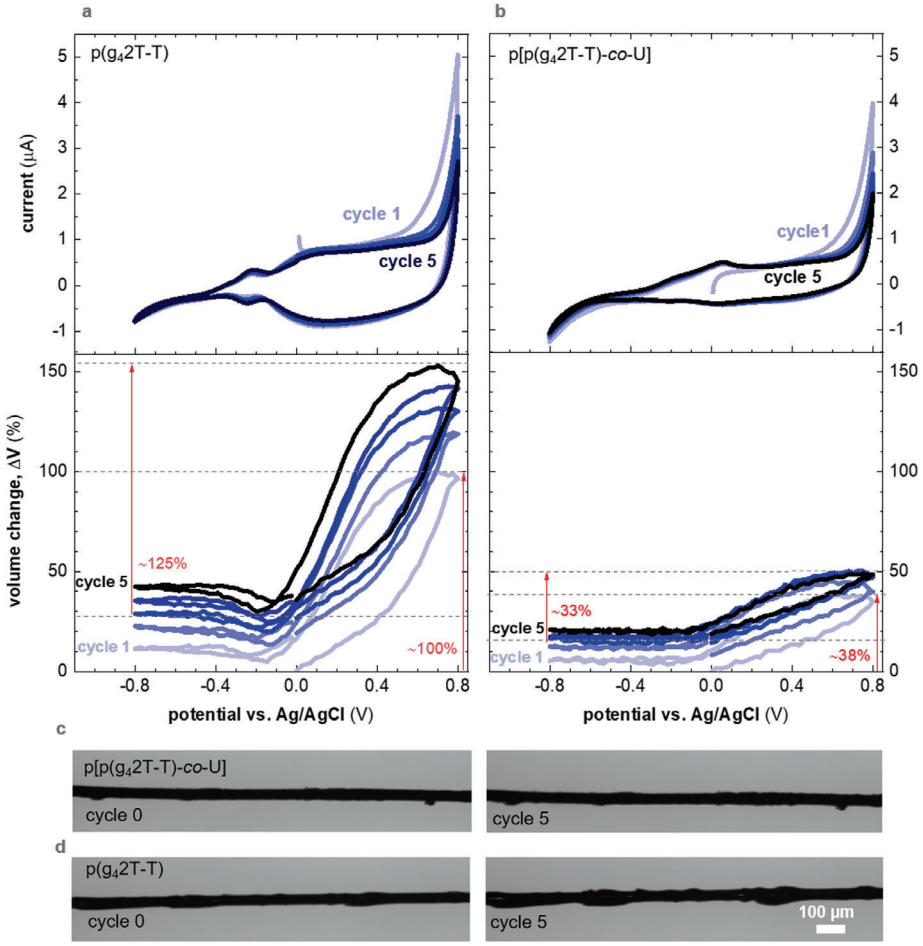

Figure 4. Cyclic voltammograms (top) and volume change of the polymer coating $\Delta V = (V_{pol} - V^0_{pol})/V^0_{pol}$, where V_{pol} is the volume of the coating at different potentials and V^0_{pol} is the initial volume of the coating (bottom), recorded during oxidation/reduction cycle 1–5 of a carbon filament coated with ~2 μm of a) p($g_4$2T-T) and b) p[p($g_4$2T-T)-*co*-U] in 0.01 M KCl electrolyte; c,d) optical micrographs of the coated carbon filaments prior to the first cycle and after cycle 5.

Table 1. Summary of electrochemical oxidation and chemical doping experiments: degree of active swelling ΔV ($n = 1$), conductivity σ when sequentially doped with F4TCNQ ($n = 3$), charge-carrier density N_v estimated from UV–vis–NIR absorbance spectra of F4TCNQ doped thin films ($n = 1$), and corresponding charge-carrier mobility μ; number of measured samples, n, indicated in brackets.

	p($g_4$2T-T)	p[p($g_4$2T-T)-*co*-U]
ΔV [%]	125	33
σ [S cm^{-1}]	48 ± 8	20 ± 5
N_v [m^{-3}]	2.4 × 10^{26}	1.7 × 10^{26}
μ [cm^2 V^{-1} s^{-1}]	1.2 ± 0.2	0.7 ± 0.2

hole charges are polarons, and that bipolarons increasingly form at higher oxidation levels.

2.6. Chemical Doping with F4TCNQ

Both p($g_4$2T-T) and p[p($g_4$2T-T)-*co*-U] could be readily doped with F4TCNQ. Sequential doping by drop-coating ≈60 nm thin polymer films with solutions of F4TCNQ in AcN resulted in an electrical conductivity of $\sigma \approx (20 \pm 5)$ S cm^{-1} and (48 ± 8) S cm^{-1} for p[p($g_4$2T-T)-*co*-U] and p($g_4$2T-T), respectively. The conductivity of the doped homopolymer and copolymer gradually decreased over the course of 7 days accompanied by a decrease in the polaronic absorption peaks in the NIR (Figure S11, Supporting Information).

We recorded UV–vis–NIR absorbance spectra of F4TCNQ-doped thin films. In case of both polymers the neat p($g_4$2T-T) absorption peak at 600 nm disappears, while two polaronic absorbance bands emerge around 900 nm and in the infrared, respectively (**Figure 6**). We estimated the F4TCNQ anion concentration through comparison of the UV–vis–NIR absorbance spectra of the F4TCNQ-doped polymers with those of neat F4TCNQ and the F4TCNQ anion (Figure 6; and Figure S10, Supporting Information), as described previously.[37] We estimate a concentration of about 10^{26} anions per m^{-3} for both materials (Table 1). The F4TCNQ anion concentration is equal to the number of generated hole polarons and hence corresponds to the charge-carrier density N_v, including both bound and mobile charges. We estimate the charge-carrier mobility μ according to $\sigma = N_v \cdot \mu \cdot e$

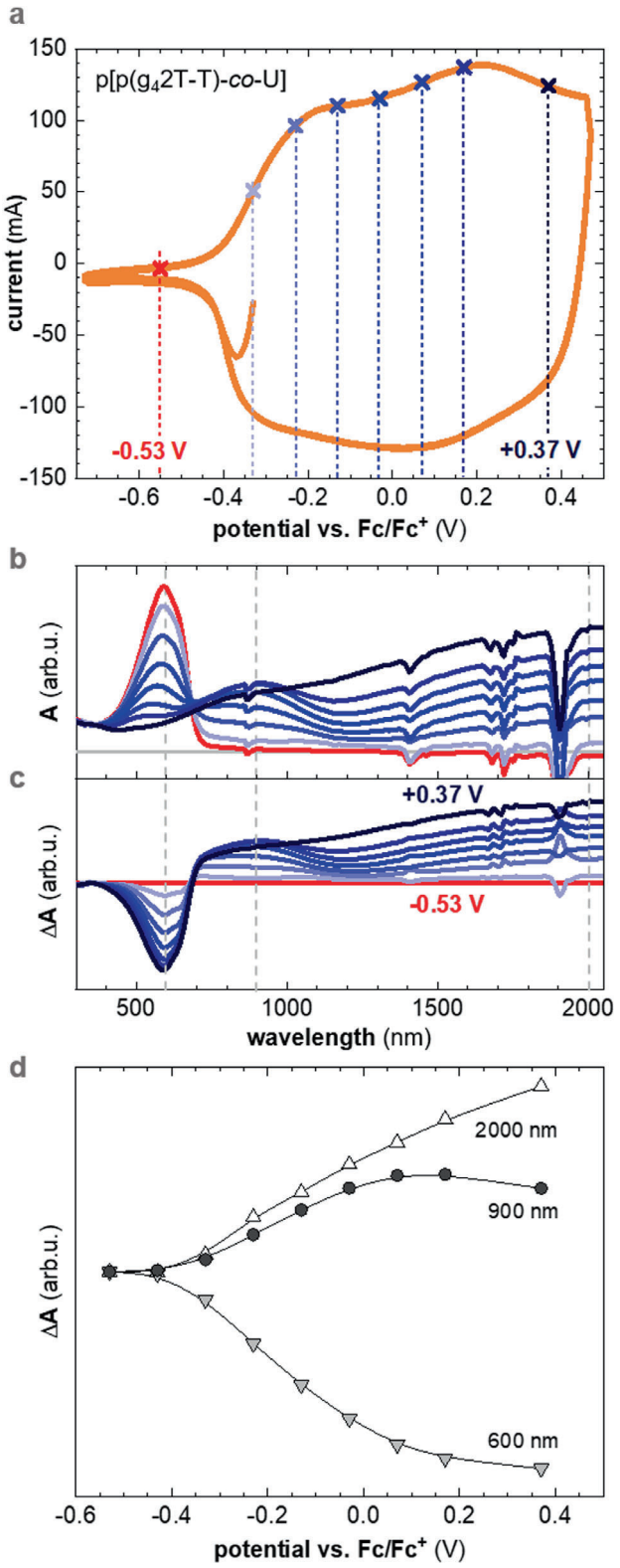

Figure 5. a) Cyclic voltammogram of p[p($g_4$2T-T)-*co*-U] film in 0.1 M solution of [EMIM][BF_4]. b) UV–vis–NIR absorbance spectra recorded at each applied electrochemical potential, and c) difference in absorbance ΔA between neutral and oxidized thin films. d) ΔA at 600 nm, 900 nm, and 2000 nm versus oxidation potential.

Table 2. OECT parameters and material figures of merit ($n = 6$): thickness d, threshold voltage V_t and saturation mobility μ_{sat} extracted from fits of $\sqrt{I_d}$ versus V_g plots; average volumetric capacitance C^* beyond the threshold voltage determined by electrochemical impedance spectroscopy (EIS; $n = 2$); maximum transconductance g_m and μC^* extracted from the slope of saturated transfer curves at $V_g = -0.6$ V; number of measured samples, n, indicated in brackets.

	p($g_4$2T-T)	p[p($g_4$2T-T)-*co*-U]
d [nm]	22 ± 9	18 ± 10
V_t [mV]	−202 ± 5	−314 ± 5
μ_{sat} [cm^2 V^{-1} s^{-1}]	0.39 ± 0.07	0.15 ± 0.10
C^* [F cm^{-3}]	258 ± 102	279 ± 114
μC^* (F cm^{-1} V^{-1} s^{-1})	86 ± 39	36 ± 29
$\mu_{sat} C^*$ [F cm^{-1} V^{-1} s^{-1}]	100 ± 44	42 ± 29
g_m [mS]	0.73 ± 0.14	0.18 ± 0.10

where e is the elementary charge, and obtain a value of $\mu \approx (1.2 \pm 0.2)$ cm^2 V^{-1} s^{-1} for p($g_4$2T-T) and $\mu \approx (0.7 \pm 0.2)$ cm^2 V^{-1} s^{-1} for p[p($g_4$2T-T)-*co*-U] (Table 1). A comparison of the mobility values indicates that the introduction of urethane blocks, which leads to a reduction in the ordering of p($g_4$2T-T) segments as a result of the formation of a hydrogen-bonded network (see WAXS diffractograms, Figure 2b), only slightly reduces μ.

2.7. Organic Electrochemical Transistors (OECTs)

The mixed conducting properties of conjugated polymers with oligoethylene glycol side chains make them ideal candidates for OECTs.[47,48] Integration of OECTs onto flexible arrays for implantable or wearable bioelectronic applications requires mechanical robustness,[5,49] which urethane blocks readily impart. Therefore, OECTs were fabricated and tested employing the homopolymer and copolymer as the semiconducting channel material (**Figure 7**a,b), with the various device parameters collected in **Table 2**. Equally thin p($g_4$2T-T) and p[p($g_4$2T-T)-*co*-U] devices (thickness $d \approx 20$ nm) with identical channel aspect ratio (width to length ratio W/L = 10) both displayed clear transistor behavior (Figure 7c) with a strong turn on (subthreshold swing of (75 ± 2) mV/decade and (87 ± 5) mV/decade, respectively), good ON/OFF ratios of more than 10^4 (Figure 7d), and ideal saturation (Figure 7e,f). The volumetric capacitance C^* for both materials was determined by electrochemical impedance spectroscopy (EIS; Figure S12, Supporting Information). The incorporation of the urethane block had little effect on the volumetric capacitance, with values of $C^* \approx (258 \pm 102)$ F cm^{-3} for p($g_4$2T-T) and $C^* \approx (279 \pm 114)$ F cm^{-3}, for p[p($g_4$2T-T)-*co*-U], which are in good agreement with measurements done on other polythiophenes with oligoethylene glycol side chains.[50] From the slope of the collected transfer curves (I_d vs V_g), the gate transconductance $g_m = dI_d/dV_g$ was calculated, which captures the ability of an OECT to amplify an input. In the saturation regime g_m is given by

$$g_m = \frac{Wd}{L} \mu C^* \left(V_T - V_G \right)$$

where μC^*, the product of volumetric capacitance and charge-carrier mobility μ, represents a figure of merit intrinsic to the

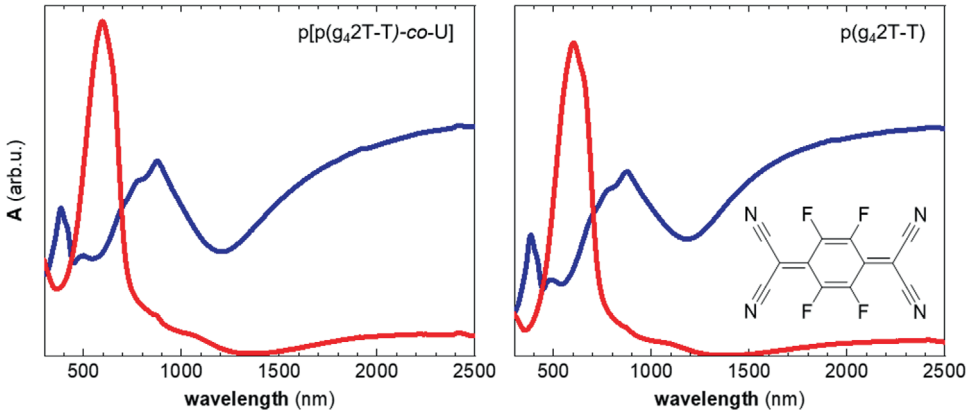

Figure 6. UV–vis–NIR absorbance spectra of ≈60 nm thin films of the copolymer p[p($g_4$2T-T)-*co*-U] (left) and p($g_4$2T-T) (right) after spin-coating (red) and once sequentially doped with F4TCNQ (blue); inset: chemical structure of F4TCNQ.

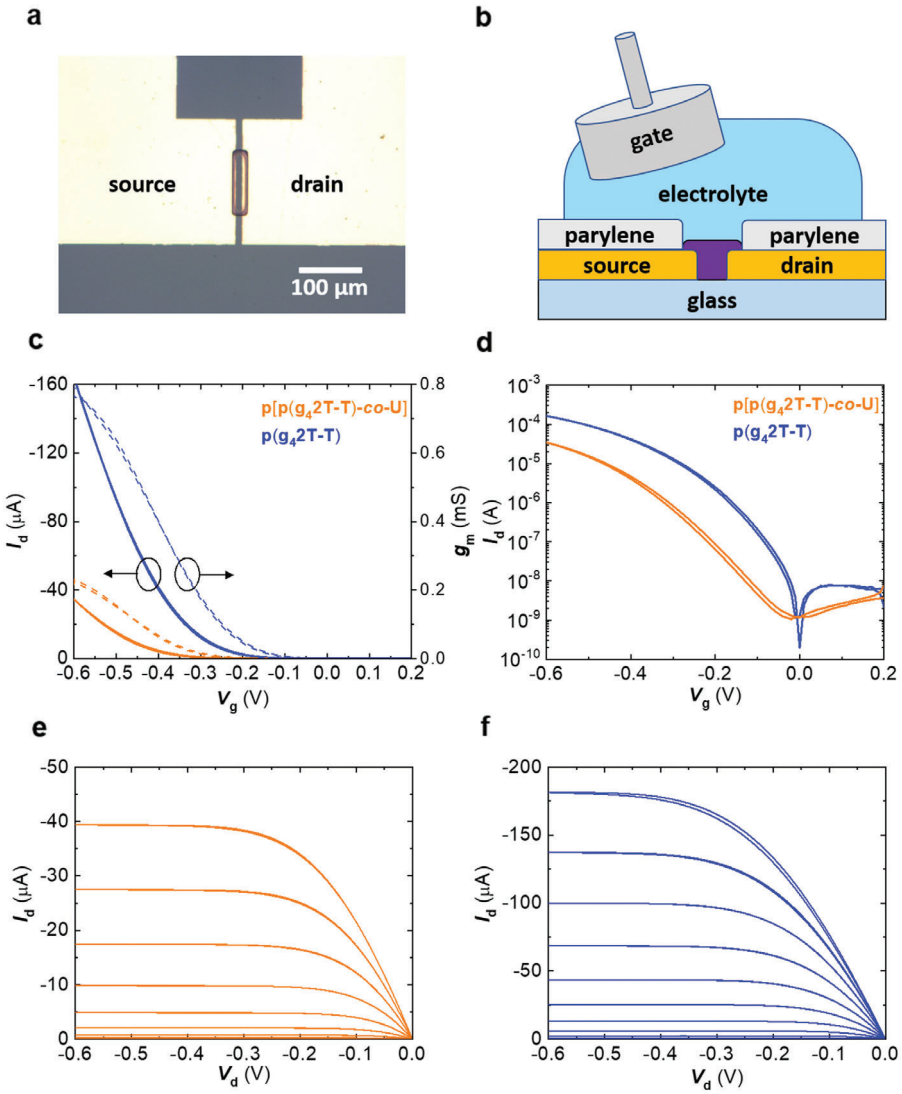

Figure 7. OECTs: a) Micrograph of the patterned semiconducting channel connecting the encapsulated Au source and drain electrodes; b) cross-sectional cartoon of the OECT device structure (not to scale); c) transfer curves (I_d vs V_g) and voltage dependent gate transconductance g_m of p[p($g_4$2T-T)-*co*-U] (orange) and p($g_4$2T-T) (blue) OECTs with a drain bias of −0.6 V. d) Semilog plots of the same transfer curves; output curves of e) p[p($g_4$2T-T)-*co*-U] and f) p($g_4$2T-T) OECTs. All measurements collected at a sweep rate of 200 mV s^{-1} on devices with ≈20 nm thick channels and a width to length ratio W/L = 10.

channel material. Given the channel dimensions, and p($g_4$2T-T) and p[p($g_4$2T-T)-*co*-U] threshold voltages of $V_t \approx (-202 \pm 5)$ mV and (-314 ± 5) mV, respectively, μC^* was directly extractable from the transfer curves. The polymers p($g_4$2T-T) and p[p($g_4$2T-T)-*co*-U] displayed a $\mu C^* \approx (86 \pm 39)$ F cm^{-1} V^{-1} s^{-1} and (36 ± 29) F cm^{-1} V^{-1} s^{-1}, respectively. We ascribe the 60% decrease in μC^* to incorporation of urethane blocks, which led to a decrease in μ (cf. Table 2). The charge-carrier mobility in the saturation regime μ_{sat} was extracted from the slope of $\sqrt{I_{sd}}$ versus V_g plots. As expected, μ_{sat} of p[p($g_4$2T-T)-*co*-U] was ≈60% less than that of p($g_4$2T-T) (Table 2). Alternatively, calculating the figure of merit from the product of transfer curve determined mobility and EIS determined capacitance ($\mu_{sat}C^*$) gave similar values and an identical trend. The μC^* and $\mu_{sat}C^*$ trends for OECTs both mirror the mobility and conductivity trends observed in molecularly doped samples.

Interestingly, C^* is similar for both the homopolymer and copolymer despite a smaller volume fraction of conjugated repeat units in case of the former, which indicates that the presence of urethane blocks actually leads to a higher oxidation level of the conjugate backbone. While the presence of urethane blocks does not inhibit the overall charge storage capacity, C^*, it does delay the onset voltage of charge accumulation V_t. The incorporation of 5 nm long nonconjugated segments that significantly disrupt the ability of conjugated segments to order (cf. Figure 2) likely impairs electronic charge transport. However, the copolymers resistance to swelling seems to counterbalance this, as electrically conductive pathways clearly persist as evidenced by the OECT results.

3. Conclusions

We have synthesized a copolymer consisting of soft p($g_4$2T-T) segments and hard urethane segments. The urethane segments considerably reinforce the polar polythiophene through hydrogen bonding. Free-standing ribbons of the p[p($g_4$2T-T)-*co*-U] copolymer feature a tensile modulus of about 25 MPa and elongation at break of 95%. The presence of the reinforcing urethane segments does not affect the ability to take up charge upon electrochemical oxidation. Both, chemical doping with F4TCNQ and the operation of OECTs indicate that the urethane block only slightly reduces the charge-carrier mobility. We conclude that the introduction of reinforcing segments is a promising strategy for modifying the mechanical and electrochemical properties of polar conjugated polymers. Further work with regard to the type and relative length of the reinforcing segments is needed to create materials that do not show any trade-off between mechanical and electrochemical properties.

4. Experimental Section

Materials: The synthesis of p($g_4$2T-T) ($M_n \approx 24$ kg mol^{-1}; PDI ≈ 3.3) is described elsewhere.[37] The synthetic procedure and corresponding NMR spectra of p[p($g_4$2T-T)-*co*-U] ($M_n \approx 13.5$ kg mol^{-1}; PDI ≈ 2.5) are provided in the Supporting Information. Chloroform (Fisher Scientific), acetonitrile (AcN) (Fisher Scientific), 1,2- dichlorobenzene (o-DCB) (Acros Organics), and anhydrous pyridine (Sigma-Aldrich) where used as received. DMSO from Fisher Scientific was dry distilled and stored over 4 Å molsieves. 2,3,5,6-tetrafluoro-7,7,8,8-tetracyanoquinodimethane (F4TCNQ) and 1-ethyl-3-methylimidazolium tetrafluoroborate ([EMIM][BF_4]) were purchased from Tokyo Chemical Industry (TCI) and Sigma-Aldrich, respectively, and used as received.

Chemical Doping: Films for UV–vis–NIR and conductivity measurements were prepared by spin-coating 80–90 °C hot solutions of the polymers in anhydrous pyridine (10 g L^{-1}) onto hot glass slides. Sequential doping was done at room temperature by drop-casting a solution of F4TCNQ in AcN (10 g L^{-1}) onto thin films, followed by spinning off the remaining solution after 1 min. Doped films were rinsed with AcN to remove excess dopant. The thickness of thin films was measured with a KLA Alphastep Tencor D-100 profilometer.

Size Exclusion Chromatography (SEC): The molecular weight distribution was measured at 40 °C with a TOSOH EcoSEC HLC-8320GPC system (Japan), equipped with an EcoSEC RI detector and three PSS PFG 5 µm columns (microguard, 100, and 300 Å; USA). Poly(methyl methacrylate) (PMMA) standards were used for calibration and toluene was used as an internal standard.

NMR Spectroscopy: NMR spectra were recorded with an automated Agilent (Varian) MR 400 MHz spectrometer (equipped with "one-probe") with $CDCl_3$ or d-DMSO as the solvent. In all cases, the peak values were calibrated relative to the residual solvent signals ($CDCl_3$, 7.26 ppm or d-DMSO, 2.50 ppm).

FTIR: Transmission FTIR spectra were recorded with a PerkinElmer FT-IR Spectrometer "Frontier" on p[p($g_4$2T-T)-*co*-U] drop-cast from DMSO (10 g L^{-1}) onto CaF_2. Variable-temperature transmission FTIR was done by heating from 22 to 220 °C using a Specac electrical heating jacket equipped with a Specac 4000 series temperature controller (West 6100$^+$).

UV–Vis–NIR Absorption Spectroscopy: UV–vis–NIR spectra were recorded with a PerkinElmer Lambda 1050 spectrophotometer.

Analysis of Mechanical Properties: Free-standing films of p[p($g_4$2T-T)-*co*-U] with a thickness of ≈100 µm were prepared by drop-casting from pyridine (10 g L^{-1}) onto microscopy glass slides, from which the specified film could be removed with a sharp blade. Samples of thin films supported by a glass fiber mesh were prepared by coating glass fiber meshes (50 × 5 mm^2) with solutions of the polymers dissolved in pyridine (15 g L^{-1}). DMA and tensile testing were performed using a Q800 (TA Instruments); glass fiber mesh samples were clamped with the glass fiber strands at 45° to the direction of deformation. DMA was carried out at a dynamic strain of 0.05% and a frequency of 1 Hz while ramping the temperature from −90 to 140 °C (glass fiber mesh samples) and −70 to 40 °C (free-standing p[p($g_4$2T-T)-*co*-U], gauge length = 4.5 mm) at 3 °C min^{-1} with a preload force of 0.01 N. Tensile testing was performed at room temperature and a strain rate of 0.5 N min^{-1} with a preload force of 0.02 N and gauge length = 3.8 mm.

WAXS: WAXS was done using a piece of as-synthesized p($g_4$2T-T) and a film sample prepared for DMA in case of p[p($g_4$2T-T)-*co*-U]. WAXS diffractograms were obtained using a Mat:Nordic instrument from SAXSLAB equipped with a Rigaku 003+ high brilliance micro focus Cu-radiation source (wavelength = 1.5406 Å) and a Pilatus 300 K detector placed at a distance of 88.6 mm from the sample.

Transmission Electron Microscopy (TEM): Samples for TEM were prepared by spin-coating p($g_4$2T-T) from chloroform (1 g L^{-1}) or p[p($g_4$2T-T)-*co*-U] from anhydrous pyridine (1 g L^{-1}) onto glass slides coated with poly(diallyldimethylammonium chloride) (PDADMAC). Pieces of polymer films were floated off in water and collected with a copper grid. TEM was done with a FEI Titan 80–300 operated in STEM mode at an acceleration voltage of 300 kV. Images were recorded using a signal from a high-angle annular dark-field detector.

Spectroelectrochemistry: Electrochemical measurements were performed with freshly prepared solutions of [EMIM][BF_4] in dry and degassed AcN (0.1 M) using a custom made three-electrode setup in a standard 1 × 1 cm^2 quartz cuvette. Polymer films were spin-coated from pyridine (10 g L^{-1}) onto ITO coated glass (R ≈150 Ohm sq^{-1}), which served as the working electrode. A Pt wire (∅ ≈ 1 mm) and Ag wire served as the counter and pseudoreference electrode. The potentials were calibrated versus the Ferrocene/Ferrocenium (Fc/Fc^+) redox couple. Cyclic voltammograms were recorded with a scan rate of 100 mV s^{-1} using a 650D electrochemical workstation from CH Instruments. The ionization energies of

the polymers were calculated using IE = 5.1 eV + E_{ox} versus Fc/Fc$^+$, where E_{ox} is the oxidation onset versus Fc/Fc$^+$. Spectroelectrochemistry was performed by recording UV–vis–NIR spectra at different oxidation potentials with a PerkinElmer Lambda 1050 spectrophotometer.

Swelling Experiments: Carbon filaments (diameter ≈ 34.5 µm ± 2.5 µm; provided by Specialty Materials, USA) were coaxially coated with p($g_4$2T-T) from chloroform or p[p($g_4$2T-T)-*co*-U] from pyridine, and left to dry at room temperature. The electrochemical cell consisted of a coated carbon filament working electrode (and reference uncoated fiber), a Pt counter electrode and an Ag/AgCl wire reference electrode, which were arranged between two glass slides separated by a poly(dimethylsiloxane) (PDMS) well that contained the electrolyte (0.01 M KCl). Cyclic voltammetry was performed with a Metrohm µAutolab Type III (NOVA 2.1 software) between ± 0.8 V at a scan rate of 10 mV s^{-1}, with simultaneous monitoring of the volume change using a Nikon SMZ1500 stereo microscope equipped with a Nikon DS-Fi1 camera. The volume of the swollen polymer coating at different potentials was calculated from the average width of the coated carbon filament assuming a cylindrical shape.

OECTs: OECTs test chips were prepared following previously reported microfabrication techniques.[51] OECT channels were fabricated by spin-coating p($g_4$2T-T) from chloroform (2.5 g L^{-1}) or p[p($g_4$2T-T)-*co*-U] from filtered o-DCB solution (2 g L^{-1}) onto OECT test chips at room temperature, followed by patterning via removal of a sacrificial parylene layer. OECTs were gated with aqueous 100 × 10^{-3} M NaCl using a Ag/AgCl pellet as the faradaic gate electrode.[52] Electrical characterization of the OECTs was carried out using source-measure units from National Instruments controlled by custom LabView code. The capacitance was determined via EIS using a Metrohm potentiostat with a frequency response analyzer with a Ag/AgCl pellet functioning as a combined reference and counter electrode.[52]

Electrical Conductivity Measurements: The electrical resistivity was measured with a 4-point probe setup from Jandel Engineering (cylindrical probe head, RM3000) using colinear tungsten carbide electrodes with equidistant spacing of 1 mm. The in-line 4-point probe for films gives a measure of the sheet resistance $r_s = \frac{\pi}{\ln 2} \cdot V/I$, where $\pi/\ln 2$ is a geometrical correction factor. The conductivity was calculated according to $\sigma = 1/(t \cdot r_s)$.

Statistical Analysis: The number of measured samples are given in the legends of Tables 1 and 2; reported values and errors correspond to the mean and standard deviation.

Supporting Information

Supporting Information is available from the Wiley Online Library or from the author.

Acknowledgements

S.Z. and R.K. contributed equally to this work. The authors gratefully acknowledge financial support from the Swedish Research Council through Grants Nos. 2016-06146 and 2018-03824, the Knut and Alice Wallenberg Foundation through a Wallenberg Academy Fellowship, and the European Research Council (ERC) under Grant Agreement No. 637624. WAXS measurements and electron microscopy were performed at the Chalmers Material Analysis Laboratory (CMAL). The authors thank R. B. Rashid for fabricating OECT test chips. B.D.P. and J.R. gratefully acknowledge support from the National Science Foundation Grant No. NSF DMR-1751308. W.S. gratefully acknowledges support from the Northwestern University Office of Undergraduate Research. This work utilized the Keck-II facility of Northwestern University's NUANCE Center and the Northwestern University Micro/Nano Fabrication Facility (NUFAB), which are both partially supported by Soft and Hybrid Nanotechnology Experimental (SHyNE) Resource (NSF ECCS-1542205), the Materials Research Science and Engineering Center (NSF DMR-1720139), the State of Illinois, and Northwestern University. Additionally, the Keck-II facility is partially supported by the International Institute for Nanotechnology (IIN); the Keck Foundation; and the State of Illinois, through the IIN. J.G. and E.S. gratefully acknowledge support from The Wallenberg Wood Science Center (KAW 2018.0452). The authors thank Prof. Enrique Gomez for highly insightful discussions.

Conflict of Interest

The authors declare no conflict of interest.

Keywords

chemical and electrochemical doping, organic electrochemical transistors (OECT), polar conjugated polymers, swelling, urethane

Received: July 22, 2020
Revised: October 1, 2020
Published online: December 11, 2020

[1] T. Someya, Z. Bao, G. G. Malliaras, *Nature* **2016**, *540*, 379.
[2] Z. Bao, X. Chen, *Adv. Mater.* **2016**, *28*, 4177.
[3] B. Wang, A. Facchetti, *Adv. Mater.* **2019**, *31*, 1901408.
[4] M. Wang, P. Baek, A. Akbarinejad, D. Barker, J. Travas-Sejdic, *J. Mater. Chem. C* **2019**, *7*, 5534.
[5] S. E. Root, S. Savagatrup, A. D. Printz, D. Rodriquez, D. J. Lipomi, *Chem. Rev.* **2017**, *117*, 6467.
[6] R. Xie, R. H. Colby, E. D. Gomez, *Adv. Electron. Mater.* **2018**, *4*, 1700356.
[7] C. Müller, *Chem. Mater.* **2015**, *27*, 2740.
[8] B. Roth, S. Savagatrup, N. V. de los Santos, O. Hagemann, J. E. Carlé, M. Helgesen, F. Livi, E. Bundgaard, R. R. Søndergaard, F. C. Krebs, D. J. Lipomi, *Chem. Mater.* **2016**, *28*, 2363.
[9] R. Peng, B. Pang, D. Hu, M. Chen, G. Zhang, X. Wang, H. Lu, K. Cho, L. Qiu, *J. Mater. Chem. C* **2015**, *3*, 3599.
[10] P. Baek, N. Aydemir, Y. An, E. W. C. Chan, A. Sokolova, A. Nelson, J. P. Mata, D. McGillivray, D. Barker, J. Travas-Sejdic, *Chem. Mater.* **2017**, *29*, 8850.
[11] A. X. Chen, A. T. Kleinschmidt, K. Choudhary, D. J. Lipomi, *Chem. Mater.* **2020**, *32*, 7582.
[12] J. Y. Oh, S. Rondeau-Gagné, Y.-C. Chiu, A. Chortos, F. Lissel, G.-J. N. Wang, B. C. Schroeder, T. Kurosawa, J. Lopez, T. Katsumata, J. Xu, C. Zhu, X. Gu, W.-G. Bae, Y. Kim, L. Jin, J. W. Chung, J. B. H. Tok, Z. Bao, *Nature* **2016**, *539*, 411.
[13] Y. Zheng, M. Ashizawa, S. Zhang, J. Kang, S. Nikzad, Z. Yu, Y. Ochiai, H.-C. Wu, H. Tran, J. Mun, Y.-Q. Zheng, J. B. H. Tok, X. Gu, Z. Bao, *Chem. Mater.* **2020**, *32*, 5700.
[14] F. Sugiyama, A. T. Kleinschmidt, L. V. Kayser, M. A. Alkhadra, J. M. H. Wan, A. S. C. Chiang, D. Rodriquez, S. E. Root, S. Savagatrup, D. J. Lipomi, *Macromolecules* **2018**, *51*, 5944.
[15] Y. Zhao, X. Zhao, Y. Zang, C.-a. Di, Y. Diao, J. Mei, *Macromolecules* **2015**, *48*, 2048.
[16] A. Gasperini, S. Bivaud, K. Sivula, *Chem. Sci.* **2014**, *5*, 4922.
[17] S. Savagatrup, X. Zhao, E. Chan, J. Mei, D. J. Lipomi, *Macromol. Rapid Commun.* **2016**, *37*, 1623.
[18] B. C. Schroeder, Y.-C. Chiu, X. Gu, Y. Zhou, J. Xu, J. Lopez, C. Lu, M. F. Toney, Z. Bao, *Adv. Electron. Mater.* **2016**, *2*, 1600104.
[19] M. Ashizawa, Y. Zheng, H. Tran, Z. Bao, *Prog. Polym. Sci.* **2020**, *100*, 101181.
[20] J. Mun, G.-J. N. Wang, J. Y. Oh, T. Katsumata, F. L. Lee, J. Kang, H.-C. Wu, F. Lissel, S. Rondeau-Gagné, J. B.-H. Tok, Z. Bao, *Adv. Funct. Mater.* **2018**, *28*, 1804222.

[21] S. Savagatrup, A. D. Printz, D. Rodriquez, D. J. Lipomi, *Macromolecules* **2014**, *47*, 1981.
[22] Z. C. Smith, Z. M. Wright, A. M. Arnold, G. Sauvé, R. D. McCullough, S. A. Sydlik, *Adv. Electron. Mater.* **2017**, *3*, 1600316.
[23] S. Pankaj, E. Hempel, M. Beiner, *Macromolecules* **2009**, *42*, 716.
[24] R. Xie, A. R. Weisen, Y. Lee, M. A. Aplan, A. M. Fenton, A. E. Masucci, F. Kempe, M. Sommer, C. W. Pester, R. H. Colby, E. D. Gomez, *Nat. Commun.* **2020**, *11*, 893.
[25] A. Giovannitti, D.-T. Sbircea, S. Inal, C. B. Nielsen, E. Bandiello, D. A. Hanifi, M. Sessolo, G. G. Malliaras, I. McCulloch, J. Rivnay, *Proc. Natl. Acad. Sci. USA* **2016**, *113*, 12017.
[26] C. B. Nielsen, A. Giovannitti, D.-T. Sbircea, E. Bandiello, M. R. Niazi, D. A. Hanifi, M. Sessolo, A. Amassian, G. G. Malliaras, J. Rivnay, I. McCulloch, *J. Am. Chem. Soc.* **2016**, *138*, 10252.
[27] A. Giovannitti, C. B. Nielsen, D.-T. Sbircea, S. Inal, M. Donahue, M. R. Niazi, D. A. Hanifi, A. Amassian, G. G. Malliaras, J. Rivnay, I. McCulloch, *Nat. Commun.* **2016**, *7*, 13066.
[28] A. Savva, R. Hallani, C. Cendra, J. Surgailis, T. C. Hidalgo, S. Wustoni, R. Sheelamanthula, X. Chen, M. Kirkus, A. Giovannitti, A. Salleo, I. McCulloch, S. Inal, *Adv. Funct. Mater.* **2020**, *30*, 1907657.
[29] C. K. Song, B. J. Eckstein, T. L. D. Tam, L. Trahey, T. J. Marks, *ACS Appl. Mater. Interfaces* **2014**, *6*, 19347.
[30] D. Moia, A. Giovannitti, A. A. Szumska, I. P. Maria, E. Rezasoltani, M. Sachs, M. Schnurr, P. R. F. Barnes, I. McCulloch, J. Nelson, *Energy Environ. Sci.* **2019**, *12*, 1349.
[31] A. V. Volkov, H. Sun, R. Kroon, T.-P. Ruoko, C. Che, J. Edberg, C. Müller, S. Fabiano, X. Crispin, *ACS Appl. Energy Mater.* **2019**, *2*, 5350.
[32] J. Brebels, J. V. Manca, L. Lutsen, D. Vanderzande, W. Maes, *J. Mater. Chem. A* **2017**, *5*, 24037.
[33] D. Kiefer, A. Giovannitti, H. Sun, T. Biskup, A. Hofmann, M. Koopmans, C. Cendra, S. Weber, L. J. Anton Koster, E. Olsson, J. Rivnay, S. Fabiano, I. McCulloch, C. Müller, *ACS Energy Lett.* **2018**, *3*, 278.
[34] J. Liu, L. Qiu, R. Alessandri, X. Qiu, G. Portale, J. Dong, W. Talsma, G. Ye, A. A. Sengrian, P. C. T. Souza, M. A. Loi, R. C. Chiechi, S. J. Marrink, J. C. Hummelen, L. J. A. Koster, *Adv. Mater.* **2018**, *30*, 1704630.
[35] B. Meng, J. Liu, L. Wang, *Polym. Chem.* **2020**, *11*, 1261.
[36] D. Ohayon, G. Nikiforidis, A. Savva, A. Giugni, S. Wustoni, T. Palanisamy, X. Chen, I. P. Maria, E. Di Fabrizio, P. M. F. J. Costa, I. McCulloch, S. Inal, *Nat. Mater.* **2020**, *19*, 456.
[37] R. Kroon, D. Kiefer, D. Stegerer, L. Yu, M. Sommer, C. Müller, *Adv. Mater.* **2017**, *29*, 1700930.
[38] R. Kroon, D. A. Mengistie, D. Kiefer, J. Hynynen, J. D. Ryan, L. Yu, C. Müller, *Chem. Soc. Rev.* **2016**, *45*, 6147.
[39] A. Lund, N. M. van der Velden, N.-K. Persson, M. M. Hamedi, C. Müller, *Mater. Sci. Eng., R* **2018**, *126*, 1.
[40] M. Szycher, *Szycher's Handbook of Polyurethanes*, 2nd ed., CRC Press, Boca Raton, FL **1991**.
[41] J. O. Akindoyo, M. D. H. Beg, S. Ghazali, M. R. Islam, N. Jeyaratnam, A. R. Yuvaraj, *RSC Adv.* **2016**, *6*, 114453.
[42] K. G. Chittibabu, S. Balasubramanian, W. H. Kim, A. L. Cholli, J. Kumar, S. K. Tripathy, *J. Macromol. Sci. A* **1996**, *33*, 1283.
[43] A. I. Hofmann, R. Kroon, L. Yu, C. Müller, *J. Mater. Chem. C* **2018**, *6*, 6905.
[44] A. Sharma, X. Pan, J. A. Campbell, M. R. Andersson, D. A. Lewis, *Macromolecules* **2017**, *50*, 3347.
[45] J. Gladisch, E. Stavrinidou, S. Ghosh, A. Giovannitti, M. Moser, I. Zozoulenko, I. McCulloch, M. Berggren, *Adv. Sci.* **2020**, *7*, 1901144.
[46] A. Richter, S. Howitz, D. Kuckling, K.-F. Arndt, *Sens. Actuators, B* **2004**, *99*, 451.
[47] B. D. Paulsen, K. Tybrandt, E. Stavrinidou, J. Rivnay, *Nat. Mater.* **2020**, *19*, 13.
[48] J. Rivnay, S. Inal, A. Salleo, R. M. Owens, M. Berggren, G. G. Malliaras, *Nat. Rev. Mater.* **2018**, *3*, 17086.
[49] H.-R. Lim, H. S. Kim, R. Qazi, Y.-T. Kwon, J.-W. Jeong, W.-H. Yeo, *Adv. Mater.* **2020**, *32*, 1901924.
[50] S. Inal, G. G. Malliaras, J. Rivnay, *Nat. Commun.* **2017**, *8*, 1767.
[51] Z. S. Parr, R. B. Rashid, B. D. Paulsen, B. Poggi, E. Tan, M. Freeley, M. Palma, I. Abrahams, J. Rivnay, C. B. Nielsen, *Adv. Electron. Mater.* **2020**, *6*, 2000215.
[52] G. Tarabella, C. Santato, S. Y. Yang, S. Iannotta, G. G. Malliaras, F. Cicoira, *Appl. Phys. Lett.* **2010**, *97*, 123304.

Paper II

Ground-state electron transfer in all-polymer donor–acceptor heterojunctions

Kai Xu, Hengda Sun, Tero-Petri Ruoko, Gang Wang, Renee Kroon, Nagesh B. Kolhe, Yuttapoom Puttisong, Xianjie Liu, Daniele Fazzi, Koki Shibata, Chi-Yuan Yang, Ning Sun, Gustav Persson, Andrew B. Yankovich, Eva Olsson, Hiroyuki Yoshida, Weimin M. Chen, Mats Fahlman, Martijn Kemerink, Samson A. Jenekhe, Christian Müller, Magnus Berggren and Simone Fabiano

Nature Materials, 2020, 19, 738–744

nature materials

ARTICLES

https://doi.org/10.1038/s41563-020-0618-7

Ground-state electron transfer in all-polymer donor–acceptor heterojunctions

Kai Xu[1], Hengda Sun[1]✉, Tero-Petri Ruoko[1], Gang Wang[1], Renee Kroon[2], Nagesh B. Kolhe[3], Yuttapoom Puttisong[4], Xianjie Liu[1], Daniele Fazzi[5], Koki Shibata[6], Chi-Yuan Yang[1], Ning Sun[7], Gustav Persson[8], Andrew B. Yankovich[8], Eva Olsson[8,9], Hiroyuki Yoshida[10,11], Weimin M. Chen[4], Mats Fahlman[1,12], Martijn Kemerink[13], Samson A. Jenekhe[3], Christian Müller[2,9], Magnus Berggren[1,12]✉ and Simone Fabiano[1,12]✉

Doping of organic semiconductors is crucial for the operation of organic (opto)electronic and electrochemical devices. Typically, this is achieved by adding heterogeneous dopant molecules to the polymer bulk, often resulting in poor stability and performance due to dopant sublimation or aggregation. In small-molecule donor–acceptor systems, charge transfer can yield high and stable electrical conductivities, an approach not yet explored in all-conjugated polymer systems. Here, we report ground-state electron transfer in all-polymer donor–acceptor heterojunctions. Combining low-ionization-energy polymers with high-electron-affinity counterparts yields conducting interfaces with resistivity values five to six orders of magnitude lower than the separate single-layer polymers. The large decrease in resistivity originates from two parallel quasi-two-dimensional electron and hole distributions reaching a concentration of ~10^{13} cm^{-2}. Furthermore, we transfer the concept to three-dimensional bulk heterojunctions, displaying exceptional thermal stability due to the absence of molecular dopants. Our findings hold promise for electro-active composites of potential use in, for example, thermoelectrics and wearable electronics.

Doping is an essential process needed to define and optimize the performance of organic electronic and electrochemical devices. In particular, this is true when high or precise control over the electrical conductivity is required in devices based on intrinsic semiconducting conjugated organic materials[1–5]. Both p- and n-doping are widely used in various devices, such as in the charge injection/extraction layers of organic light emitting diodes (OLEDs), organic solar cells (OSCs) and organic field effect transistors, as well as in the active materials of thermoelectric generators and electrochemical transistors[3–10]. Typically, this is done by the addition of heterogeneous dopant molecules or polyelectrolytes that, once the electrical doping process is completed, not only become redundant but often negatively affect both the electrical and mechanical properties of the semiconductor through generation of non-conducting phases inside the doped bulk[11,12], or reduction of the mobility due to Coulomb scattering[13,14]. While many polymer–dopant systems exist that are stable on mild thermal annealing, more rapid diffusion and sublimation occurs at higher temperatures[15], which can ultimately lead to degradation of the electrical properties[16–20].

Intuitively, if one brings two different semiconducting polymers in physical contact and if the electron affinity of one (acceptor, A) polymer matches the ionization energy of the other (donor, D) polymer at the interface[21], electron transfer from D to A may occur spontaneously in the electronic ground state, without any external excitation or charge injection. By its nature, such a spontaneous process will create an equal number of mobile positive and negative charge carriers, and the process cannot be compared to conventional n- or p-doping where only one type of charge carrier can be mobile. The exclusion of immobile counter charges may be anticipated to solve issues related to stability, phase segregation and morphology perturbation, features that will negatively affect charge carrier mobility. In small-molecule D–A systems, this concept has been demonstrated in the form of charge transfer salts, resulting in conducting systems with metallic transport properties[22]. However, charge transfer salts either suffer from poor film forming capabilities[23,24], or they rely on the use of single crystals[25,26], and have therefore limited practical applications. The use of all-polymer electron transfer heterojunctions could potentially solve these issues. However, while previously debated[27], ground-state electron transfer (GSET) in all-polymer blends has not been realized.

Here, we report a systematic study of GSET in all-polymer D–A heterojunctions, providing an efficient approach for generating highly mobile charges in polymer semiconductors. We find that conducting interfaces with sheet resistances of around 2 MΩ sq^{-1} are obtained when the high-electron-affinity acceptor (electron-transporting) polymer poly(benzimidazobenzophenanthroline) (BBL) is combined with low-ionization-energy donor

[1]Laboratory of Organic Electronics, Department of Science and Technology, Linköping University, Norrköping, Sweden. [2]Department of Chemistry and Chemical Engineering, Chalmers University of Technology, Göteborg, Sweden. [3]Department of Chemical Engineering and Department of Chemistry, University of Washington, Seattle, WA, USA. [4]Department of Physics, Chemistry and Biology, Linköping University, Linköping, Sweden. [5]Institute of Physical Chemistry, Department Chemistry, University of Cologne, Cologne, Germany. [6]Graduate School of Science and Engineering, Chiba University, Inage-ku, Chiba, Japan. [7]Department of Physics, Center for Optoelectronics Engineering Research, Yunnan University, Kunming, China. [8]Department of Physics, Chalmers University of Technology, Göteborg, Sweden. [9]Wallenberg Wood Science Center, Chalmers University of Technology, Göteborg, Sweden. [10]Graduate School of Engineering, Chiba University, Inage-ku, Chiba, Japan. [11]Molecular Chirality Research Center, Chiba University, Inage-ku, Chiba, Japan. [12]Wallenberg Wood Science Center, Linköping University, Norrköping, Sweden. [13]Complex Materials and Devices, Department of Physics Chemistry and Biology, Linköping University, Linköping, Sweden. ✉e-mail: hengda.sun@liu.se; magnus.berggren@liu.se; simone.fabiano@liu.se

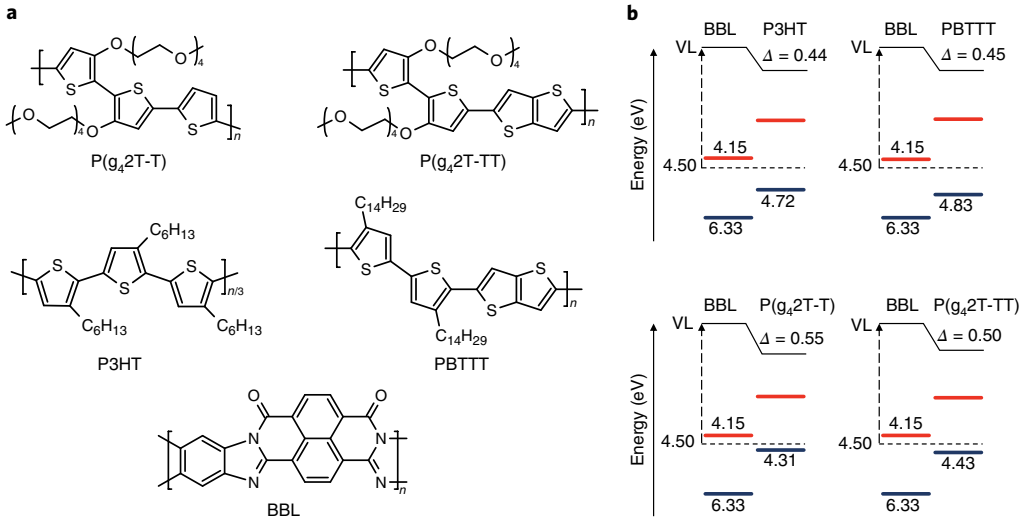

Fig. 1 | Energetics of the all-polymer D–A heterojunctions. a, Chemical structures of P($g_4$2T-T), P($g_4$2T-TT), P3HT, PBTTT and BBL. **b**, Energy level diagrams of the all-polymer D–A heterojunctions as obtained by UPS and LEIPS (electron affinity in red and ionization energy in blue). The resulting down-shift (Δ, in eV) of the vacuum level (VL) for P3HT–BBL, PBTTT–BBL, P($g_4$2T-T)–BBL and P($g_4$2T-TT)–BBL heterojunctions is reported in the diagram.

(hole-transporting) polymers, namely bithiophene-thiophene (P($g_4$2T-T)) or bithiophene-thienothiophene (P($g_4$2T-TT)) copolymers, carrying oligoethylene glycol side chains (Fig. 1a). Two parallel quasi-two-dimensional electron and hole distributions, each reaching a concentration of 10^{13} cm^{-2}, are confined to nanometre-thin layers and hence correspond to an electrical conductivity of about 2 (S cm^{-1}). The remarkable vacuum level shift and spin signals observed in ultraviolet photoelectron spectroscopy (UPS) and electron paramagnetic resonance (EPR) measurements, respectively, are attributed to the formation of polarons induced by spontaneous electron transfer at the D–A heterointerfaces. Ultraviolet–visible (UV–vis) absorption spectra, combined with quantum-chemical calculations, further revealed that both negative and positive polarons are present in the bilayer. It can be anticipated that our discovery of all-polymer GSET will have a similar effect on the field of organic electronics as the discovery of all-polymer excited state charge transfer in the context of OLEDs and OSCs[28,29].

The bilayer energetics were studied by UPS and low-energy inverse photoelectron spectroscopy (LEIPS)[30,31]. The resulting energy level diagrams are given in Fig. 1b. BBL films were prepared on a series of conducting substrates (Al, Au, ITO, PEDOT:PSS) spanning a range of work functions. The resulting BBL–substrate work function (4.50 ± 0.04 eV) and BBL ionization energy (6.33 ± 0.04 eV) were found to be substrate-independent (Supplementary Fig. 1). The substrate-independent work function suggests the existence of a free charge density in the as-prepared BBL films that is sufficiently large to equilibrate the Fermi level (chemical potential) across the BBL–substrate interface. From the LEIPS measurements, the electron affinity of BBL was determined to be 4.15 ± 0.02 eV (Supplementary Fig. 2). Films of the two donors P($g_4$2T-T) and P($g_4$2T-TT), as well as of the corresponding polymers carrying alkyl side chains, namely poly(3-hexylthiophene) (P3HT) and poly[2,5-bis(3-tetradecylthiophen-2-yl)thieno[3,2-b]thiophene] (PBTTT), were spin-cast on a series of high work function substrates to obtain their so-called pinning energies[32–34]. The latter can then be used to predict the energy level alignment, including the size and direction of the vacuum level shift, at weakly interacting organic semiconductor interfaces[35,36]. A second series of films were then fabricated on identically prepared BBL/PEDOT:PSS/ITO substrates and the resulting change in work functions was measured using UPS for each donor polymer (Supplementary Fig. 3), thereby obtaining an estimate of the vacuum level shift (Fig. 1b). The obtained work functions and vacuum level shifts are in excellent agreement with estimates based on the measured donor polymer pinning energies. P3HT–BBL and PBTTT–BBL interfaces show almost identical vacuum level shifts (0.45 eV), indicating a similar amount of electron transfer from the two donors to BBL. For P($g_4$2T-TT)–BBL and P($g_4$2T-T)–BBL, the vacuum level shifts are larger than for P3HT–BBL and PBTTT–BBL, with values of 0.50 and 0.55 eV, respectively. Hence, the UPS data show that GSET is stronger for P($g_4$2T-T) followed by P($g_4$2T-TT), while P3HT and PBTTT yield the least GSET.

Bilayer films were prepared by spin coating the donor polymers on top of BBL films from orthogonal solvents (see Methods for further details). This results in a two-dimensional interface between the donor and acceptor polymers (Supplementary Figs. 4 and 5). Grazing-incidence wide-angle X-ray scattering shows that the bilayer diffraction pattern is predominantly a superposition of the donor and acceptor patterns (Supplementary Figs. 6 and 7). Figure 2a shows representative current–voltage (I–V) characteristics of pristine BBL, P($g_4$2T-T) and P($g_4$2T-TT) films as well as P($g_4$2T-T)–BBL and P($g_4$2T-TT)–BBL bilayer films measured at room temperature in a two-terminal lateral device configuration (Fig. 2a, inset). We measured ten devices for each kind of pristine polymer and bilayer film, all exhibiting an excellent level of device-to-device reproducibility. In all cases, the I–V curves show a linear response without any noticeable limitations from the electrical contacts. Moreover, the comparison of two- and four-terminal measurements, which show comparable resistivity values, indicates that the contact resistance can be neglected (Supplementary Fig. 8). The average sheet resistances are shown in Fig. 2b. The room-temperature resistance measured on individual ~20-nm-thin films of each polymer is typically larger than 100 GΩ sq^{-1}. In contrast, when P($g_4$2T-T) and P($g_4$2T-TT) are spin coated on top of BBL to form bilayers, the resistance drops by more than five orders of magnitude as compared to the pristine films, now reaching a value of 2.3 ± 0.4 MΩ sq^{-1}. Note that the latter value reflects the charge transport in a single quasi-two-dimensional interfacial layer, resulting in an electrical conductivity of about 2 S cm^{-1} as detailed next. This large drop in room-temperature resistance is indicative of a strongly enhanced conductivity due to interfacial GSET. The resistance is found to be independent of the individual donor and acceptor polymer film thickness (Supplementary Fig. 9), suggesting that

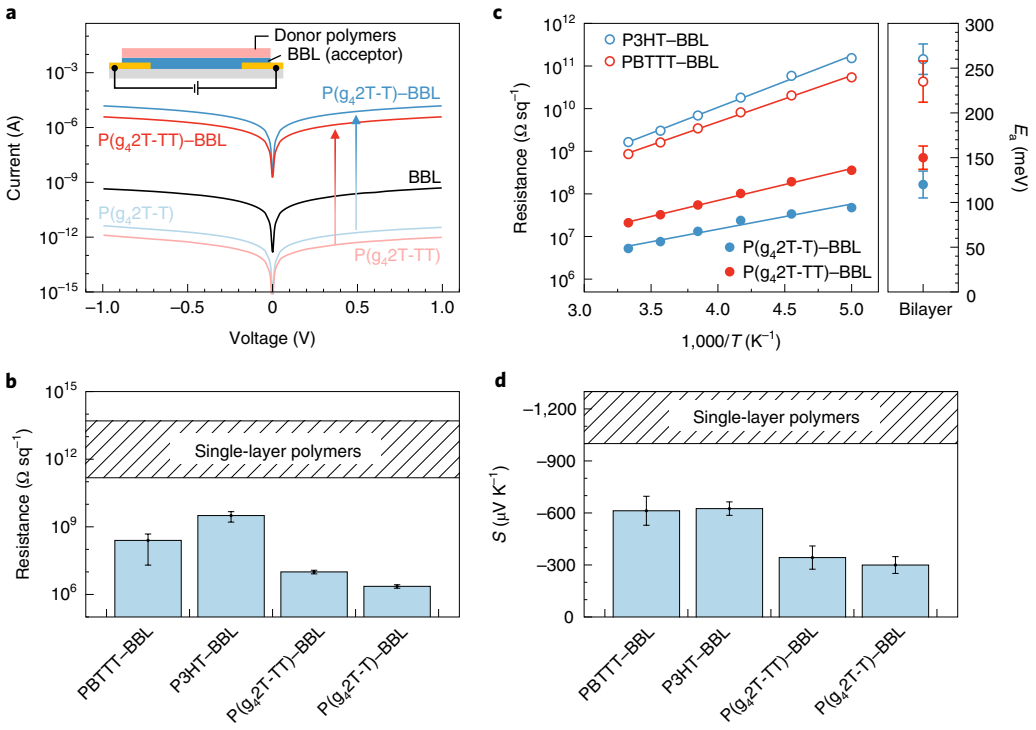

Fig. 2 | Electrical characterization of the all-polymer D–A heterojunctions. a, *I–V* curves of all-polymer-based devices. The inset shows the two-terminal lateral device configuration used for the measurement. **b**, Column diagram of resistance statistics of BBL, P($g_4$2T-T), P($g_4$2T-TT) and the corresponding bilayer films; error bars represent standard deviation. **c**, Resistance of the bilayer film as a function of temperature, and corresponding activation energies; error bars represent standard deviation. **d**, Seebeck coefficient of P($g_4$2T-T)–BBL, P($g_4$2T-TT)–BBL, P3HT–BBL and PBTTT–BBL bilayer films; error bars represent standard deviation.

GSET is limited to the first few molecular layers on either side of the interface (see Fig. 3)[22]. For comparison, we measured the changes in resistance when donor polymers with high ionization energy (P3HT and PBTTT) were spin coated on top of the BBL layer. The room-temperature resistance of the resulting bilayers varied by less than three orders of magnitude, reaching values in the range of 300–3,000 MΩ sq^{-1} (Supplementary Fig. 10). To assess the effect of the dielectric environment on GSET, we used poly(3-carboxy-pentyl-thiophene) (P3CPT), a conjugated polyelectrolyte having a similar dielectric constant ($\varepsilon_e = 3.9 \pm 0.1$) to P($g_4$2T-TT) ($4.2 \pm 0.1$)[37] and P($g_4$2T-T) ($4.4 \pm 0.2$) but higher ionization energy (4.84 ± 0.04 eV) (Supplementary Figs. 3 and 11). When P3CPT was spun on top of BBL, we observed no significant vacuum level shift as well as high resistance values (1.2 ± 0.7 GΩ sq^{-1}) (Supplementary Fig. 12), as in the case of P3HT–BBL and PBTTT–BBL bilayers. In addition, pure tetraethylene glycol, drop-cast on top of BBL, also results in high resistance values (2.1 ± 0.2 GΩ sq^{-1}, see Supplementary Fig. 12), indicating that a polar environment alone cannot explain the decrease in resistance. The temperature dependence of the resistance for P($g_4$2T-T)–BBL, P($g_4$2T-TT)–BBL, P3HT–BBL and PBTTT–BBL bilayers is summarized in the Arrhenius plot of Fig. 2c. For a given voltage, the current in P($g_4$2T-T)–BBL and P($g_4$2T-TT)–BBL bilayers decreases as the temperature is lowered from 300 to 200 K. The linearity of the data for P($g_4$2T-T)–BBL and P($g_4$2T-TT)–BBL interfaces indicates that conduction at the D–A interface is thermally activated. Activation energies of 120 ± 15 and 150 ± 13 meV are obtained for electron and hole transport along the P($g_4$2T-T)–BBL and P($g_4$2T-TT)–BBL interfaces, respectively, smaller than those extracted for P3HT–BBL (260 ± 17 meV) and PBTTT–BBL (235 ± 23 meV). This further supports an increase in the carrier density due to GSET when donor polymers with a low ionization energy are used[38].

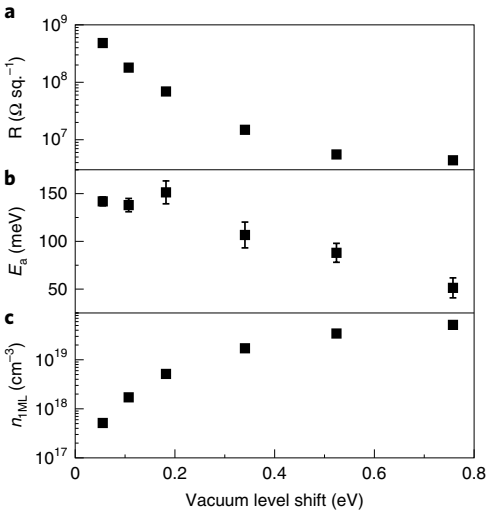

Fig. 3 | Kinetic Monte Carlo simulation of GSET heterojunctions. **a**–**c**, Calculated resistance (R) (**a**), activation energy (E_a) (**b**) and charge density (n_{1ML}) (**c**) versus vacuum level shift for a single bilayer. To facilitate comparison with experiment, the charge density in **c** is calculated by assuming the total charge density sits in a single unit cell wide layer, see Supplementary Fig. 14. Parameters used are energetic disorder 60 meV, lattice constant 1.8 nm, attempt to hop frequency 3×10^{14} s^{-1}, all typical for doped conjugated polymers[41].

The Seebeck coefficients (S) of the polymer combinations also show a similar trend as the two-dimensional conduction and sheet resistance values (Fig. 2d). Because of the high resistivity of

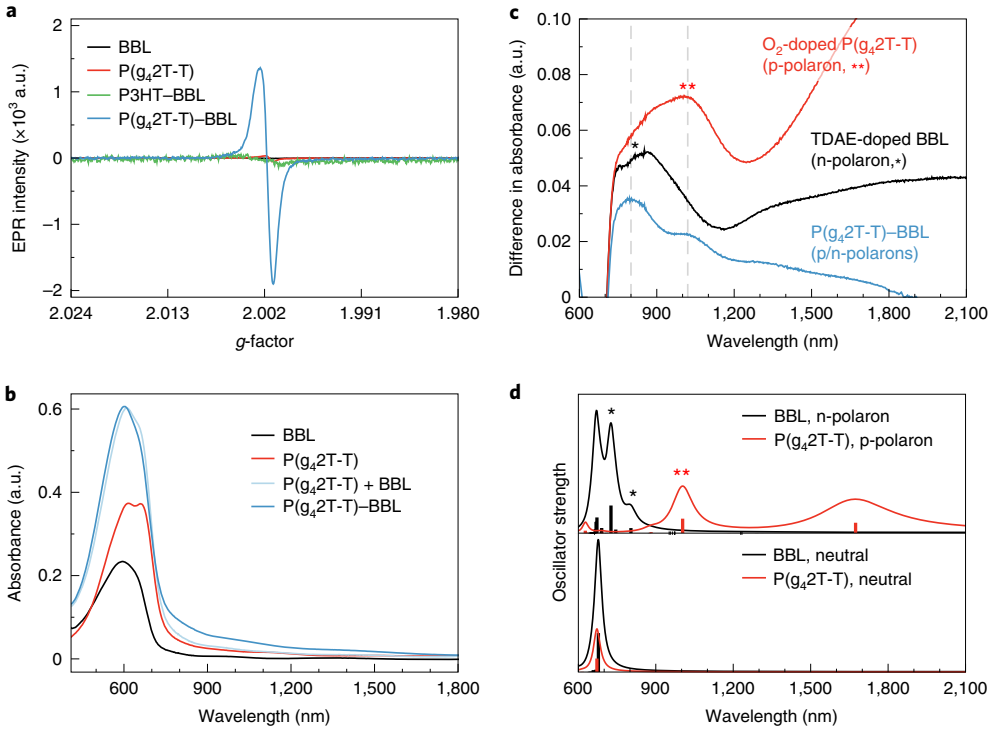

Fig. 4 | GSET confirmed by EPR and UV–vis–NIR spectroscopies. a, Volume-normalized EPR signal of all-polymer films, where a 2-nm-thick interfacial layer is assumed in the bilayer films, that is, 1 nm on either side of the interface. **b**, Absorption spectra of BBL, P($g_4$2T-T) and P($g_4$2T-T)–BBL films. **c**, Difference between the bilayer P($g_4$2T-T)–BBL and the sum of single P($g_4$2T-T) and BBL layer (P($g_4$2T-T) + BBL) absorptions, showing the polaron absorption in the bilayer, as well as difference between both TDAE-doped BBL and O_2-doped P($g_4$2T-T) layer and the relative non-doped layer absorptions, showing the n- and p-polaron spectra, respectively. **d**, DFT/TDDFT computed vertical transition energies and spectra for neutral species (bottom panel) and charged polaronic species (upper panel), for BBL and P($g_4$2T-T). TDDFT vertical energies are shifted by 0.4 eV, and spectra are computed as a Lorentzian convolution of transition energies with a full-width half-maximum of 0.1 eV.

the individual polymers, the thermovoltages of the pristine (non-conducting) materials cannot be measured reliably, but their absolute values are larger than 1,000 μV K^{-1}. When P($g_4$2T-T)–BBL and P($g_4$2T-TT)–BBL bilayers are formed, their Seebeck coefficients drop to -300 ± 48 and -343 ± 67 μV K^{-1}, respectively. These thermovoltage values are approximately half of those measured for P3HT–BBL (-625 ± 39 μV K^{-1}) and PBTTT–BBL (-612 ± 84 μV K^{-1}) bilayers, suggesting a higher charge density, which is consistent with the conductivity measurements. The negative Seebeck coefficients of the bilayer films also suggests that the conductivity is dominated by the n-type BBL.

It is of particular interest to also determine to which extent the hole channel contributes to the conduction. The conductivity and Seebeck coefficient of BBL and P($g_4$2T-T) change under oxygen exposure (Supplementary Fig. 13), an evolution that can consistently be interpreted in terms of a two-layer system composed of two parallel channels for electron and hole transport, respectively. On exposure to oxygen, an exponential decrease in conductivity is observed. This decrease is entirely dominated by a reduction in conductivity of the BBL phase (σ_{BBL}), such that the weight factor of the only linearly increasing S_{BBL} will diminish. This shifts the balance towards the positive $S_{P(g42T\text{-}T)}$, the weight factor of which will probably increase. As this process continues, the total thermovoltage changes sign and the resulting conductivity starts to increase again when the p-doping of P($g_4$2T-T) becomes large enough to compensate for the conductivity loss in BBL (see Supplementary Fig. 13 for further discussion).

To gain further insight into the fraction of charges that contribute to transport, we paired temperature-dependent resistance measurements with kinetic Monte Carlo (kMC) modelling. kMC simulations are a powerful tool to obtain detailed insight into charge and energy transport in disordered media[39–42]. Figure 3 shows the result of such simulations tailored to the description of GSET in a bilayer geometry. In short, the model describes the stochastic motion of discrete electrons and holes on a simple cubic lattice using Miller–Abrahams hopping rates. The simulation box includes the bilayer interface in the *xy* plane and is chosen sufficiently large to reach flat-band conditions at the boundaries at $z = 0$ and $z = 36$ nm. All Coulomb interactions between charge carriers are explicitly accounted for and updated after each hopping event. There are no traps or static charges, corresponding to for example dopant ions, in the simulations. For simplicity, equal disorder and hopping parameters are used for electrons and holes. The simulations indicate that the charges are confined to a narrow, essentially single unit cell wide bilayer with equal densities of electrons and holes (see the concentration profiles in Supplementary Fig. 14). The latter is a direct consequence of charge conservation and the nature of the electron transfer process. Despite their relative simplicity, the simulations also quasi-quantitatively reproduce the experimentally observed trends in sheet resistance (Fig. 3a) and activation energy (Fig. 3b) as a function of the vacuum level shift. Specifically, a simulated activation energy of ~100 meV (Supplementary Fig. 15) for vacuum level shifts around 0.5 eV agrees well with the values of 120 ± 15 meV measured for P($g_4$2T-T)–BBL interfaces. Note also that for smaller shifts of the vacuum level (<0.4 eV), the activation energy exceeds 150 meV, which is in agreement with the larger activation energies measured for P3HT–BBL and PBTTT–BBL systems. Likewise, the range of sheet resistances obtained in kMC simulations matches very well with the values in Fig. 2b, running from ~4 MΩ sq^{-1} for the most conductive bilayer

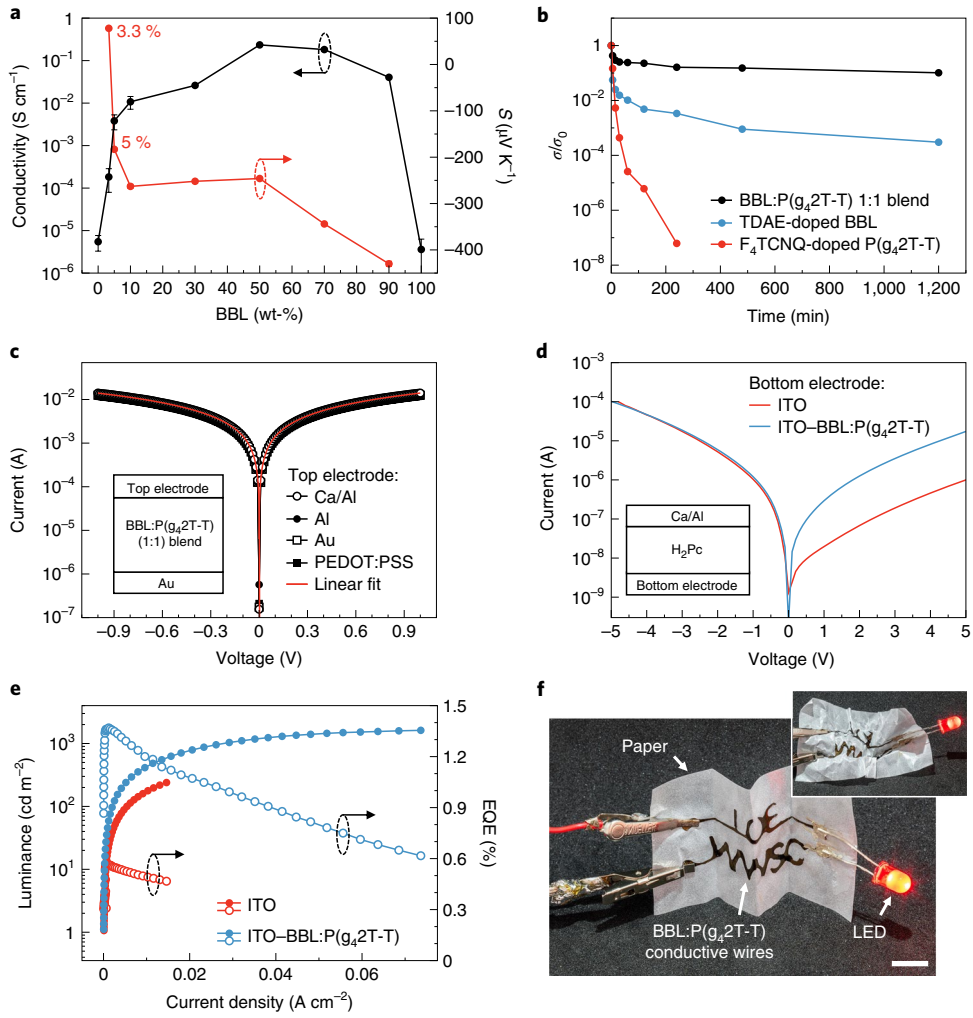

Fig. 5 | Electrical characterization of BBL:P(g$_4$2T-T) blend films. a, Conductivity and Seebeck coefficient of BBL:P(g$_4$2T-T) blend films at different BBL content; error bars represent standard deviation. **b**, Normalized electrical conductivity of P(g$_4$2T-T):BBL (1:1) blend, TDAE-doped BBL and F$_4$TCNQ-doped P(g$_4$2T-T) films on continuous thermal annealing at 200 °C for 20 h inside a N_2-filled glovebox. **c**, *I*–*V* characteristics of BBL:P(g$_4$2T-T) (1:1) BHJs sandwiched between Au and various metal electrodes with work functions ranging from 5.1 eV (PEDOT:PSS) to 2.8 eV (Ca/Al). **d**, *I*–*V* characteristics of a typical diode using ITO with and without BBL:P(g$_4$2T-T) (1:1) BHJs as the bottom electrode. **e**, Luminance and external quantum efficiency (EQE) as a function of current density for inverted OLEDs using ITO with and without BBL:P(g$_4$2T-T) (1:1) BHJs as the bottom electrode. **f**, Photograph of a folded paper circuit with BBL:P(g$_4$2T-T) BHJ conductive wires lighting up a LED. The paper circuit functions even after being aggressively crumpled. Scale bar, 8 mm.

(highest vacuum level shift), to ~500 MΩ sq^{-1} for the least conductive bilayer.

EPR spectroscopy was performed to confirm the existence of polarons in the bilayer films and to determine their density. All samples were sealed in EPR tubes inside a nitrogen-filled glovebox to avoid oxygen exposure. The volume-normalized EPR data are reported in Fig. 4a. Separate single-layer polymers show weak EPR signals (Supplementary Fig. 16 and Supplementary Table 1), whereas a stronger EPR signal intensity is observed for the P(g$_4$2T-T)–BBL and P(g$_4$2T-TT)–BBL bilayers, consistent with the presence of GSET-induced polarons that have a density of 4–5 × 10^{19} cm^{-3} (considering a 2-nm-thin interfacial layer as inferred from kMC simulations). This charge density corresponds well to the outcome of the kMC simulations reported above and with what is observed from impedance measurements (Supplementary Fig. 17), giving values of 7.5 × 10^{19} cm^{-3} for the P(g$_4$2T-T)–BBL sample. For comparison, P3HT–BBL bilayers only give a carrier density of 3.5 × 10^{18} cm^{-3}, which is in line with the roughly exponential relationship between vacuum level shift and charge carrier density predicted by kMC.

The absorption spectra of BBL, P(g$_4$2T-T) and P(g$_4$2T-T)–BBL, measured in nitrogen atmosphere, are shown in Fig. 4b,c together with the computed (density functional theory, DFT, and time-dependent DFT, TDDFT) vertical electronic transitions and spectra for the neutral and single charged states (polaron) of the corresponding oligomers shown in Fig. 4d. P(g$_4$2T-TT) and P(g$_4$2T-TT)–BBL absorption spectra are qualitatively similar to P(g$_4$2T-T) and P(g$_4$2T-T)–BBL, and for this reason are reported in Supplementary Fig. 18. The sum of the pristine BBL and P(g$_4$2T-T) absorptions matches the absorption of the bilayer film with respect to the π–π* transition regions of the individual polymers located around 600 nm (refs. [37,43]). The optical absorption of polaronic species formed in the bilayer sample was obtained by subtracting the sum of the pristine BBL and P(g$_4$2T-T) absorptions from the absorption of the P(g$_4$2T-T)–BBL bilayer and is given as the blue curve in Fig. 4c. The absorption of the polarons in the bilayer has two sub-bandgap peaks at 800 and 1,030 nm, respectively, with a minor absorption component extending into the mid-infrared region, along with a bleaching of the ground-state absorption at shorter wavelengths. These two

peaks originate from the negative (800 nm) and positive (1,030 nm) polarons (Supplementary Fig. 19). The energetics of the polarons are in agreement with the DFT/TDDFT computed spectra of electronically neutral and charged oligomer chains (Fig. 4d). For BBL, one intense transition is computed for the n-polaron species (negatively charged state, $q=-1$, doublet) and appears at around 800 nm (Fig. 4d)[44]. For both P($g_4$2T-T) and P($g_4$2T-TT) (see Supplementary Fig. 19c for the latter), two main intense transitions are computed for the p-polaron species (positive charged state, $q=1$, doublet), namely at about 1,000 nm and 1,600–1,700 nm. The n-polaron transition (800 nm) and the two p-polaron transitions (1,000 nm and 1,600–1,700 nm) match well with the observed polaron absorption bands in the bilayer structure. Details concerning the nature of the electronic transitions and the polarons' molecular structure are reported in the Supplementary Information.

Finally, we demonstrate GSET in D–A bulk heterojunctions (BHJs) by blending P($g_4$2T-T) with BBL in a common solvent. The resulting all-polymer D–A BHJs have appreciable conductivity without the need of heterogeneous dopants. The conductivity of the BHJ layer at different polymer weight ratios is reported in Fig. 5a. A BBL:P($g_4$2T-T) blend with 1:1 weight ratio shows the highest bulk conductivity of $0.23\pm0.02\,S\,cm^{-1}$, which is four to five orders of magnitude higher than that of the pure polymers. The Seebeck coefficient for these blends varies from $-430\,\mu V\,K^{-1}$ at 90 wt% BBL to $80\,\mu V\,K^{-1}$ at 3.3 wt% BBL, indicating that P($g_4$2T-T) starts to dominate the conduction only at very low BBL concentrations (Fig. 5a). A plateau in the Seebeck coefficient value at around $-260\,\mu V\,K^{-1}$ is found for BBL:P($g_4$2T-T) blend ratios ranging from 10 to 50 wt%, which is comparable to the thermovoltage of a bilayer made from the same material combination (Fig. 2d). A similar trend is observed for BBL:P($g_4$2T-TT) (Supplementary Fig. 20). This suggests that the interfacial regions at these compositions of the BHJ behave similarly to a bilayer, indicating that the balance of p- and n-transport of charge and energy is similar to the bilayer. Weakly diffracting domains with a typical phase-separation length scale of 40–60 nm are observed for 50–70 wt% BBL content (Supplementary Figs. 21 and 22). In the BHJ case, the larger interfacial area per unit volume not only increases the bulk conductivity but also affects the Seebeck coefficient. A maximum power factor of $2.2\pm0.2\,\mu W\,m^{-1}\,K^{-2}$ was obtained for the BHJs with a BBL content of 70 wt% (Supplementary Fig. 23), which is among the highest power factors reported for solution processed films of n-type polymers[45]. Since the thermopower values in the electron- and hole-carrying phases counteract each other, the measured high thermopower is not a trivial result. It reflects that, at least for the present material combination, at equal electron and hole densities, the electron charge and energy transport dominate over the hole transport[41]. The all-polymer D–A BHJs show also superior thermal stability as compared to the equivalent single polymer films doped by molecular dopants (Fig. 5b). The electrical conductivity of the BBL:P($g_4$2T-T) (1:1) blend decreases by less than one order of magnitude on continuous thermal annealing at 200 °C for 20 h, while for TDAE-doped BBL the conductivity drops by more than four orders of magnitude under the same stressing conditions. The conductivity of F_4TCNQ-doped P($g_4$2T-T) vanishes below detection limits after only 4 h of annealing at 200 °C, which we ascribe to sublimation of the dopant (Supplementary Fig. 24).

Last, we investigated the ability of all-polymer D–A BHJs to function as universal interface/transport layers. The BBL:P($g_4$2T-T) (1:1) blend forms an ohmic contact to various metal electrodes with work functions ranging from 5.1 eV (PEDOT:PSS) to 2.8 eV (Ca/Al), as indicated by the linear I–V characteristics shown in Fig. 5c. When coated onto ITO substrates, BBL:P($g_4$2T-T) BHJs can effectively inject electrons into a 100-nm-thick layer of phthalocyanine (H_2Pc, electron affinity of 2.7 eV), yielding a ten-fold higher current level as compared to identical devices with bare ITO electrodes (Fig. 5d). We then tested these all-polymer D–A BHJs as injecting electrodes in proof-of-concept OLEDs. Inverted OLEDs with BBL:P($g_4$2T-T)-coated ITO electrodes (see Methods for detailed information) yield a higher luminance and external quantum efficiency as compared to identical devices without BBL:P($g_4$2T-T) BHJs (Fig. 5e). Because of their appreciable conductivity and ability to make ohmic contacts, these all-polymer D–A BHJs can be printed on paper to form conductive lines and used to light up an inorganic LED, even after being crumpled (Fig. 5f).

In summary, we report GSET in all-polymer D–A heterojunctions. We find that placing low-ionization-energy conjugated polymers into contact with a high-electron-affinity counterpart enables the formation of conducting interfaces with resistivity values that are five to six orders of magnitude lower than those of the separate single-layer polymers. The increased electrical conductivity originates from two parallel quasi-two-dimensional electron and hole sheet distributions reaching a charge concentration per unit area of $\sim10^{13}\,cm^{-2}$. UPS, EPR and UV–vis–near infrared (–NIR) measurements, combined with DFT calculations and kMC simulations, reveal the formation of p/n-polarons induced by a spontaneous electron transfer at the D–A heterointerfaces. We further transferred the concept of GSET to three-dimensional all-polymer BHJs, displaying superior thermal stability as compared to the equivalent single polymer films doped by molecular dopants. We anticipate that our discovery of all-polymer GSET will have a similar effect as the discovery of excited state charge transfer in the field of OLEDs and OSCs. As no mobile dopant molecules are used to dope the system, we envisage that our findings will inspire the development of next-generation biocompatible conductors for bioelectronics and wearable (e-textile/e-skin) devices.

Online content

Any methods, additional references, Nature Research reporting summaries, source data, extended data, supplementary information, acknowledgements, peer review information; details of author contributions and competing interests; and statements of data and code availability are available at https://doi.org/10.1038/s41563-020-0618-7.

Received: 26 September 2019; Accepted: 17 January 2020;
Published online: 09 March 2020

References

1. Reineke, S., Thomschke, M., Lussem, B. & Leo, K. White organic light-emitting diodes: status and perspective. *Rev. Mod. Phys.* **85**, 1245–1293 (2013).
2. Peumans, P., Yakimov, A. & Forrest, S. R. Small molecular weight organic thin-film photodetectors and solar cells. *J. Appl. Phys.* **93**, 3693–3723 (2003).
3. Lussem, B. et al. Doped organic transistors. *Chem. Rev.* **116**, 13714–13751 (2016).
4. Bubnova, O. & Crispin, X. Towards polymer-based organic thermoelectric generators. *Energy Environ. Sci.* **5**, 9345–9362 (2012).
5. Walzer, K., Maennig, B., Pfeiffer, M. & Leo, K. Highly efficient organic devices based on electrically doped transport layers. *Chem. Rev.* **107**, 1233–1271 (2007).
6. Bubnova, O. et al. Semi-metallic polymers. *Nat. Mater.* **13**, 190–194 (2014).
7. Russ, B., Glaudell, A., Urban, J. J., Chabinyc, M. L. & Segalman, R. A. Organic thermoelectric materials for energy harvesting and temperature control. *Nat. Rev. Mater.* **1**, 16050 (2016).
8. Salzmann, I., Heimel, G., Oehzelt, M., Winkler, S. & Koch, N. Molecular electrical doping of organic semiconductors: fundamental mechanisms and emerging dopant design rules. *Acc. Chem. Res.* **49**, 370–378 (2016).
9. Rivnay, J. et al. Organic electrochemical transistors. *Nat. Rev. Mater.* **3**, 17086 (2018).
10. Sun, H. et al. Complementary logic circuits based on high-performance n-type organic electrochemical transistors. *Adv. Mater.* **30**, 1704916 (2018).
11. Nardes, A. M. et al. Microscopic understanding of the anisotropic conductivity of PEDOT: PSS thin films. *Adv. Mater.* **19**, 1196–1200 (2007).
12. Qiu, L. et al. Enhancing doping efficiency by improving host-dopant miscibility for fullerene-based n-type thermoelectrics. *J. Mater. Chem. A.* **5**, 21234–21241 (2017).
13. Pingel, P. & Neher, D. Comprehensive picture of p-type doping of P3HT with the molecular acceptor F4TCNQ. *Phys. Rev. B.* **87**, 115209 (2013).

14. Zuo, G., Abdalla, H. & Kemerink, M. Impact of doping on the density of states and the mobility in organic semiconductors. *Phys. Rev. B.* **93**, 235203 (2016).
15. Li, J. et al. Quantitative measurements of the temperature-dependent microscopic and macroscopic dynamics of a molecular dopant in a conjugated polymer. *Macromolecules* **50**, 5476–5489 (2017).
16. Li, J. et al. Measurement of small molecular dopant F4TCNQ and C60F36 diffusion in organic bilayer architectures. *ACS Appl. Mater. Interfaces* **7**, 28420–28428 (2015).
17. Hynynen, J. et al. Enhanced electrical conductivity of molecularly p-doped poly(3-hexylthiophene) through understanding the correlation with solid-state order. *Macromolecules* **50**, 8140–8148 (2017).
18. Jacobs, I. E. & Moulé, A. J. Controlling molecular doping in organic semiconductors. *Adv. Mater.* **29**, 1703063 (2017).
19. Kroon, R. et al. Polar side chains enhance processability, electrical conductivity, and thermal stability of a molecularly p-doped polythiophene. *Adv. Mater.* **29**, 1700930 (2017).
20. Reiser, P. et al. Dopant diffusion in sequentially doped poly(3-hexylthiophene) studied by infrared and photoelectron spectroscopy. *J. Phys. Chem. C.* **122**, 14518–14527 (2018).
21. Fahlman, M. et al. Interfaces in organic electronics. *Nat. Rev. Mater.* **4**, 627–650 (2019).
22. Alves, H., Molinari, A. S., Xie, H. X. & Morpurgo, A. F. Metallic conduction at organic charge-transfer interfaces. *Nat. Mater.* **7**, 574–580 (2008).
23. Odom, S. A. et al. Restoration of conductivity with TTF-TCNQ charge-transfer salts. *Adv. Funct. Mater.* **20**, 1721–1727 (2010).
24. Hiraoka, M. et al. On-Substrate synthesis of molecular conductor films and circuits. *Adv. Mater.* **19**, 3248–3251 (2007).
25. Jacobs, I. E. et al. Polymorphism controls the degree of charge transfer in a molecularly doped semiconducting polymer. *Mater. Horiz.* **5**, 655–660 (2018).
26. Jérome, D. Organic conductors: from charge density wave TTF–TCNQ to superconducting (TMTSF)2PF6. *Chem. Rev.* **104**, 5565–5592 (2004).
27. Chen, X. L. & Jenekhe, S. A. Bipolar conducting polymers: blends of p-type polypyrrole and an n-type ladder polymer. *Macromolecules* **30**, 1728–1733 (1997).
28. Grancini, G. et al. Hot exciton dissociation in polymer solar cells. *Nat. Mater.* **12**, 29–33 (2013).
29. Kawamura, Y., Yanagida, S. & Forrest, S. R. Energy transfer in polymer electrophosphorescent light emitting devices with single and multiple doped luminescent layers. *J. Appl. Phys.* **92**, 87–93 (2002).
30. Yoshida, H. Principle and application of low energy inverse photoemission spectroscopy: a new method for measuring unoccupied states of organic semiconductors. *J. Electron Spectrosc. Relat. Phenom.* **204**, 116–124 (2015).
31. Yoshida, H. Near-ultraviolet inverse photoemission spectroscopy using ultra-low energy electrons. *Chem. Phys. Lett.* **539-540**, 180–185 (2012).
32. Oehzelt, M., Koch, N. & Heimel, G. Organic semiconductor density of states controls the energy level alignment at electrode interfaces. *Nat. Commun.* **5**, 4174–4174 (2014).
33. Greiner, M. T. et al. Universal energy-level alignment of molecules on metal oxides. *Nat. Mater.* **11**, 76–81 (2012).
34. Bokdam, M., Çakır, D. & Brocks, G. Fermi level pinning by integer charge transfer at electrode-organic semiconductor interfaces. *Appl. Phys. Lett.* **98**, 113303–113303 (2011).
35. Braun, S., Salaneck, W. R. & Fahlman, M. Energy-level alignment at organic/metal and organic/organic interfaces. *Adv. Mater.* **21**, 1450–1472 (2009).
36. Bao, Q., Braun, S., Wang, C., Liu, X. & Fahlman, M. Interfaces of (ultra)thin polymer films in organic electronics. *Adv. Mater. Interfaces* **6**, 1800897 (2018).
37. Kiefer, D. et al. Double doping of conjugated polymers with monomer molecular dopants. *Nat. Mater.* **18**, 149–155 (2019).
38. Pasveer, W. F. et al. Unified description of charge-carrier mobilities in disordered semiconducting polymers. *Phys. Rev. Lett.* **94**, 206601 (2005).
39. Bässler, H. Charge transport in disordered organic photoconductors a Monte Carlo simulation study. *Phys. Status Solidi B.* **175**, 15–56 (1993).
40. Zuo, G., Abdalla, H. & Kemerink, M. Conjugated polymer blends for organic thermoelectrics. *Adv. Electron. Mater.* **5**, 1800821 (2019).
41. Zuo, G., Li, Z., Wang, E. & Kemerink, M. High seebeck coefficient and power factor in n-type organic thermoelectrics. *Adv. Electron. Mater.* **4**, 1700501 (2018).
42. Melianas, A. et al. Photo-generated carriers lose energy during extraction from polymer-fullerene solar cells. *Nat. Commun.* **6**, 8778 (2015).
43. Wang, S. et al. Thermoelectric properties of solution-processed n-doped ladder-type conducting polymers. *Adv. Mater.* **28**, 10764–10771 (2016).
44. Fazzi, D., Fabiano, S., Ruoko, T.-P., Meerholz, K. & Negri, F. Polarons in π-conjugated ladder-type polymers: a broken symmetry density functional description. *J. Mater. Chem. C.* **7**, 12876–12885 (2019).
45. Yao, C. J., Zhang, H. L. & Zhang, Q. Recent progress in thermoelectric materials based on conjugated polymers. *Polymers* **11**, 107 (2019).

Methods

Materials. High-molecular-weight BBL ($\eta = 11.6\,dl\,g^{-1}$ in methanesulfonic acid (MSA) at 30 °C, $M_w = 60.5$ kDa), was synthesized following the procedure reported previously[46]. P($g_4$2T-T) and P($g_4$2T-TT) were synthesized following the procedure reported in refs. [19,37]. RR-P3HT (Sigma-Aldrich), PBTTT-C14 (Merck Chemicals) and P3CPT (Sigma-Aldrich) were used as received.

Sample preparation. High-molecular-weight BBL was dissolved in MSA at room temperature at a concentration of 2 mg ml^{-1}. BBL films were fabricated by spin coating on glass at 3,000 r.p.m. for 1 min, immediately followed by immersion into (1) isopropanol and (2) deionized water to remove any residual MSA from the film, as confirmed by Fourier transform-infrared (FTIR) (Supplementary Fig. 25). P($g_4$2T-T) and P($g_4$2T-TT) were dissolved in anhydrous chloroform at a concentration of 5 mg ml^{-1} inside an N_2-filled glovebox, whereas P3HT and PBTTT were dissolved in anhydrous chlorobenzene at a concentration of 5 mg ml^{-1} inside the glovebox. Note that chloroform does not dissolve the underneath BBL layer (Supplementary Fig. 26). The PBTTT solution was heated on 150 °C hotplate before use to completely dissolve the polymer. The donor polymers were spin coated inside the glovebox at 1,000 r.p.m. for 1 min. The as-prepared films were thermally annealed on a hotplate at 120 °C for 0.5 h inside the glovebox. For preparation of the blend films, P($g_4$2T-T) was dissolved in MSA at a concentration of 2 mg ml^{-1} under an ambient environment, then blended with BBL solutions at different ratios, followed by stirring at ~200 r.p.m. (room temperature) for one night to allow proper mixing. The blend films were prepared by spin coating at 1,500–3,000 r.p.m. for 1 min to get a final film thickness of around 20 nm. Finally, the blend films were transferred to the glovebox and annealed on a hotplate at 120 °C for 20 min to get rid of residual MSA and oxygen in the film. A clear conductivity increase could be observed after the annealing process. For the metal–insulator–metal diodes, 30-nm-thick BBL:P($g_4$2T-T) (1:1) films were spin coated on top of prepatterned gold electrodes (3 nm Cr as adhesion layer). Top metal electrodes were thermally evaporated through a shadow mask, yielding a device with an active area of 0.25 mm^2. The PEDOT:PSS (Clevios PH1000) top electrode was spin coated on top of the BHJ films. Electron-only diodes were fabricated by evaporating H_2PC (100 nm) onto ITO and ITO coated with a 10-nm-thick BBL:P(g42T-T) (1:1) layer, followed by thermal evaporation of Ca (10 nm) and Al (100 nm) as the top electrode. The device area was 4 mm^2. Inverted OLEDs were fabricated by thermal evaporation and had the following structure: ITO (or ITO–BBL:P($g_4$2T-T) (1:1) (10 nm))/ 4,6-bis(3,5-di(pyridin-3-yl)phenyl)-2-methylpyrimidine (60 nm)/coumarin 545T doped in tris-(8-hydroxyquinoline)aluminium 3 wt% (20 nm)/*N*,*N*'-di(1-naphthyl)-*N*,*N*'-diphenyl-(1,1′-biphenyl)-4,4′-diamine (70 nm)/MoO_3 (5 nm)/Al. The device area was 8 mm^2. The paper circuit was fabricated by drop casting BBL:P($g_4$2T-T) (1:1) from MSA solution (8 mg ml^{-1}) on tracing papers through a shadow mask. The MSA was washed with deionized water and dried before use.

Electrical characterization. Electrical conductivity and the Seebeck coefficients were measured inside the glovebox using a semiconductor characterization system (Keithley 4200-SCS). For the conductivity measurements, prepatterned substrates were prepared by thermally evaporating 3 nm of chromium and 20 nm of gold on clean glass substrates with a shadow mask. The substrates had a channel length of 30 μm and a channel width of 1,000 μm was used. A pair of Peltier elements were used to provide a temperature difference for Seebeck coefficient measurements. For these measurements, a different shadow mask was used, with a channel length of 0.5 mm and a channel width of 15 mm. The temperature difference was monitored using thermocouples. Electrical characterization of the metal–insulator–metal and electron-only diodes was performed with Keithley 4200-SCS inside a nitrogen-filled glovebox. The OLED electrical characterization was carried out using a Keithley 2400 source meter, while spectra and brightness properties were measured with a HORIBA PR-650 SpectraScan, controlled by the Labview program.

UPS. UPS experiments were carried out using a Scienta ESCA 200 spectrometer in an ultrahigh vacuum (1×10^{-10} mbar) with a standard helium-discharge lamp with photon energy of 21.22 eV (He I). The total energy resolution of the UPS measurement was about 80 meV as estimated from the width of the Fermi level of clean gold foil. All spectra were collected at a photoelectron takeoff angle of 0° (normal emission) at room temperature. The work function of the films was extracted from the determination of the high binding-energy cutoff of the UPS spectrum by applying a bias of −3 V to the sample.

LEIPS. For the LEIPS measurements, high-molecular-weight BBL was spin coated at rates of 3,000 and 4,000 r.p.m. from a 2 mg ml^{-1} solution. Since the obtained electron affinities are sensitive to the film thickness, we examined two different films to confirm the results. The specimen was introduced into the vacuum chamber evacuated to 3×10^{-7} Pa. The details of the LEIPS apparatus are described elsewhere[47]. An electron beam was introduced to the sample surface and the emitted photons were observed by a photon detector consisting of a bandpass filter and photomultiplier (Hamamatsu R585s). The electron energy was swept in the range of 0–5 eV. The overall resolution was between 0.3 and 0.4 eV. No discernible change due to sample damage was observed. The vacuum level was obtained from the inflection point of the sample current.

EPR. Quantitative EPR experiments were performed at the Swedish Interdisciplinary Magnetic Resonance Centre at Linköping University, using a Bruker Elexsys E500 spectrometer operating at about 9.8 GHz (X-band). EPR spectra were recorded in dark at room temperature. The films were prepared by spin coating on quartz glass as mentioned previously, followed by annealing on a hotplate at 150 °C for 20 min. All samples were encapsulated in an EPR tube with photoactive glues inside a glovebox to avoid oxygen exposure.

Thin-film morphology characterization. Atomic force microscopy (Digital Instruments) was performed in tapping mode using a silicon cantilever having a spring constant of 40 N m^{-1}. Grazing-incidence wide-angle X-ray scattering measurements were performed at Beamline 8-ID-E[48] at the Advanced Photon Source at the Argonne National Laboratory. Samples were irradiated with a 10.9-keV X-ray beam at an incidence angle of 0.125–0.135° in a vacuum for two summed exposures of 2.5 s (totalling 5 s of exposure), and scattered X-rays were recorded by a Pilatus 1 M detector located 228.16 mm from the sample at two different heights. The collected images were then processed by using the GIXGUI[49] software written for MATLAB and combined to eliminate gaps due to rows of inactive pixels, which also demonstrated that scattering was not changed by the X-ray exposure. All the films used for grazing-incidence wide-angle X-ray scattering characterization had the same thickness of roughly 25 nm. The data with incident angle 0.135° was judged to have the best signal and was selected for further analysis. Transmission electron microscope (TEM) lamellas were prepared using a combined focused ion beam—scanning electron microscope (Tescan GAIA3, FEI Versa). A representative area was selected and an initial protective layer of Pt was deposited on top of the region using electron beam-induced deposition with an electron beam of 3 kV. This was followed by ion beam-induced deposition to further increase the thickness of the Pt protection layer using a 30 kV Ga^+ ion beam with a current of 153 pA. A lamella was subsequently milled out and lifted to a TEM half-grid[50]. TEM analysis was performed using a FEI Titan 80–300 operated in scanning TEM mode at 300 kV and a JEOL NeoARM200F-Mono 40–200 operated in scanning TEM mode at 60 and 200 kV acceleration voltages. Energy dispersive X-ray spectroscopy and electron energy-loss spectroscopy spectral images were acquired to study the spatial distribution oxygen and nitrogen. These signals carried information about the location of BBL and P($g_4$2T-T). The signal was accumulated over multiple scan cycles to reduce damage to the sample.

UV–vis–NIR and FTIR absorption spectroscopy. Absorption spectra of the films were measured using a UV–vis–NIR spectrophotometer (PerkinElmer Lambda 900) inside an airtight sample holder. The films were prepared on calcium fluoride windows by spin coating following this procedure. The FTIR spectra were measured in transmission mode inside an airtight sample holder with a Bruker Equinox 55 spectrometer averaging 200 scans with a resolution of 4 cm^{-1} and a zero-filling factor of 2.

Thermogravimetric analysis. Thermal stability measurements were performed by TGA with a Mettler Toledo TGA/DSC 3+ under a 20 ml min^{-1} nitrogen flow. A drying step was performed at 50 °C for 10 min, after which the weight loss of each sample was recorded from 25 to 600 °C with a scan rate of 10 °C min^{-1}.

First principles calculations. Oligomers of different lengths were considered. For the case of BBL, eight repeat units were considered. For the cases of P($g_4$2T-T) and P($g_4$2T-TT), three repeat units were computed. Each structure was optimized by using the hybrid range-separated-corrected DFT functional, namely ωB97X-D3, combined with double-zeta split valence polarized Pope's basis set 6–31G*. Neutral and charged (positive $q = +1$ and negative $q = -1$) electronic states were considered. Charged states (polarons) were initially described using the spin polarized unrestricted DFT (UDFT) approach. For each case, a wavefunction stability check was run using the broken-symmetry (BS)-UDFT scheme. If an instability in the wavefunction was found, both the electronic and nuclear structures were re-optimized following the BS-UDFT potential energy profile. For the case of BBL, an instability in the negatively charged state was found[43,44], while for P($g_4$2T-T) and P($g_4$2T-TT) the unrestricted DFT wavefunction does not show any broken-symmetry behaviour. Vertical transition energies were computed for both neutral (TDDFT method) and charged (TDUDFT) states. For BBL, TD-BS-UDFT method was applied. All calculations were performed with the program package Gaussian16 B.01 (ref. [51]).

Data availability

The authors declare that the main data supporting the findings of this study are available within the paper and its Supplementary Information files. Source data for Figs. 2–5 are provided with the paper.

References

46. Arnold, F. E. & Van Deusen, R. L. Preparation and properties of high molecular weight, soluble oxobenz[de]imidazobenzimidazoisoquinoline ladder polymer. *Macromolecules* **2**, 497–502 (1969).

47. Yoshida, H. Note: low energy inverse photoemission spectroscopy apparatus. *Rev. Sci. Instrum.* **85**, 016101 (2014).
48. Jiang, Z. et al. The dedicated high-resolution grazing-incidence X-ray scattering beamline 8-ID-E at the advanced photon source. *J. Synchrotron Radiat.* **19**, 627–636 (2012).
49. Jiang, Z. GIXSGUI: a MATLAB toolbox for grazing-incidence X-ray scattering data visualization and reduction, and indexing of buried three-dimensional periodic nanostructured films. *J. Appl. Crystallogr.* **48**, 917–926 (2015).
50. Pettersson, H., Nik, S., Weidow, J. & Olsson, E. A method for producing site-specific TEM specimens from low contrast materials with nanometer precision. *Microsc. Microanal.* **19**, 73–78 (2013).
51. Frisch, M. J. et al. Gaussian 16, Revision B.01 (Gaussian, Inc., 2016).

Acknowledgements

We thank C. Musumeci (Linköping University) for assistance with atomic force microscopy and S. Gustafsson (Chalmers) for assistance with TEM specimen preparation. This work was supported by the Knut and Alice Wallenberg foundation, VINNOVA (grant no. 2015-04859), the Swedish Research Council (grant agreement nos. 2016-03979, 2016-06146, 2016-05498, 2016-05990, 2018-03824), the Swedish Government Strategic Research Area in Materials Science on Functional Materials at Linköping University (Faculty Grant SFO Mat LiU no. 2009 00971), ÅForsk (18-313) and the European Research Council (ERC) under grant agreement no. 637624. We also thank the Chalmers Material Analysis Laboratory for their support of microscopes. T.P.R acknowledges funding from the Finnish Cultural Foundation and the Finnish Foundation for Technology Promotion. N.S. thanks the National Natural Science Foundation of China (grant no. 61805211). H.Y. acknowledges JST ALCA (JPMJAL1404) and the Futaba Foundation. Work at the University of Washington was supported by the National Science Foundation (DMR-1708450). D.F. acknowledges the Deutsche Forschungsgemeinschaft (DFG) for the grant 'Molecular Understanding of Thermo-Electric Properties in Organic Polymers (FA 1502/1-1)', and the Regional Computing Centre (RRZK) of Universität zu Köln, for providing computing time and resources on the HPC CHEOPS.

Author contributions

S.F. conceived, designed and supervised the project. H.S. initiated the study. K.X. and H.S. prepared the samples, performed the electrical measurements and analysed the data. T.P.R. recorded and analysed the UV–vis–NIR data. G.W. performed the grazing-incidence wide-angle X-ray scattering and atomic force microscopy measurements. R.K. synthesized P($g_4$2T-T) and P($g_4$2T-TT). N.B.K. synthesized BBL, under S.A.J.'s supervision. Y.P. and W.M.C. performed and analysed the EPR data. X.L. and M.F. recorded and analysed the UPS spectra. D.F. performed the DFT calculations. K.S. and H.Y. performed and analysed the LEIPS data. C.Y.Y fabricated and tested the paper circuits. N.S. fabricated and tested the OLEDs. G.P., A.B.Y. and E.O. performed and analysed TEM. M.K. performed the kMC simulations. K.X., H.S., M.K., C.M. and S.F. wrote the manuscript. All authors contributed to discussion and manuscript preparation.

Competing interests

The authors declare no competing interests.

Additional information

Supplementary information is available for this paper at https://doi.org/10.1038/s41563-020-0618-7.

Correspondence and requests for materials should be addressed to H.S., M.B. or S.F.

Reprints and permissions information is available at www.nature.com/reprints.

Paper III

Experimentally Calibrated Kinetic Monte Carlo Model Reproduces Organic Solar Cell Current–Voltage Curve

Sebastian Wilken, Tanvi Upreti, Armantas Melianas, Staffan Dahlström, Gustav Persson, Eva Olsson, Ronald Österbacka, and Martijn Kemerink

Solar RRL , 2020, 2000029

Solar RRL
www.solar-rrl.com

Experimentally Calibrated Kinetic Monte Carlo Model Reproduces Organic Solar Cell Current–Voltage Curve

Sebastian Wilken, Tanvi Upreti, Armantas Melianas, Staffan Dahlström, Gustav Persson, Eva Olsson, Ronald Österbacka, and Martijn Kemerink*

Kinetic Monte Carlo (KMC) simulations are a powerful tool to study the dynamics of charge carriers in organic photovoltaics. However, the key characteristic of any photovoltaic device, its current–voltage (*J–V*) curve under solar illumination, has proven challenging to simulate using KMC. The main challenges arise from the presence of injecting contacts and the importance of charge recombination when the internal electric field is low, i.e., close to open-circuit conditions. Herein, an experimentally calibrated KMC model is presented that can fully predict the *J–V* curve of a disordered organic solar cell. It is shown that it is crucial to make experimentally justified assumptions on the injection barriers, the blend morphology, and the kinetics of the charge transfer state involved in geminate and nongeminate recombination. All of these properties are independently calibrated using charge extraction, electron microscopy, and transient absorption measurements, respectively. Clear evidence is provided that the conclusions drawn from microscopic and transient KMC modeling are indeed relevant for real operating organic solar cell devices.

1. Introduction

Kinetic Monte Carlo (KMC) simulations have successfully been used to model the charge carrier dynamics in organic photovoltaics (OPVs) on the ps to μs timescale. For instance, it was shown that in thin-film OPV devices, thermalization in the disorder-broadened density of states (DOS) does not complete before charges are extracted.[1–4] The conclusions from these studies are drawn from the fitting of time-resolved experiments performed under certain bias conditions such as short circuit or open circuit. Other authors used KMC modeling to focus on the process of charge recombination and its dependence on the morphology in slabs of material, i.e., in absence of contacts.[5–9] However, it is still an open question to which extent nonequilibrium phenomena and other aspects that are not accounted for in macroscopic simulations, such as quasi-equilibrium drift–diffusion (DD) models, govern the steady-state operation of complete OPV devices. To answer the question, it would be highly desirable to have a microscopic model that is also able to describe the current–voltage (*J–V*) curve, particularly the open-circuit voltage (V_{OC}) and the fill factor.

Modeling *J–V* curves with KMC has so far proven nearly impossible. One of the main challenges is the presence of two injecting contacts. While it may be acceptable to consider the contacts as simple sinks for electrons and holes in transient extraction experiments (performed at $V \ll V_{OC}$), this simplification does not work for situations closer to V_{OC}. When the internal field is low, contacts inject many charge carriers into the active layer. This high carrier density is demanding from the computational point of view and challenging to correctly account for. Even though a few concepts exist how contacts can be implemented in KMC, literature studies have so far failed to fully describe *J–V* data of real devices or are based on assumptions that are not justified experimentally.[10–12]

Besides computational challenges, the injected charge density also sets the boundary conditions for the recombination of photogenerated carriers.[13] Charge recombination generally becomes more important when going from short circuit to open circuit because transport will slow down. Indeed, the competition between charge extraction and recombination has been demonstrated to be the main determinant of the device fill factor.[14–16] For a device model to be reliable, it must therefore capture the

Dr. S. Wilken, S. Dahlström, Prof. R. Österbacka
Department of Physics, Faculty of Science and Engineering
Åbo Akademi University
Porthansgatan 3, 20500 Turku, Finland
E-mail: sebastian.wilken@abo.fi

The ORCID identification number(s) for the author(s) of this article can be found under https://doi.org/10.1002/solr.202000029.

DOI: 10.1002/solr.202000029

Dr. S. Wilken, T. Upreti, Prof. M. Kemerink
Department of Physics, Chemistry and Biology
Linköping University
581 83 Linköping, Sweden

Dr. A. Melianas
Department of Materials Science and Engineering
Stanford University
Stanford, CA 94305, USA

G. Persson, Prof. E. Olsson
Department of Physics
Chalmers University of Technology
412 96 Göteborg, Sweden

hopping transport characteristics and the recombination kinetics at the same time. Even though the mechanisms of charge recombination are highly disputed, it is commonly accepted that the morphology plays a key role.[6,17,18] For instance, it is well documented that aggregated donor or acceptor domains may lower the recombination rate.[19–22] However, although the morphology of many donor/acceptor blends is well characterized by electron microscopy and other techniques, the nanostructure is often neglected in KMC and an effective medium is assumed instead.[23]

Here, we present a KMC model that successfully predicts device *J*–*V* curves while simultaneously accounting for nonequilibrium hopping transport and recombination dynamics. We show that this is only possible when correct assumptions are made on the injection barriers, the morphology of the active layer, and the charge recombination rate. All these properties are calibrated by independent experimental techniques such as charge extraction, electron microscopy, and transient absorption. We are thereby introducing a device model that works on a multitude of length and time scales. As such it will be useful for future investigations on the interplay between elementary processes and device characteristics of organic solar cells and other optoelectronic devices.

2. Results and Discussion

2.1. Material System

The aim of this work is to develop and experimentally calibrate a KMC model that fits both transient experiments and device *J*–*V* curves. Our material system for experimental calibration is TQ1:$PC_{71}BM$,[24] an archetypal polymer/fullerene blend. The reason for choosing TQ1:$PC_{71}BM$ is that for this specific system a clear picture of the carrier dynamics has emerged from time-resolved measurements and previous modeling, which is summarized in a recent review article.[23] Hence, many of the parameters for the KMC model are already known; in particular, it has been shown that the charge extraction in thin devices with an active-layer thickness around 100 nm is strongly affected by nonequilibrium effects. **Figure 1** shows the experimental *J*–*V* curve of a 72 nm-thick TQ1:$PC_{71}BM$ solar cell under simulated sunlight. The device displays an open-circuit voltage of 835 mV, a short-circuit current of 86 A m^{-2}, a fill factor of 0.63, and an efficiency of 4.5%.

2.2. KMC Describes Device Current–Voltage Curve

The KMC model, which is extended and experimentally calibrated in this work to fully describe OPV devices, has been introduced previously.[1,3] Briefly, it implements the extended Gaussian disorder model on a simple cubic lattice and takes into account: excitons; charge transfer (CT) pairs; electrons and holes; morphology via the allocation of individual hopping sites to different material phases; charge injection/extraction by hopping from/to the Fermi level of the respective contact; full Coulomb interactions, including those by image charges in the electrodes; periodic boundary conditions in the lateral directions.

Charge transport is described in terms of the Miller–Abrahams model, in which the hopping rate ν_{ij} from site i to site j separated by a distance r_{ij} is given by

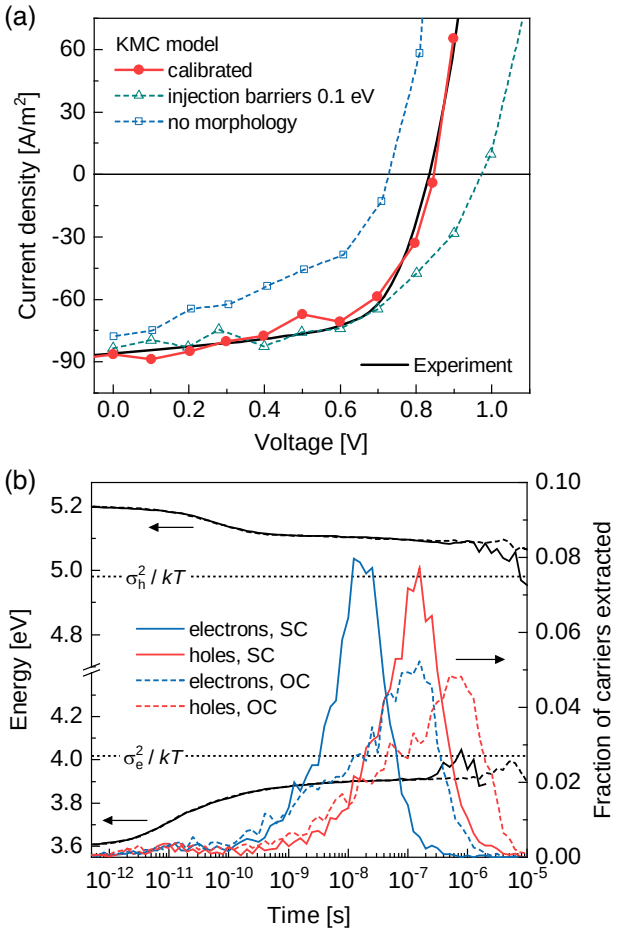

Figure 1. Key results of the KMC model described in this work. a) Experimental and simulated *J*–*V* curves of a TQ1:$PC_{71}BM$ solar cell (active-layer thickness: 72 nm) with the device architecture ITO/PEDOT:PSS/TQ1:$PC_{71}BM$/LiF/Al under simulated sunlight. Filled circles refer to the calibrated KMC model with the input parameters shown in Table 1. Open symbols are simulations with the same parameter set, but assuming too low injection barriers of 0.1 eV (triangles) or only an effective medium without $PC_{71}BM$ aggregates (squares). b) Simulated relaxation (black lines, left axis) and extraction time distributions (colored lines, right axis) of photogenerated charges under steady-state illumination at short circuit (SC, solid lines) and open circuit (OC, dashed lines) using the calibrated KMC model. Both electrons and holes are extracted before they reach their quasi-equilibrium energy (dotted lines).

$$\nu_{ij} = \nu_0 \exp(-2\alpha r_{ij}) \begin{cases} \exp\left(-\frac{\Delta E_{ij}}{kT}\right) & \Delta E_{ij} > 0 \\ 1 & \Delta E_{ij} \leq 0 \end{cases} \quad (1)$$

where ν_0 is the attempt-to-hop frequency, α is the inverse localization length, $\Delta E_{ij} = E_j - E_i$ is the energy difference between the sites, and kT is the thermal energy. Hopping is assumed to take place in a Gaussian DOS

$$g(E) = \frac{1}{\sqrt{2\pi\sigma^2}} \exp\left[-\frac{(E - E_0)^2}{2\sigma^2}\right] \quad (2)$$

where E is the single particle energy, E_0 is the mean energy, and σ is the width of the Gaussian DOS or the energetic disorder.

We note that without of loss of generality, also other energy distributions could be assumed in the model, such as an exponential DOS. From previous studies, however, it is known that a Gaussian DOS gives the most appropriate description for the present TQ1:$PC_{71}BM$ system both when describing transient and steady-state experiments.[23,25] In this work, only hopping between nearest neighbors on a regular, sixfold coordinated lattice was considered. In this configuration, the localization length α is unimportant; the first exponential term of Equation (1) was implicitly included in ν_0, that is, the rate of downward nearest-neighbor hops.

The core working principle of a KMC model is to simulate the time evolution of a system based on the transition rates of all possible events (here hops, generation, recombination, injection). The event that occurs at a certain point in time is randomly selected with the transition rates used as weighting factors. The time step between single events is calculated as $\tau = -\ln(u)/\Sigma_\nu$, where u is a random number drawn from a homogeneous distribution between 0 and 1, and Σ_ν is the sum of the rates of all possible events. A typical simulation starts with a number of photogenerated excitons. The excitons may separate into CT pairs/free charges or recombine after their lifetime. Diffusion of excitons by Förster and Dexter energy transfer is both accounted for. An additional on-site barrier of 0.8 eV is used to facilitate charge separation in molecularly mixed phases. Further details on the used KMC algorithm can be found in the Supporting Information of ref. [3].

As mentioned earlier, the presence of injecting contacts causes computational challenges. Charge injection is mediated by the injection barriers, i.e., the energy offset between the contact Fermi level and the respective molecular orbital of the semiconductor. Especially for low barriers, carriers may oscillate multiple times across the contact interface before injection/extraction finally takes place. We mitigated this "small barrier" problem by only allowing for a transfer if the number of charges next to the contact interface deviates from its equilibrium value. The transfer is modeled as hopping event with an attempt frequency $\nu_{0,\mathrm{cont}}$ of the same order as for the transport of the faster carrier (here electrons) in the semiconductor. This ensures that charge collection is not limited by the contacts. Both the cathode and anode were considered nonselective; hence, possible losses due to diffusion of carriers into the "wrong" contact are implicitly accounted for.

An advantage of KMC simulations is that no explicit assumptions about the formalism of charge recombination need to be made. Recombination of free charges involves the formation of a CT pair as intermediate. Exciton formation is explicitly allowed, but requires overcoming the relevant energy-level offset between the TQ1 and $PC_{71}BM$; as such, it can be interpreted as the inverse of charge separation, i.e., the splitting of (CT) excitons into free electrons and holes. As discussed in more detail later, it is then the inverse lifetime of the CT state that determines the recombination rate and must be calibrated experimentally.

The filled circles in Figure 1a show that after the calibration discussed later, the KMC model fits the J–V curve of the TQ1:$PC_{71}BM$ solar cell well within experimental accuracy and matches both the device V_{OC} and fill factor. **Table 1** shows the key parameters used for the simulations. We note that these values are not the result of a fitting routine but come from independent characterizations. The hopping parameters were chosen in such a way that they represent earlier experiments, such as time-resolved electric-field-induced second harmonic generation (TREFISH)[4] and temperature-dependent space-charge-limited currents (SCLC),[4,26] but at the same time allow efficient calculations. This was done by assuming a single disorder for electrons and holes ($\sigma_\mathrm{e} = \sigma_\mathrm{h} \equiv \sigma$) and adjusting the attempt frequencies ν_0 such that the macroscopic transport characteristics of TQ1:$PC_{71}BM$, e.g., the contrast between electron and hole mobility, are still captured (see Supporting Information for details). Figure 1b shows that also with the symmetrized hopping parameters, relaxation in the DOS is far from being complete when photogenerated carriers are extracted. This is true for both short-circuit and open-circuit conditions, which indicates that nonequilibrium effects may affect charge extraction along the entire J–V curve. A detailed discussion of how the nonequilibrium effects influence the individual performance parameters will be the topic of another publication.

Table 1. Key parameters used in the calibrated KMC model.

Parameter	Value
Simulated volume [sites]	$40 \times 40 \times 40$
Nearest neighbor distance, a_{NN} [nm]	1.8
Energetic disorder electrons, σ_e [meV]	75
Attempt-to-hop frequency electrons, $\nu_{0,\mathrm{e}}$ [s^{-1}]	1×10^{11}
Energetic disorder holes, σ_h [meV]	75
Attempt-to-hop frequency holes, $\nu_{0,\mathrm{h}}$ [s^{-1}]	1×10^{10}
Inverse exciton lifetime, k_{exc} [s^{-1}]	1×10^{9}
Inverse CT state lifetime, k_{CT} [s^{-1}]	3×10^{7}
Injection barrier height [eV]	0.2
Contact attempt-to-hop frequency, $\nu_{0,\mathrm{cont}}$ [s^{-1}]	1×10^{11}

The main result of this study is that a KMC model that can describe full J–V characteristics requires an appropriate description and calibration of the injection barriers and the morphology in the active layer. If wrong or too simple assumptions are made on these properties, our otherwise well-validated KMC model can no longer describe the device (Figure 1a, open symbols). Because this mainly concerns V_{OC} and the fill factor, these observations are closely related to the charge recombination. In the following sections we will therefore focus on the factors that determine the shape of the J–V curves in the fourth quadrant, that is, the injection barrier height, the blend morphology, and the recombination rate.

2.3. Calibration of Injection Barriers

The injection barriers set the carrier density in the device around the built-in voltage. To get a realistic estimate of the barrier height, we compare the results of charge extraction experiments in the dark with device simulations. As KMC calculations are computationally too expensive for this approach, we used a DD model instead.[27,28] This is justified because the charges treated here were not photogenerated, but injected from the contacts, so that the complexities of exciton/charge separation are bypassed. Furthermore, charges are injected from thermalized reservoirs (contacts), so that it is reasonable to describe them

by a quasi-equilibrium mobility. The mobility values were estimated by inserting the hopping parameters in Table 1 in the mobility functional by Pasveer et al.[29] Charge recombination is assumed to be strictly bimolecular with the steady-state recombination coefficient ($6 \times 10^{-18} m^3 s^{-1}$) taken from experimental studies on TQ1:$PC_{71}BM$.[30,31]

Figure 2a shows the effect of the injection barrier height on the average carrier density. Here, we chose devices with an active-layer thickness of 150 nm; only at these larger thicknesses a "bulk" region is established, which makes the comparison with charge-extraction experiments more reliable.[32,33] Note that especially at higher densities the carrier profiles are not perfectly symmetric, which is due to the imbalanced electron and hole transport.[28,34] The experiments to be simulated are charge extraction by linearly increasing voltage (CELIV) and bias-assisted charge extraction (BACE). In both techniques, the device is held at a certain pre-bias (V_{pre}) until a steady state is reached; the charges in the device are then extracted by applying a triangular (CELIV) or rectangular (BACE) voltage pulse. The dark carrier density is calculated from the transient current $J(t)$ via

$$n_{dark} = \frac{1}{qd}\int_0^{t_f} [J(t) - J_0(t)]dt \quad (3)$$

where q is the elementary charge, d is the active-layer thickness, J_0 is the displacement current measured at $V_{pre} = 0$, and t_f is the time at which charge extraction is completed. Note that in the form of Equation (3), the carrier density represents the average of electrons and holes, as pointed out by Hawks et al.[35]

Figure 2b shows that CELIV and BACE give a consistent picture of the carrier density as a function of voltage. At $V_{pre} = 0.9$ V, which approximately corresponds to open-circuit conditions under 1 sun illumination, n_{dark} is about 1×10^{22} m^{-3}. This is the same order of magnitude as for the photogenerated carrier density and indicates the importance of injected carriers for charge recombination. As can be seen, the best description of the dark carrier density and its voltage dependence is obtained for a barrier height of 0.2 eV; with this value, the KMC model reproduces the experimental J–V curve (see Figure 1). We note that the discrepancy between CELIV/BACE and DD simulation at voltages well below the built-in voltage is merely due to experimental limitations. In this regime, most carriers are situated in the thin space-charge regions close to the contacts, which makes them only partly visible to charge-extraction experiments.[14,36]

If instead too small injection barriers are selected as input for the KMC model, it can no longer describe both V_{OC} and the fill factor. The open triangles in Figure 1 show this for a barrier height of 0.1 eV. Although it is not pursued further in this work, we would like to stress that this finding shows that defining a contact as "Ohmic," in the sense that it does not limit injection and extraction in a particular experiment, is insufficient. Here, injection barriers of 0.1 and 0.2 eV both give rise to "Ohmic" injection, implying bulk-limited transport under forward bias, but these barriers are not equivalent in terms of the resulting photovoltaic behavior.

Another interesting observation is that, as one would expect, lowering the injection barriers from 0.2 to 0.1 eV leads to an increase in V_{OC}. But at the same time the fill factor becomes reduced, so that the overall power conversion efficiency stays roughly the same. Hence, we can deduce from our KMC simulations that reducing the injection barriers does not per se lead to a better performing solar cell device. Closer examination of this aspect, however, requires more extensive parameter studies, which are beyond the scope of the present article and will be the subject of future work.

2.4. Morphology Governs Charge Recombination

In our previous KMC studies, the photoactive blend was assumed as an effective hopping medium without any morphological features.[1,3,4] This zero-order approximation is reasonable when describing experiments on the ps to μs timescale where charge recombination is insignificant. However, we find that the effective-medium approach fails to fully describe the device J–V curve (Figure 1, open squares). To obtain a more realistic

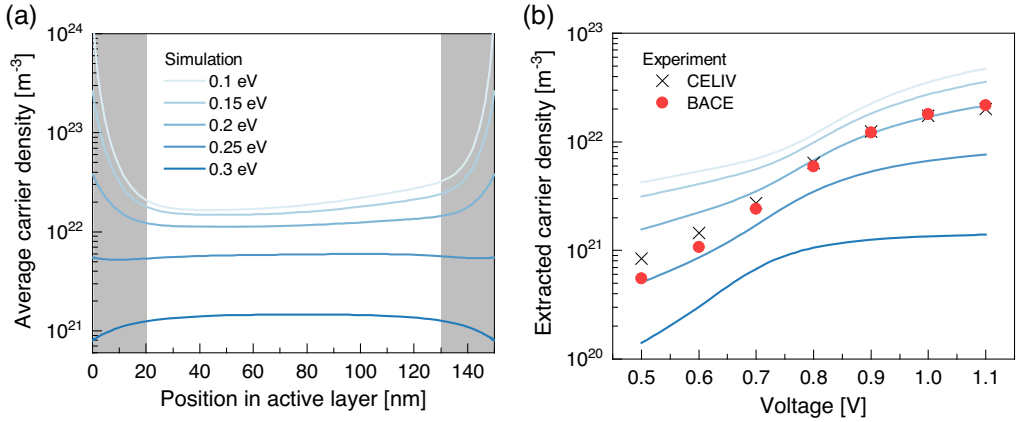

Figure 2. Calibration of the injection barrier height. a) Spatial carrier density profiles at a forward bias of 0.9 V for different barriers at the anode and cathode. Data refer to the average of the electron and hole density calculated with a DD model. Gray shaded areas mark the space-charge regions close to the contact interfaces. b) Extracted carrier density according to Equation (3) from CELIV and BACE experiments on a 150 nm-thick TQ1:$PC_{71}BM$ solar cell (symbols). The voltage axis refers to the bias V_{pre} present before charges were extracted by the reverse voltage pulse. Colored traces are the prediction from DD calculations using the same injection barrier heights as in panel (a).

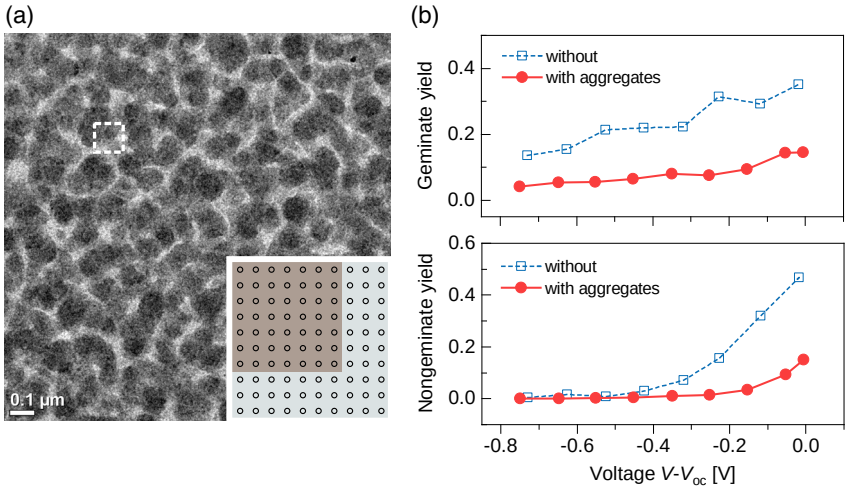

Figure 3. Impact of morphology on charge recombination. a) BF-TEM image of a TQ1:$PC_{71}BM$ blend film and numerical implementation of the morphology (inset). See the Supporting Information for a HDAAF-STEM image of the same sample. The relevant structure are $PC_{71}BM$ aggregates, which are assumed in the KMC model as 7×7 inclusions in a 10×10 unit cell representing the mixed phase of TQ1 and $PC_{71}BM$. In vertical direction, the aggregates are assumed to be extended throughout the whole thickness. The dashed square shows a region that is reasonably captured by this model morphology. b) Impact of the aggregates on the simulated yield of geminate and nongeminate recombination between short-circuit and open-circuit conditions.

picture of the morphology, we performed transmission electron microscopy (TEM). **Figure 3**a shows a representative bright-field (BF) TEM image of a TQ1:$PC_{71}BM$ blend that was prepared the same way as for device fabrication. The image displays a granular structure with clusters of dark contrast of about 100 nm in size. Dark regions in BF-TEM images of polymer/fullerene blends are commonly attributed to fullerene domains because of their higher density. However, this assignment is not unambiguous; the different intensities could also be caused by phase contrast due to local crystallinity differences. For comparison, we investigated the same sample in scanning transmission electron microscopy (STEM) mode using a high-angle annular dark field (HAADF) detector.[37,38] In the Supporting Information we show that HAADF-STEM reveals very similar structures as in Figure 3a, but of inverted contrast. This clearly confirms that the clusters seen in TEM are $PC_{71}BM$ aggregates, in agreement with earlier work on similar blend systems.[39]

The main effect of aggregation is to reduce the energy gap between the highest occupied molecular orbital (HOMO) and the lowest unoccupied molecular orbital (LUMO) compared with the amorphous material. This creates an energy cascade with a driving force for carriers to move from the (molecularly mixed) amorphous regions toward the (material-pure) aggregates and will affect the way how charges separate and recombine.[19–22] We implemented the aggregates in the KMC model as 7×7 inclusions in a 10×10 unit cell describing the mixed donor/acceptor phase (Figure 3a, inset). Inclusions were assumed to consist of pure $PC_{71}BM$ with a 0.2 eV lower-lying LUMO compared with the mixed phase; all other properties were left unchanged to keep the number of unknown parameters at a minimum. We did not consider pure TQ1 domains, as our TEM experiments do not provide any evidence for them. This is reasonable because TQ1 is a relatively amorphous polymer that has no strong tendency to form aggregates, in particular in blends with excess fullerene.[40]

Note that the aggregate size in the KMC model is smaller than what is suggested from the electron microscopy images. This was done to keep the simulation box computationally tractable while still getting reasonable statistics. The size of the inclusions and the unit cell were chosen such that the donor/acceptor ratio of the blend is maintained. A detailed examination of the structure size on the device performance is beyond the scope of this work; however, first tests indicate that the actual size of the aggregates is much less important than their presence. Likewise, a 0.1 eV lower-lying LUMO for the aggregate phase did not make any relevant difference as compared with the used 0.2 eV.

Only with the inclusions in the effective hopping medium we were able to match the fill factor of the experimental devices. Figure 3b shows that this is due to a reduction of the charge recombination. Importantly, the presence of aggregates simultaneously reduces the yields of geminate and nongeminate recombination. This confirms earlier suggestions that the generation and recombination of free charges are coupled via the ability of CT pairs to separate.[41,42] In other words, the possibility for carriers (here electrons) to lower their energy by moving to the aggregates will not only increase the charge separation yield, but also reduce the nongeminate recombination. This is a clear hint that the different ability to form aggregates/phase-pure domains may explain why different OPV materials show so different recombination rates compared with the Langevin model. In the context of this work, however, it means that it is the kinetics of the CT states, i.e., how they dissociate and (re-)associate, that must be calibrated experimentally.

2.5. Calibration of the Recombination Rate

The inset in **Figure 4** shows the kinetic model of charge recombination that has emerged from the literature.[2,19,30,41,42] As we discuss to some detail in the Supporting Information,

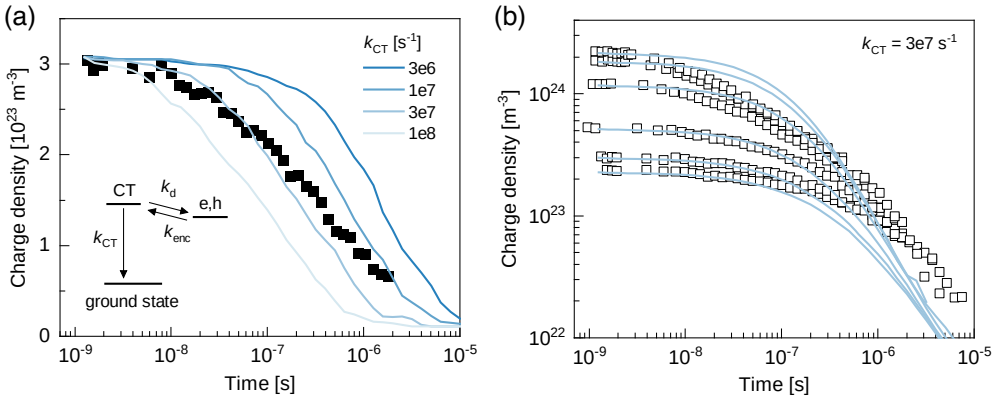

Figure 4. Comparison between experimental (symbols) and modeled (lines) transient absorption of TQ1:$PC_{71}BM$ blends. a) Attempts to model the experiment with a pump fluency of 4×10^{16} photons $\cdot$ m^{-2} with the parameters shown in Table 1 but varied decay rate of CT states into the ground state. Inset: Illustration of the relevant states and transitions for charge recombination. b) Measurements with various initial carrier densities by varying the pump fluency from 2.5×10^{16} to 6×10^{17} photons $\cdot$ m^{-2} and simulations for a fixed decay rate of $k_{CT} = 3 \times 10^7 s^{-1}$. Experimental data from Andersson et al.[43]

recombination in TQ1:$PC_{71}BM$ is not limited by the rate k_{enc} at which free carriers meet to form an interfacial CT complex. This implies that the probability for the CT pair to dissociate is much higher than to decay to the ground state ($k_d \gg k_{CT}$). It has been shown that in such a situation an equilibrium between CT states and free charge carriers is established.[2,41] The position of the equilibrium is determined by the rate k_{CT}, which is the relevant parameter in the KMC model to calibrate the recombination.

To do so, we use the results of transient absorption (TA) experiments. TA is a pump-probe technique that optically tracks a carrier population created by a short light pulse over time. As the experiment is carried out under flat-band conditions, the measured decay solely reflects the recombination kinetics. Figure 4a shows the TA decay of a TQ1:$PC_{71}BM$ device for a pump fluency of 4×10^{16} photons $\cdot$ m^{-2} taken from the literature.[43] The traces are attempts to describe the experiment with our KMC model. One can clearly see that the (inverse) CT state lifetime is the crucial parameter for the decay dynamics. The best fit on short time scales is obtained for $k_{CT} = 3 \times 10^7 s^{-1}$. Figure 4b shows that with the calibrated value for k_{CT}, we are able to reasonably describe transient absorption data for a range of initial carrier densities.

On longer time scales, however, the fit between TA experiment and KMC model is not as good. The reason for this is the symmetrized transport parameters we use for computational effectiveness. As discussed in the Supporting Information, the disorder σ and attempt-to-hop frequency ν_0 are largely interchangeable, i.e., increasing the one parameter can be compensated by decreasing the other and vice versa. This interchangeability allows us to use the values shown in Table 1, which keep the KMC calculations manageable while still reproducing the measured quasi-steady-state mobilities. Nevertheless, using symmetrized transport parameters remains a simplification, so that some of the details necessary to describe the full TA traces are lost. In Figure S2, Supporting Information, we show that a better fit can be obtained when the "real," nonsymmetrized values for σ and ν_0 are used in the simulation. However, significant differences between the parameter sets are only noticeable at very high initial carrier densities ($\approx 10^{24} m^{-3}$) and on the time scale of μs and beyond. At those times, most of the carriers have already been extracted, as can be seen from the histograms in Figure 3b and from previous experiments.[1,4,23] Hence, the use of the simplified transport parameters is well justified when describing a solar cell under standard operating conditions.

3. Conclusions

We have presented a KMC model that fully describes the *J*–*V* curve of a disordered organic solar cell under solar illumination. The agreement between experiment and simulation is obtained by experimentally calibrating the injections barriers, the blend morphology, and the dynamics of the CT state involved in charge recombination. Our work clearly highlights the importance of contacts for a KMC model to describe operating OPVs. We find that seemingly small changes in the injection barrier height can have major impact on the device V_{OC} and fill factor. This confirms that injected charges play a key role in the apparent recombination mechanism. Furthermore, we find charge recombination to be limited by the fate of the intermediate CT exciton, which can be influenced by the presence of aggregates in the active layer, and not by the transport of electrons and holes; our results indicate that the energy difference between the aggregated and mixed regions and the aggregate size is not that important, but the presence of aggregates is.

The platform introduced in this work will be useful for future studies on properties of OPV materials that are not accessible via macroscopic, quasi-equilibrium modeling techniques such as DD. Questions to be answered include, but are not limited to, how nonequilibrium effects affect the device operation and what the critical morphological factors are that determine the charge recombination. Finally, we point out that our results give strong support that the conclusions derived from previous transient KMC studies are also relevant for OPVs under standard operating conditions.

4. Experimental Section

Device Fabrication: Binary solution of poly[[2,3-bis(3-octyloxyphenyl)-5,8-quinoxalinediyl]-2,5-thiophenediyl] (TQ1) and [6,6]-phenyl-C_{71}-butyric acid methyl ester ($PC_{71}BM$) in weight ratio 1:2.5 was prepared in chlorobenzene to a total concentration of 25 mg mL^{-1}. The device structure was ITO/PEDOT:PSS (30 nm)/TQ1:$PC_{71}BM$ (72 nm)/LiF (0.6 nm)/Al (90 nm). ITO-coated glass substrates were boiled in a 5:1:1 mixture (by volume) of deionized water, ammonium hydroxide (25%), and hydrogen peroxide (28%) at 80 °C for 15 min for cleaning. PEDOT:PSS (Baytron P VP Al 4083) was spin-coated onto the ITO glasses at 3000 rpm for 40 s, followed by annealing at 150 °C for 10 min. The active layer was spin-coated at 500 rpm for 60 s. The LiF/Al top electrode was deposited by thermal evaporation through a shadow mask to get an active area of 0.05 cm^2.

Electrical Measurements: Current–voltage curves were recorded with a Keithley 2401 source measure unit under standard AM1.5G illumination (100 mW cm^{-2}) using an Oriel LSH-7320 solar simulator. Dark charge extraction measurements were performed using a pulse generator (SRS DG 535) and a function generator (SRS DS 345) for applying the extraction voltage pulse and an oscilloscope (Tektronix TDS 680B) for recording the current transient. Devices were mounted in a vacuum cryostat kept at room temperature. The measurement setup was controlled from a computer using a LabVIEW program. In the CELIV experiments, a steady-state voltage V_{pre} was applied in forward bias of the solar cell and a linearly increasing extraction pulse $V(t) = -At$ with $A = 0.05\,\mathrm{V\,\mu s^{-1}}$ and a total pulse length of 50 µs was used for charge extraction. For the BACE measurements, the same V_{pre} as used in the CELIV measurements was applied and charges were extracted using a rectangular voltage pulse with an amplitude 2.5 V and a pulse length of 50 µs.

Electron Microscopy: Samples for TEM were prepared by floating off TQ1:$PC_{71}BM$ films from PEDOT:PSS-coated glass substrates in deionized water. This was followed by picking up the films directly on TEM copper mesh grids for imaging. BF-TEM images were taken at an acceleration voltage of 200 kV in a FEI Tecnai T20 instrument. HAADF-STEM images were taken at an acceleration voltage of 300 kV in a FEI Titan 80-300.

Supporting Information

Supporting Information is available from the Wiley Online Library or from the author.

Acknowledgements

This project has received funding through European Union's Horizon 2020 research and innovation programme under the Marie Skłodowska-Curie grant agreement no. 799801 ("ReMorphOPV"). T.U., G.P., and E.O. acknowledges funding by Vetenskapsrådet (project "OPV2.0"). A.M. acknowledges support from the Knut and Alice Wallenberg Foundation (KAW 2016.0494) for Postdoctoral Research at Stanford University. S.D. and R.Ö. acknowledge financial support from the Jane & Aatos Erkko foundation (project "ASPIRE"). G.P. and E.O. thank the Chalmers Material Analysis Laboratory for their support of microscopes.

Conflict of Interest

The authors declare no conflict of interest.

Keywords

charge injection, charge recombination, kinetic Monte Carlo simulations, organic photovoltaics, morphology

Received: January 15, 2020
Revised: April 10, 2020
Published online:

[1] A. Melianas, V. Pranculis, A. Devižis, V. Gulbinas, O. Inganäs, M. Kemerink, *Adv. Funct. Mater.* **2014**, *24*, 4507.
[2] I. A. Howard, F. Etzold, F. Laquai, M. Kemerink, *Adv. Energy Mater.* **2014**, *4*, 1301743.
[3] A. Melianas, F. Etzold, T. J. Savenije, F. Laquai, O. Inganäs, M. Kemerink, *Nat. Commun.* **2015**, *6*, 8778.
[4] A. Melianas, V. Pranculis, Y. Xia, N. Felekidis, O. Inganäs, V. Gulbinas, M. Kemerink, *Adv. Energy Mater.* **2017**, *7*, 1602143.
[5] B. P. Lyons, N. Clarke, C. Groves, *Energy Environ. Sci.* **2012**, *5*, 7657.
[6] M. C. Heiber, C. Baumbach, V. Dyakonov, C. Deibel, *Phys. Rev. Lett.* **2015**, *114*, 136602.
[7] C. Groves, N. C. Greenham, *Phys. Rev. B* **2008**, *78*, 155205.
[8] V. Coropceanu, J. L. Brédas, S. Mehraeen, *J. Phys. Chem. C* **2017**, *121*, 24954.
[9] W. Kaiser, A. Gagliardi, *J. Phys. Chem. Lett.* **2019**, *10*, 6097.
[10] L. Meng, Y. Shang, Q. Li, Y. Li, X. Zhan, Z. Shuai, R. G. E. Kimber, A. B. Walker, *J. Phys. Chem. B* **2010**, *114*, 36.
[11] L. Meng, D. Wang, Q. Li, Y. Yi, J. L. Brédas, Z. Shuai, *J. Chem. Phys.* **2011**, *134*, 124102.
[12] D. Kipp, V. Ganesan, *J. Appl. Phys.* **2013**, *113*, 234502.
[13] U. Würfel, L. Perdigón-Toro, J. Kurpiers, C. M. Wolff, P. Caprioglio, J. J. Rech, J. Zhu, X. Zhan, W. You, S. Shoaee, D. Neher, M. Stolterfoht, *J. Phys. Chem. Lett.* **2019**, *10*, 3473.
[14] D. Neher, J. Kniepert, A. Elimelech, L. J. A. Koster, *Sci. Rep.* **2016**, *6*, 24861.
[15] D. Bartesaghi, I. Del Carmen Pérez, J. Kniepert, S. Roland, M. Turbiez, D. Neher, L. J. A. Koster, *Nat. Commun.* **2015**, *6*, 7083.
[16] P. Kaienburg, U. Rau, T. Kirchartz, *Phys. Rev. Appl.* **2016**, *6*, 024001.
[17] C. Göhler, A. Wagenpfahl, C. Deibel, *Adv. Electron. Mater.* **2018**, *4*, 1700505.
[18] G. Lakhwani, A. Rao, R. H. Friend, *Annu. Rev. Phys. Chem.* **2014**, *65*, 557.
[19] T. M. Burke, M. D. McGehee, *Adv. Mater.* **2014**, *26*, 1923.
[20] F. C. Jamieson, E. B. Domingo, T. McCarthy-Ward, M. Heeney, N. Stingelin, J. R. Durrant, *Chem. Sci.* **2012**, *3*, 485.
[21] S. Sweetnam, K. R. Graham, G. O. Ngongang Ndjawa, T. Heumüller, J. A. Bartelt, T. M. Burke, W. Li, W. You, A. Amassian, M. D. McGehee, *J. Am. Chem. Soc.* **2014**, *136*, 14078.
[22] D. P. McMahon, D. L. Cheung, A. Troisi, *J. Phys. Chem. Lett.* **2011**, *2*, 2737.
[23] A. Melianas, M. Kemerink, *Adv. Mater.* **2019**, 1806004.
[24] E. Wang, L. Hou, Z. Wang, S. Hellström, F. Zhang, O. Inganäs, M. R. Andersson, *Adv. Mater.* **2010**, *22*, 5240.
[25] A. Melianas, N. Felekidis, Y. Puttisong, S. C. J. Meskers, O. Inganäs, W. M. Chen, M. Kemerink, *Proc. Natl. Acad. Sci. USA* **2019**, *116*, 23416.
[26] T. Upreti, Y. Wang, H. Zhang, D. Scheunemann, F. Gao, M. Kemerink, *Phys. Rev. Appl.* **2019**, *12*, 064039.
[27] M. Burgelman, P. Nollet, S. Degrave, *Thin Solid Films* **2000**, *361–362*, 527.
[28] S. Wilken, O. J. Sandberg, D. Scheunemann, R. Österbacka, *Sol. RRL* **2020**, *4*, 1900505.
[29] W. F. Pasveer, J. Cottaar, C. Tanase, R. Coehoorn, P. A. Bobbert, P. W. M. Blom, D. M. de Leeuw, M. A. J. Michels, *Phys. Rev. Lett.* **2005**, *94*, 206601.
[30] D. H. K. Murthy, A. Melianas, Z. Tang, G. Juška, K. Arlauskas, F. Zhang, L. D. A. Siebbeles, O. Inganäs, T. J. Savenije, *Adv. Funct. Mater.* **2013**, *23*, 4262.

[31] S. Roland, J. Kniepert, J. A. Love, V. Negi, F. Liu, P. Bobbert, A. Melianas, M. Kemerink, A. Hofacker, D. Neher, *J. Phys. Chem. Lett.* **2019**, *10*, 1374.
[32] T. Kirchartz, J. Nelson, *Phys. Rev. B* **2012**, *86*, 165201.
[33] F. Deledalle, P. S. Tuladhar, J. Nelson, J. R. Durrant, T. Kirchartz, *J. Phys. Chem. C* **2014**, *118*, 8837.
[34] D. Scheunemann, S. Wilken, O. J. Sandberg, R. Österbacka, M. Schiek, *Phys. Rev. Appl.* **2019**, *11*, 054090.
[35] S. A. Hawks, B. Y. Finck, B. J. Schwartz, *Phys. Rev. Appl.* **2015**, *3*, 044014.
[36] J. Kniepert, I. Lange, N. J. van der Kaap, L. J. A. Koster, D. Neher, *Adv. Energy Mater.* **2014**, *4*, 1301401.
[37] J. Loos, E. Sourty, K. Lu, G. de With, S. van Bavel, *Macromolecules* **2009**, *42*, 2581.
[38] A. Alekseev, G. J. Hedley, A. Al-Afeef, O. A. Ageev, I. D. W. Samuel, *J. Mater. Chem. A* **2015**, *3*, 8706.
[39] O. Bäcke, C. Lindqvist, A. D. de Zerio Mendaza, S. Gustafsson, E. Wang, M. R. Andersson, C. Müller, E. Olsson, *Nanoscale* **2015**, *7*, 8451.
[40] E. Wang, J. Bergqvist, K. Vandewal, Z. Ma, L. Hou, A. Lundin, S. Himmelberger, A. Salleo, C. Müller, O. Inganäs, F. Zhang, M. Andersson, *Adv. Energy Mater.* **2013**, *3*, 806.
[41] T. M. Burke, S. Sweetnam, K. Vandewal, M. D. McGehee, *Adv. Energy Mater.* **2015**, *5*, 1500123.
[42] S. Shoaee, A. Armin, M. Stolterfoht, S. M. Hosseini, J. Kurpiers, D. Neher, *Sol. RRL* **2019**, *3*, 1900184.
[43] L. M. Andersson, A. Melianas, Y. Infahasaeng, Z. Tang, A. Yartsev, O. Inganäs, V. Sundström, *J. Phys. Chem. Lett.* **2013**, *4*, 2069.

Paper IV

Visualisation of individual dopant molecules in organic electronics: sub-nanometre 3D distribution and correlation to electronic properties

Gustav Persson, Emmy Järsvall, Magnus Röding, Yadong Zhang, Stephen Barlow, Seth Marder, Christian Müller, Eva Olsson

In manuscript

Visualisation of individual dopant molecules in organic electronics: sub-nanometre 3D distribution and correlation to electronic properties†

Gustav Persson,[a] Emmy Järsvall,[b] Magnus Röding,[c,d] Yadong Zhang,[e] Stephen Barlow,[e] Seth Marder,[e] Christian Müller [b] and Eva Olsson [a*]

Keywords: Visualisation, 3D, molecular dopant, organic semiconductor, nanostructure, concentration, clustering, electron tomography, structure-property correlation

Abstract

Molecular doping is of key importance for the performance enhancement of organic electronic devices. Despite this importance, little is known about the spatial distribution of these dopants, especially at molecular length scales. A homogenous distribution is often assumed when simulating transport properties of these materials, even though the distribution is known to be inhomogeneous. In this study, electron tomography is used to determine the position of individual dopant molecules and their three-dimensional distribution in a semiconducting polymer at the sub-nanometre scale. This enables the visualisation of the spatial distribution of the molecules. A heterogenous distribution is observed and its characteristics depend on the dopant concentrations. At low dopant concentrations, the majority of the dopant molecules are present as individual molecules or form clusters consisting of up to five molecules. At higher dopant concentrations, the dopants form larger nanoclusters with elongated shapes. Even in clusters, each individual dopant is still accessible to the surrounding polymer. A decrease in electrical conductivity is observed for the highly doped samples despite the lack of formation of large aggregates. The decreased conductivity is instead attributed to the increased energetic disorder and lower probability of charge transfer that originates from the increased size and the larger spread of dopant cluster size. This study highlights the importance of detailed information concerning the dopant spatial distribution at the sub-nanometre scale in three dimensions when designing organic electronic devices. The information acquired using this method can be used for more accurate simulations of transport properties of doped organic semiconductors.

[a]Department of Physics, Chalmers University of Technology, 41296 Göteborg, Sweden. Email: eva.olsson@chalmers.se
[b]Department of Chemistry and Chemical Engineering, Chalmers University of Technology, 41296 Göteborg, Sweden
[c]RISE Research Institutes of Sweden, Biomaterials and Health, Agriculture and Food, 41276 Göteborg, Sweden
[d]Department of Mathematical Sciences, Chalmers University of Technology, 41296 Göteborg, Sweden
[e]School of Chemistry and Biochemistry and Center for Organic Photonics and Electronics, Georgia Institute of Technology, Atlanta, GA 30332-0400, USA
†Electronic Supplementary Information (ESI) available. See DOI:

Introduction

Molecular doping enables control of the conductivity of organic semiconductors. Doping is used to enhance the performance of organic electronics utilising the advantageous aspects of efficient processing, light weight and mechanical flexibility of the organic semiconductors[1-3]. Due to intense research activities considerable progress has been made in recent years and the performance of organic electronics is approaching that of their inorganic counterparts, such as for solar cells, light-emitting diodes and thermoelectric generators[4-8]. The dopants allow the adjustment of energy levels and tuning of the conductivity in a range of several orders of magnitude[9]. However, crucial aspects of mechanims of doping including the charge transfer between dopant and the polymer, separation of the electron-hole pair and mobility of the charges are still not fully understood[10]. Control of the position of individual dopants with respect to other dopants and also the surrounding polymer are crucial aspects[11].

It has been repeatedly argued that the structural details of the fine-scale distribution of dopants affect the organic semiconductor performance[12-17]. At dopant concentrations of a few mol% the conductivity increases with increasing concentrations and the increase in conductivity can be several orders of magnitude. The relationship between dopant concentration and conductivity changes at higher concentrations where the increase in conductivity is decelerated and eventually the conductivity may start to decrease. It has been suggested that the decrease may be due to aggregation of the dopants giving rise to a disruption of the organic semiconductor nanostructure[18,19]. There is, however, no direct evidence that such aggregates block dopants from being adjacent to the host organic semiconductor since it is challenging to determine the position of the dopants in these systems[20]. It should also be noted that a homogenous distribution of dopants is typically assumed in simulation models for electrical transport properties[21]. A recent study has shown that modelling using experimental data about the detailed nanostructure of organic semiconductors can significantly improve the accuracy of the simulations[22]. Among the challenges for the determining the spatial distribution of dopant molecules are the small dimensions of the molecules, which are commonly less than 1 nm[3 23].

In this study we determine and visualise the position of individual dopant molecules of $Mo(tfd\text{-}COCF_3)_3$ in a semiconducting polymer of p($g_4$2T-T) (molecular structures shown in ESI Fig. S1). The distribution of the dopants is studied as a function of dopant concentration. The distance between the dopants is of the order of a few nanometres. Considering the importance of the location of each individual dopant we have performed electron tomography with sub-nanometre resolution to quantitatively determine the spatial distribution in three dimensions. Attention is paid to the position of the individual dopant molecules, their position with respect to other dopants and also with respct to the surrounding polymer. A gradual change in distribution is observed where individual molecules and clusters of few dopants are dominating at low concentrations. As the dopant concentration increases, the dopants form larger clusters. It is important to note that even though the cluster sizes increase, each individual dopant is still positioned adjacent to the surrounding polymer due to the elongated morphology of the clusters. The structural observations are correlated to UV-Vis-NIR absorption spectroscopy and conductivity data. It is concluded that the changes in dopant distribution and cluster morphology, as a function

of concentration, change the probability of charge transfer between the dopants and polymer due to increased energetic disorder at high dopant concentrations.

Experimental

Materials

p($g_4$2T-T) (M_n= 24 kg mol^{-1}, PDI = 3.3) and Mo(tfd-$COCF_3$)$_3$, were prepared according to previously reported procedures[24, 25]. Poly(diallyldimethylammonium chloride) (PDADMAC, Mw=400-500 kg mol^{-1}, 20 wt.% in H_2O) and anhydrous acetonitrile (AcN, purity >99.8 %) were purchased from Sigma Aldrich. Chloroform ($CHCl_3$, purity >99.8 %) was obtained from Fisher Scientific. All commercial solvents were used as received and without further purification.

Sample preparation

Thin films were prepared by co-processing p($g_4$2T-T) and Mo(tfd-$COCF_3$)$_3$. Stock solutions were prepared by dissolving p($g_4$2T-T) and Mo(tfd-$COCF_3$)$_3$ in AcN:$CHCl_3$ (1:1, v:v) to concentrations of 10 g L^{-1} and 4 g L^{-1} respectively. The co-processed solutions where prepared by adding appropriate volumes of AcN:$CHCl_3$ (1:1, v:v) to the p($g_4$2T-T) solutions before addition of the Mo(tfd-$COCF_3$)$_3$ solution to maintain a polymer concentration of 1 g L^{-1} (TEM) and 3 g L^{-1} (optical spectroscopy) in each polymer:dopant solution while varying the concentration of Mo(tfd-$COCF_3$)$_3$. The concentrations were based on calculations of molar percentages of the molar mass of the polymer repeat unit and the molar mass of the dopant.

Samples for TEM analysis were prepared by spin casting (1000 rpm, 500 rpms^{-1}, 40 s) an initial layer of PDADMAC (diluted to 1 wt% in MiliQ H_2O) onto microscope glass, followed by spin casting of the polymer:dopant solution. This yielded polymer:dopant film thickness of 10-20 nm. The TEM samples were immersed in MilliQ water resulting in the dissolution of the PDADMAC layer and the p($g_4$2T-T):Mo(tfd-$COCF_3$)$_3$ films subsequently floated to the surface. 400 Cu mesh TEM grids (TED Pella) were used to extract the films. To ensure complete solvent evaporation, the films were stored in a dry and dark environment.

Thin films for optical and electrical characterisation were prepared by spin casting the p($g_4$2T-T):Mo(tfd-$COCF_3$)$_3$ solution onto microscope glass, yielding a film thickness of 40-90 nm.

Scanning Transmission Electron Microscopy imaging

Analysis using scanning transmission electron microscopy (STEM) was performed on a spherical aberration corrected FEI Titan 80-300 at an acceleration voltage of 300 kV. High-angle annular dark field (HAADF) signal was used to form the images.

Tomography reconstructions and analysis

Tilt series for electron tomography were acquired with the software Xplore 3D. The tilt series used a Saxton scheme for angles $\pm 70°$ with a step of 2.5° at 0° angle, for a total of 79 images per tilt series. Reconstructions were done using the software IMOD. The series were aligned using cross-correlation, and the simultaneous iterative reconstruction tomography (SIRT) algorithm (run for 25 iterations) was used to reconstruct the volumes. The final reconstructions were visualised using the software Visualizer-evo. 3D meshes representing the dopant clusters were created by applying intensity thresholds on the reconstructions. The threshold values for each sample were optimised relative to each other by keeping a

ratio of 5:20:40 dopant voxels for the 5 mol%, 20 mol% and 40 mol% samples. A red colour in the volumes was chosen to represent the position of the dopant molecule and a slightly lower intensity threshold was added as a semi-transparent yellow colour to the figures to represent potential wobble of dopant side groups during acquisition of the tilt series. Position of individual dopant molecules were fit to data by adding correctly sized markers to the reconstructions.

Quantitative image analysis

The reconstructed volumes were all cropped to in-plane size 150 nm x 150 nm. The thickness of each cropped volume was selected independently for the three samples, based on a manual estimate of the film thickness from the image data. The image data were segmented (separating clusters and background) by Gaussian smoothing ($\sigma = 0.5$ voxels) and thresholding, followed by another Gaussian smoothing ($\sigma = 0.5$ voxels) and a final thresholding. The threshold values were selected to ensure that the volume fractions of identified dopant clusters adhered to the ratio 5:20:40 to accurately reflect the relative amount of dopant in the samples. The second iteration of smoothing and thresholding helped to reduce noise in the segmentation.

Individual clusters were identified, keeping only the clusters with 3 voxels (approximately the volume of a single molecule) or more. Three different characteristics were computed from the clusters: Volume, aspect ratio, and nearest neighbour distance. The volume was computed in a straightforward manner from the volume of a single voxel. The aspect ratio was computed by approximating the cluster with an ellipsoid having the same second moments as the cluster itself, defining the aspect ratio as the ratio of the major and the minor axes. The nearest neighbour distance is simply the Euclidean distance to the nearest cluster based on centroid coordinates. To account for the finite size of the volume, mirror boundary conditions were used in the latter case.

The analysis was implemented using the software Matlab.

UV-Vis-NIR absorption spectroscopy

Measurements were performed with a PerkinElmer Lambda 1050 spectrometer.

Electrical characterisation

The electrical resistivity was measured with a four-point probe setup from Jandel Engineering (cylindrical probe head, RM3000) using collinear tungsten carbide electrodes with equidistant spacing of 1 mm that were held down with a constant weight of 60 g. The electrical conductivity (σ) was then calculated according to $\sigma = \left((V/I)kt\right)^{-1}$ where V is the voltage, I is the current, k = 4.53 is a geometrical correction factor and t is the thickness.

Results and discussions

Structural Analysis

Figs. 1a-c show HAADF-STEM images of the films with 5, 20 and 40 mol% dopant concentrations. All images show bright areas on a darker continuous background. The HAADF-STEM imaging technique provides Z-contrast where the intensity increases with Z-number[26]. The bright areas in Figs. 1a-c thus correspond to regions with higher Z-number. The average Z-number of the dopant Mo(tfd-$COCF_3$)$_3$ is 20.0 while the corresponding Z-number of the the surrounding polymer p($g_4$2T-T) is 7.7. The brighter areas therefore show the position of the doped regions. The appearance of the three films is similar in these two-dimensional projection images showing a relatively even distribution of the bright areas in the polymer. The next step is to determine the 3D structure of the films, the size and the 3D morphology of the individual dopant regions.

Electron tomography was performed for the three different dopant levels, see Figs. 1d-f. Care was taken to obtain sufficient spatial resolution in the 3D reconstructions to resolve individual dopant molecules in the films. A voxel size of 0.5 nm was chosen for all reconstructions, which is smaller than the size of one dopant molecule, approximately 1.2 nm along the long axis and 0.6 nm along the short axis[25]. The red intensity areas in Figs. 1d-f represent the positions of dopant molecules. The yellow colour represents a slightly lower intensity value. Regions showing the yellow intensity interval is seen surrounding the dopant molecule volumes with red intensity. The yellow regions can be interpreted to be due to small movements of the dopant side chains during the acquistion of the tilt series. Videos of rotating reconstructed volumes are included in ESI Video S1-3 where inspection from all angles is provided. For each sample, a volume equivalent to an in-plane area of 2 600 μm^2 is reconstructed and analysed to ensure that the observations are representative of the films. A significant difference in nanostructure of the three films is evident in the 3D reconstructions. The data shows the presence of both isolated individual dopant molecules as well as clusters of dopant molecules. The size of the clusters increases with increasing dopant level. In addition, the distance between the clusters decreases with increasing dopant level.

Representative sub-volumes are shown in Figs. 2a-c where indivdual dopant molecules both when present as isolated molecules in the polymer or in clusters are clearly observed. Figs. 2d-f show volumes with markers for the position of the individual dopants. Spherical markers with diameters corresponding to the largest dimension of the dopant molecule indicate the 3D position of each molecule in the reconstructed clusters in the sub-volumes. There is a trend of increasing size of the dopant clusters with increasing dopant concentrations. In the film with 5 mol% the dopants are present either as isolated molecules or in clusters of only a few molecules. The clusters start to form elongated chains as the concentration increases.

The dopant positions were marked manually in 50 clusters for each sample to determine the average number of molecules per cluster. The dopant size distributions are shown in ESI Fig. S2. The average number of dopants per cluster is determined to be 3.4, 4.6 and 11 for 5 mol%, 20 mol% and 40 mol%, respectively. This is a quantitative confirmation of the visual impression of the effect of concentration on the cluster size distributions obtained from the

data in Fig. 2. The next step was to further refine the statistical analysis. An analysis was performed using the software Matlab to quantitatively characterise the clusters from the reconstructed data volumes of all clusters in larger volumes from each sample. The average cluster volumes were estimated to be 1.71 nm^3, 2.96 nm^3 and 3.10 nm^3 for the specimens, further confirming the gradual increase in cluster volume with increasing dopant concentrations. Fig. 3a show histograms of the distribution of cluster volumes at different doping levels that were determined from the data analysis. These histograms show that besides larger average volumes anomalous larger clusters sizes appeared at high doping concentrations with a few clusters having volumes up to 15 nm^3.

In addition to the trend of increasing cluster volume, the reconstructions show a change in cluster morphology. At 5 mol%, the typical clusters have a rounded shape. This appearance changes to an increasingly elongated shape at higher dopant levels, with a preference for elongation out of the film plane. This structural change was quantified by measuring the aspect ratio of the clusters. The results of the data analysis is shown in the aspect ratio histograms in Fig. 3b. Examples of dopant conformations for different aspect ratios are also illustrated in the figure. The histograms exhibit multiple peaks, especially for the higher dopant concentrations, indicating that some dopant conformations may be more frequent compared to others. The average cluster aspect ratio for 5 mol% is 2.1, which is close to the aspect ratio of single dopant molecules. A general trend of higher average aspect ratio and wider aspect-ratio distribution are evident for the higher dopant concentrations. This is consistent with the elongated shapes visible in the reconstructions in Figs. 1d-f. Dopant clusters that are elongated in the out of plane direction of the films have been reported before by Donhauser et al.[27], who visualised such clusters after doping the organic compound 4,4'-bis(N-carbazolyl)-1,1'-biphenyl (CBP) with MoO_3. It is interesting to note that the MoO_3 doping of CBP was performed using co-evaporation, while the p($g_4$2T-T) in our study was doped with Mo(tfd-$COCF_3$)$_3$ using a mixed solution, indicating that elongated clusters can form for both polymers and small organic molecules for different doping techniques.

Models for prediction of organic semiconductor transport properties most often assume that the dopant distribution is homogenous. This is in distinct contrast to our experimental observations of the doped films. The visualisation of the 3D film structure shows both a size distribution of the dopant clusters and also that the cluster morphology changed with dopant concentration. As a consequence, the distance between the clusters did not show a linear dependence on concentration, see Figs. 3c. The histograms of the distribution of distances to the nearest neighbour cluster in the samples show a wider distribution of distances for 5 mol% sample. The distributions are more narrow for the higher doping concentrations. The average distance to neighbouring clusters are 5.8 nm for 5 mol%, 3.9 nm for 20 mol% and 3.3 nm for 40 mol%. These numbers are significantly different from the dopant distances in a completely homogenous sample that are 2.75, 1.63 and 1.18 nm respectively. The experimental analysis of dopant position provide information that may be crucial for the modeling of these films.

It should be noted that although the dopant cluster sizes increase with increasing dopant concentration, the elongated morphology of the clusters did still allow each dopant to be adjacent to the surrounding organic semiconductor, see Figs. 2d-f. The transfer of charges is

therefore more efficient compared to the case of a more spherical cluster morphology[28]. These observations are consistent with results from films where the organic semiconductor PBDTTT-c was doped with with $Mo(tfd\text{-}COCF_3)_3$ [18]. The NMR study showed that dopant clusters that were several tens of nm in size did not contain unreacted dopants. An explanation for this could be that the dopants remained in contact with the surrounding organic semiconductor similar to the dopant clusters that are directly visualised with high spatial resolution sufficient to resolve the individual dopant molecules in our study.

Optical and Electronic Analysis

The main goal for the doping was to introduce charge carriers and enhance device-relevant electronic properties such as conductivity. The optoelectronic properties of the films were measured for undoped, 5 mol%, 10 mol%, 20 mol%, 30 mol% and 40 mol% samples in order to analyse the changes in properties. UV-Vis-NIR spectroscopy revealed the emergence of pronounced polaronic absorption bands at 900 nm and in the near infrared in the doped films. This confirmed that charge transfer had occurred, Fig. 5a. The polaronic absorption increased with increasing dopant concentration, indicating successful charge transfer with higher number of dopants[29,30]. This is in accordance with previous conclusions that the dopants are not blocked from charge transfer in their cluster formations. Results from electrical characterisation of the co-processed samples is shown in Fig. 5b. At a concentration of 5 mol% $Mo(tfd\text{-}COCF_3)_3$, there is a steep increase in conductivity as a function of higher dopant concentrations. However, at 20 mol% this increase starts to plateau and a decline is observed after 30 mol%. As discussed earlier, this conductivity trend as a function of dopant concentration has been observed in previous studies for other dopant-organic semiconductor combinations and has been attributed to a disruption in the nanostructure at high dopant concentrations[18,19]. Interestingly, the conductivity trend changes at approximately the same concentrations where changes in cluster shape and size were observed in the tomography reconstructions. However, the analysis of the nanostructure reveals that there are no large dopant aggregates present in any of the samples. Hence, each one of the dopant molecules should still be adjacent to the polymer and be able to undergo charge transfer.

It has been noted in a recent study that clustering of dopant molecules can have a direct impact on electronic properties for organic semiconductors[31]. Through modeling, the authors showed that an increase in the number of dopants in clusters from 1 to 6 molecules leads to a widening of the charge carrier density of states (DOS). A wider DOS indicates that the dopant clustering increases the energetic disorder in the system, and this in turn can have detrimental impact on device parameters such as conductivity. As the clusters observed in this study may be larger than 6 molecules and, more notably, there are large deviations in dopant sizes, we expect the energetic disorder to be even more severe in this system. Another recent study suggests that a drop in dopant ionisation efficiency at high doping concentrations may occur partially or completely due to a low entropy effect, and does not require large aggregated dopant phases[32]. At high dopant concentrations, the number of neighbouring dopant molecules will increase and the number of neighbouring hosts that favours dopant ionisation will decrease. This means that the dopants have a decreased probability of finding a host that favours charge transfer, leading to a loss in ionisation efficiency. Note that this effect does not require large aggregated dopant phases, but the formation of clusters will likely lead to further decrease of ionisation efficiency. In

light of the results from this study, these recent studies offer reasonable explanations to the decreased conductivity at high concentrations of Mo(tfd-$COCF_3$)$_3$ dopant in p($g_4$2T-T). This indicates that even small clusters of dopants may have detrimental impact on the electronic properties of the material and that the cluster morphology plays a crucial role.

Conclusion

The tomography method presented in this study yields data regarding dopant cluster distribution within organic semiconductor thin-films at sub-nanometre resolution. Utilising the Z-contrast from the dopant molecule Mo(tfd-$COCF_3$)$_3$ mixed with the semiconducting polymer p($g_4$2T-T), the 3D cluster nanostructure has been reconstructed, allowing the position of individual dopant molecules to be visualised. The usefulness of the technique is demonstrated by extracting quantitative information regarding cluster volume, aspect ratio and nearest-neighbour distance from the reconstructions. A heterogenous dopant distribution is observed, with significantly longer average distances to neighbouring clusters compared to that of a homogeneous distribution and also large variations from the average value. Determining the position of dopant molecules at sub-nanometre resolution has the potential to improve the accuracy of transport models for doped organic semiconductors, since these models generally lack information regarding their fine-scale distribution. The method presented here may also be utilised as a characterisation tool when designing dopant-organic semiconductor combinations in order to identify systems with minimal clustering.

The reconstructed nanostructures show a growing cluster size and increasingly elongated cluster shapes at higher doping concentrations. Further, electrical measurements correlates changes in dopant sizes and shapes with changes in conductivity at approximately the same concentrations. Despite this, the results show that the dopants remain sufficiently fine-dispersed to not be blocked from contact with the surrounding organic semiconductor, indicating that the decreased conductivity is not due to formation of large dopant phases or a disruption of the organic semiconductor nanostructure. Instead, we suggest that the increased sizes and deviation in sizes of the dopant clusters observed in this study introduce a higher energetic disorder and a lower number of neighbouring hosts that favours charge transfer, which in turn leads to the decreased conductivity observed in this study. These results indicate that even clustering at the single-nanometre scale can have a significant impact on the material's electronic properties, highlighting the need for characterisation techniques at this spatial resolution when developing future materials for organic electronic devices.

Conflicts of interest

There are no conflicts of interest to declare.

Acknowledgements

We would like to thank Chalmers Material Analysis Laboratory for their support of microscopes.
We gratefully acknowledge the financial support from the Swedish Research Council grants 2016-06146 and 2018-03824.

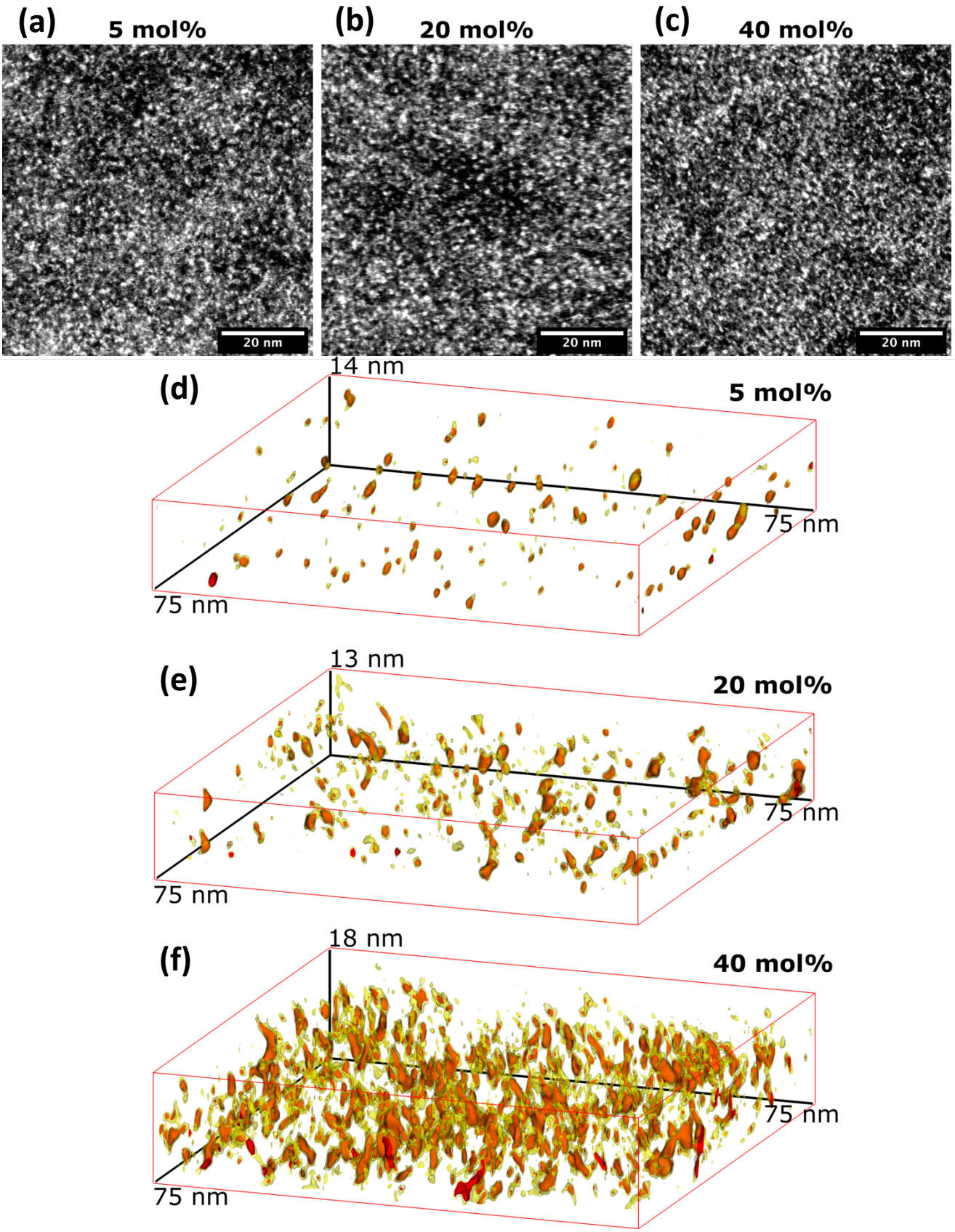

Figure 1: Electron microscopy HAADF-STEM images of representative areas (a-c) and tomography reconstructions (d-f) of p($g_4$2T-T) doped with Mo(tfd-$COCF_3$)$_3$. Red intensity thresholds in the reconstructions were chosen in order to visualise the position of dopant molecules. A lower intensity threshold is displayed in yellow.

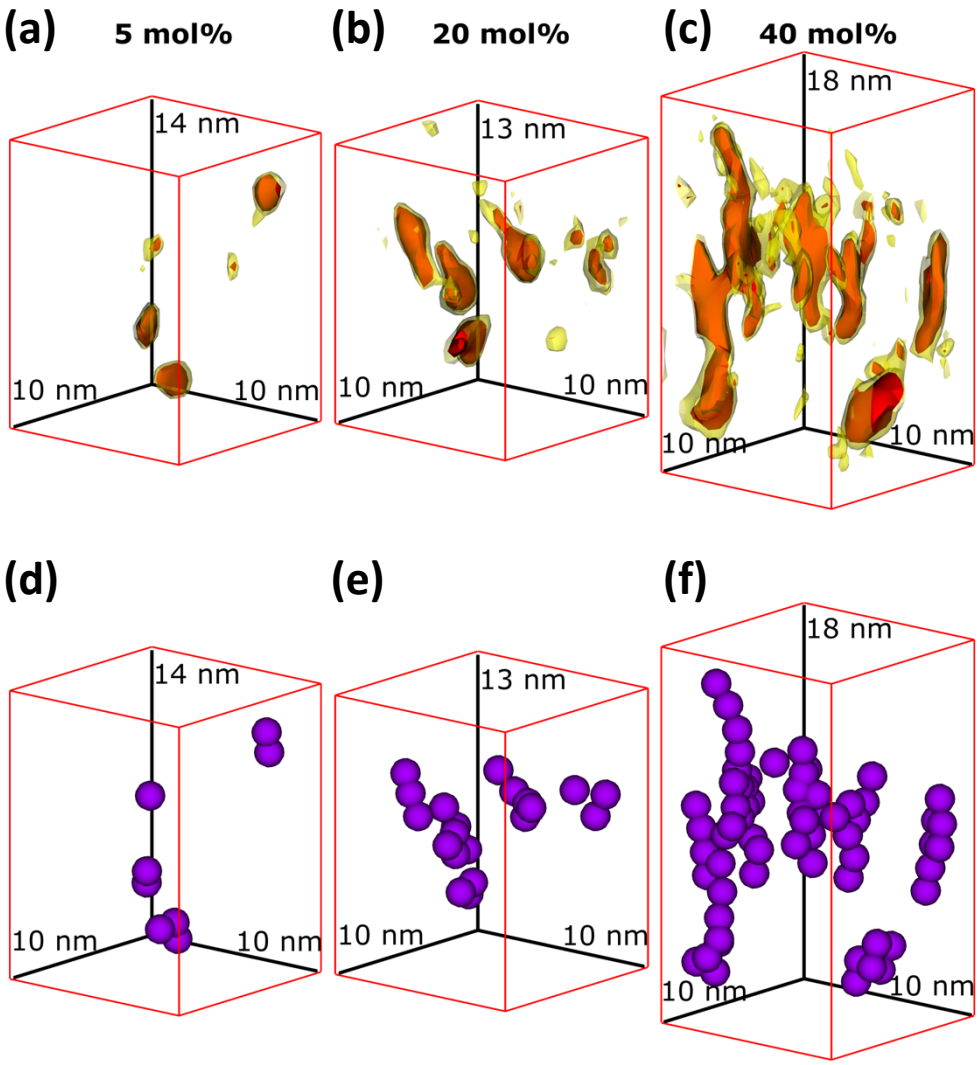

Figure 2: Example sub-volumes of the tomographic reconstructions from Figure 1 to more easily visualise (a-c) reconstructed cluster volumes and (d-f) data fitting of the positions of individual dopants in the clusters.

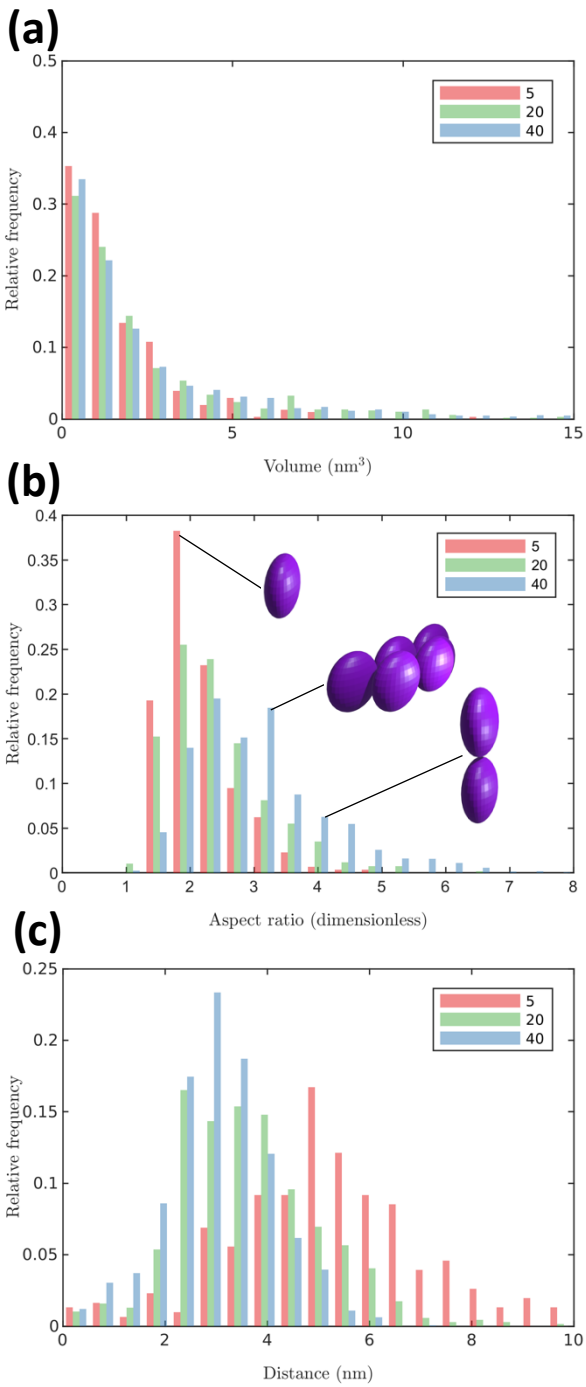

Figure 3: Histogram from data analysis on all clusters in a 150 nm by 150 nm in-plane area of each sample, displaying distribution of (a) cluster volumes, (b) cluster elongation ratios and (c) distances to nearest neighbouring clusters.

Table 1: Quantitative information from data analysis of tomography reconstruction regarding average cluster volume, elongation ratio and distrance to closest neighbouring cluster. The theoretical dopant-dopant distance of a homogenous distribution is provided as a comparison.

	5 mol%	20 mol%	40 mol%
Avg. volume per cluster [nm^3]	1.71	2.96	3.10
Avg. aspect ratio	2.14	2.40	3.01
Avg. distance to neighbour [nm]	5.17	3.63	3.03
Homogenous dopant distance [nm]	2.75	1.63	1.18

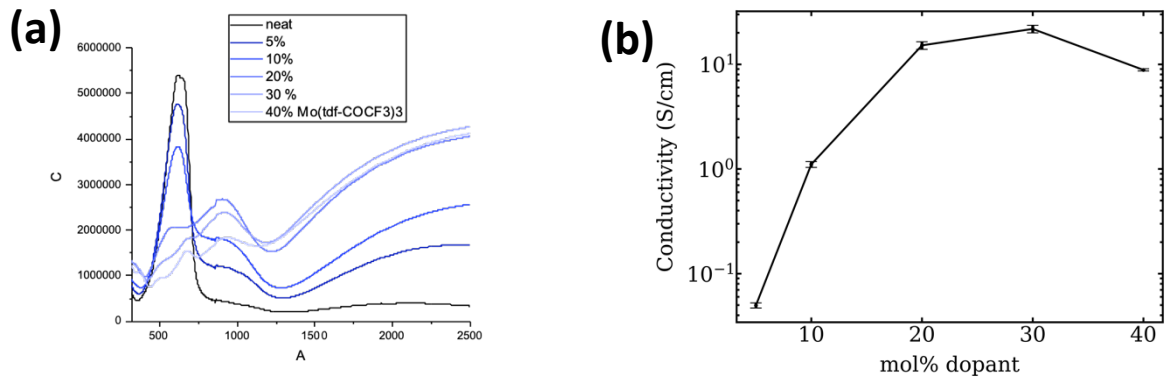

Figure 4: Results from electronic analysis of the doped samples through (a) UV-Vis-NIR absorption spectroscopy and (b) Four-point probe conductivity measurements.

Supporting Information

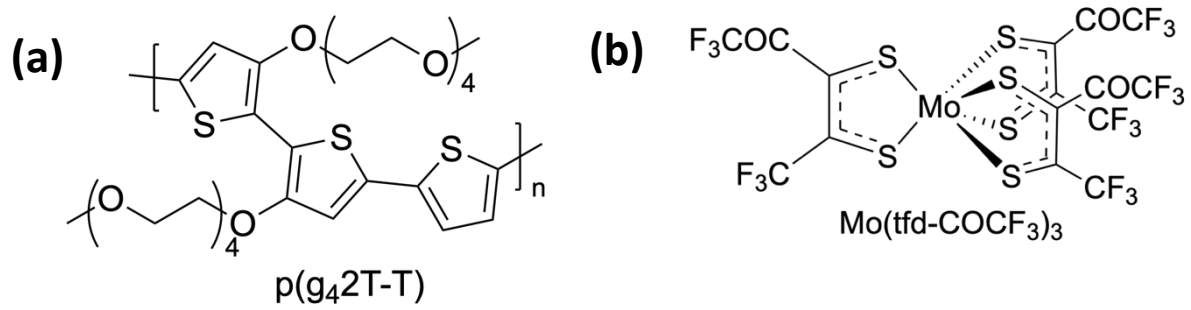

Figure S1: Molecular structures of (a) the semiconducting polymer p($g_4$2T-T) and (b) the molecular dopant Mo(tfd-$COCF_3$)$_3$.

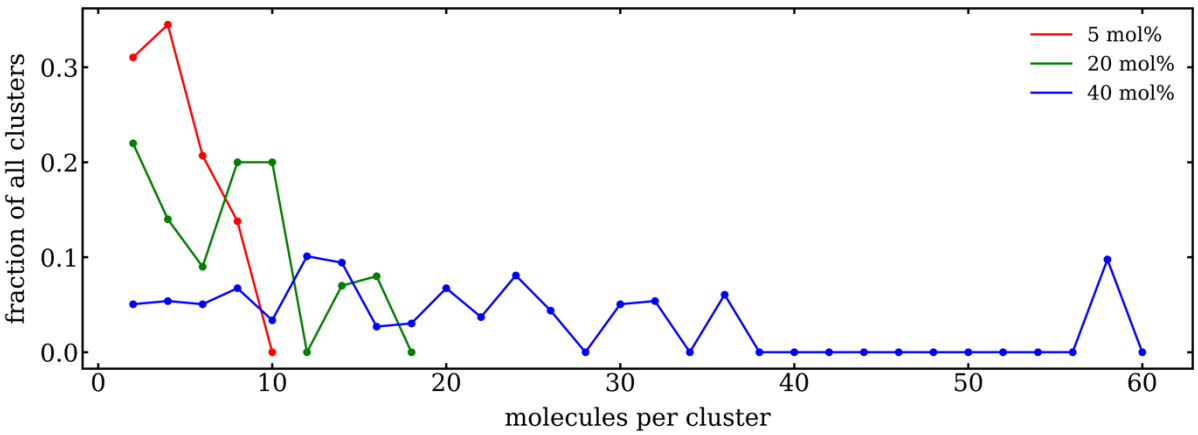

Figure S2: Distribution of number of dopants per cluster, determined from data fit of dopant positions for 50 reconstructed clusters in each sample. Average cluster sizes of 3.4 dopants, 4.6 dopants and 11 dopants are calculated for 5 mol%, 20 mol% and 40 mol%, respectively.

References

[1] R. M. Pankow and B. C. Thompson, *Polymer*, 2020, **207**, 122874
[2] W. Tress, *Organic Solar Cells Theory, Experiment, and Device Simulation*, Springer, Cham Switzerland, 2014
[3] A.F. Paterson, S. Singh, K. J. Fallon, T. Hodsden, Y. Han, B. C. Schroeder, H. Bronstein, M. Heeney, I. McCulloch and T. D. Anthopoulos, *Adv. Mater.*, 2018, **30**, 1801079
[4] D. Champier, *Energy Convers. Manag.,* 2017, **140**, 167-181
[5] B. Russ, A. Glaudell, J. J. Urban, M. L. Chabinyc and R. A. Segalman, *Nat. Rev. Mater.*, 2016, **1**, 1-14
[6] P. Cheng, G. Li, X. Zhan and Y. Yang, *Nat. Photon.*, 2018, **12**, 131-142
[7] C. Li , J. Zhou, J. Song, J. Xu, H. Zhang, X. Zhang, J. Guo, L. Zhu, D. Wei, G. Han, J. Min, Y. Zhang, Z. Xie, Y. Yi, H. Yan, F. Gao, F. Liu and Y. Sun, *Nat. Energy*, 2021, **6**, 605-613
[8] S. Yuvaraja, A. Nawaz, Q. Liu, D. Dubal, S. G. Surya, K. N. Salama and P. Sonar *Chem. Soc. Rev.*, 2020, **49,** 3423-3460
[9] B. Lüssem, M. Riede and K. Leo, *Phys. Status Solidi A*, 2013, **210**, 9-43
[10] I. Salzmann and G. Heimel, *J. Electron Spectros Relat. Phenomena*, 2015, **204**, 208-222
[11] I. E. Jacobs and A. J. Moulé, *Adv. Mater.*, 2017, **29**, 1703063
[12] S. N. Patel, A. M. Glaudell, K. A. Peterson, E. M. Thomas, K. A. O'Hara, E. Lim and M. L. Chabinyc, *Sci. adv.*, 2017, **3**, e1700434
[13] A. Hamidi-Sakr, L. Biniek, J.-L. Bantignies, D. Maurin, L. Herrmann, N. Leclerc, P. Lévêque, V. Vijayakumar, N. Zimmermann and M. Brinkman, *Adv. Funct. Mater.*, 2017, **27**, 1700173
[14] I. E. Jacobs, E. W. Aasen, J. L. Oliveira, T. N. Fonseca, J. D. Roehling, J. Li, G. Zhang, M. P. Augustine, M. Mascal and A. J. Moulé, *J. Mater. Chem. C*, 2016, **4**, 3454-3466
[15] K. Kang, S. Watanabe, K. Broch, A. Sepe, A. Brown, I. Nasrallah, M. Nikolka, Z. Fei, M. Heeney, D. Matsumoto, K. Marumoto, H. Tanaka, S. Kuroda and H. Sirringhaus, *Nat. Mater.,* 2016, **15,** 896–902
[16] J. E. Cochran, M. J. N. Junk, A. M. Glaudell, P. L. Miller, J. S. Cowart, M. F. Toney, C. J. Hawker, B. F. Chmelka and M. L. Chabinyc, *Macromolecules*, 2014, **47**, 6836-6846
[17] F. Deschler, D. Riedel, A. Deák, B. Ecker, E. von Hauff and E. Da Como, *Synth. Met*, 2015, **199**, 381-387
[18] J. Euvrard, A. Revaux, P.-A. Bayle, M. Bardet, D. Vuillaume and A. Kahn, *Org. Electron.*, 2018, **53**, 135-140
[19] C.-Y. Chang, B.-C. Tsai, Y.-C. Hsiao, M.-Z. Lin and H.-F. Meng, *Nano Energy*, 2019, **55**, 354-367
[20] A. L. Dixon, H. Vezin, T.-Q. Nguyen and G. N. M. Reddy, *Mater. Horiz.*, 2022, DOI: 10.1039/d1mh01574e
[21] H. Abdalla, G. Zuo and M. Kemerink, *Phys. Rev. B*, 2017, **96**, 241202
[22] S. Wilken, T. Upreti, A. Melianas, S. Dahlström, G. Persson, E. Olsson, R. Österbacka and M. Kemerink, *Sol. RRL*, 2020, **4**, 2000029
[23] Y. Yamashita, J. Tsurumi, M. Ohno, R. Fujimoto, S. Kumagai, T. Kurosawa, T. Okamoto, J. Takeya and S. Watanabe, *Nature*, 2019, **572,** 634–638
[24] R. Kroon, D. Kiefer, D. Stegerer, L. Yu, M. Sommer and C. Müller, *Adv. Mater.,* 2017, **29**, 1700930
[25] S. K. Mohapatra, Y. Zhang, B. Sandhu, M. S. Fonari, T. V. Timofeeva, S. R. Marder and S. Barlow, *Polyhedron*, 2016, **116**, 88-95

[26] J. M. LeBeau and S. Stemmer, *Ultramicroscopy*, 2008, **108**, 1653-1658
[27] D. Donhauser, M. Pfannmöller, L. Dieterle, K. Schultheiß, R. R. Schröder, W. Kowalsky and M. Kröger, *Adv. Funct. Mater.*, 2013, **23**, 2130-2136
[28] I. Salzmann, G. Heimel, M. Oehzelt, S. Winkler and N. Koch,*Acc. Chem. Res.,* 2016, **49**, 370–378
[29] J. L. Bredas and G. B. Street, *Acc. Chem. Res.*, 1985, **18**, 309-315
[30] H. Méndez, G. Heimel, S. Winkler, J. Frisch, A. Opitz, K. Sauer, B. Wegner, M. Oehzelt, C. Röthel, S. Duhm, D. Többens, N. Koch and I Salzmann, *Nat. Commun.*, 2015, **6,** 1-11
[31] C. J. Boyle, M. Upadhyaya, P. Wang, L. A. Renna, M. Lu-Díaz, S. Pyo Jeong, N. Hight-Huf, L. Korugic-Karasz, M. D. Barnes, Z. Aksamija and D. Venkataraman, *Nat. Commun.*, 2019, **10,** 1-10
[32] A. Fediai, A. Emering, F. Symalla and W. Wenzel, *Phys. Chem. Chem. Phys.*, 2020, **22**, 10256-10264